8-9-2021

Titanium Interconnection in Metallized Carbon Nanotube Conductors

Dylan J. McIntyre
djm9419@rit.edu

R I T

Titanium Interconnection in Metallized Carbon Nanotube Conductors

by

Dylan J. McIntyre

A dissertation submitted in partial fulfillment of the requirements
for the degree of Doctorate of Philosophy in Microsystems Engineering

Microsystems Engineering Program
Kate Gleason College of Engineering

Rochester Institute of Technology
Rochester, New York
09 August 2021

Titanium Interconnection in Metallized Carbon Nanotube Conductors

by
Dylan J. McIntyre

Committee Approval:

We, the undersigned committee members, certify that we have advised and/or supervised the candidate on the work described in this dissertation. We further certify that we have reviewed the dissertation manuscript and approve it in partial fulfillment of the requirements of the degree of Doctor of Philosophy in Microsystems Engineering.

_____

Dr. Brian J. Landi — Date
Professor, Department of Chemical Engineering

_____

Dr. Ivan Puchades — Date
Assistant Professor, Department of Electrical and Microelectronic Engineering

_____

Dr. Parsian K. Mohseni — Date
Assistant Professor, Department of Microsystems Engineering

_____

Dr. Karl D. Hirschman — Date
Professor, Department of Electrical and Microelectronic Engineering

_____

Dr. Cory D. Cress — Date
Materials Research Engineer, U.S. Naval Research Laboratory

_____

Dr. Michael S. Pierce — Date
Associate Professor, School of Physics and Astronomy

Certified by:

_____

Dr. Stefan F. Preble — Date
Director, Microsystems Engineering Program

ABSTRACT

Kate Gleason College of Engineering
Rochester Institute of Technology

Degree: Doctor of Philosophy **Program:** Microsystems Engineering
Author's Name: Dylan J. McIntyre
Advisor's Name: Dr. Brian J. Landi
Dissertation Title: Titanium Interconnection in Metallized Carbon Nanotube Conductors

Metallized carbon nanotube (CNT) networks aim to achieve conductivities competitive with bulk metals, while retaining the favorable temperature coefficient of resistance (TCR) for CNT materials. Cu is the predominant metal for high conductivity applications due to cost and availability. However, microscopy shows that Cu poorly wets a CNT surface and requires an adhesion metal for an improved physical and electrical interface. The present dissertation utilizes thermal evaporation as a direct method to evaluate 2-D coatings of Ti as an interfacial metal for bulk Cu-CNT hybrids. Specifically, a 10 nm Ti layer maintained a continuous and uniform coating after annealing to 400 °C for an hour, demonstrating the temperature stability of Ti on a bulk CNT network. Additionally, Ti successfully suppressed the delamination of a Cu overcoat and achieved a 12% decrease in resistance for Cu-Ti-CNT hybrids after annealing at 400 °C.

The benefits observed with thermally evaporated Ti adhesion layers motivated the development of a 3-D deposition approach using a novel joule-heated driven CVD technique, which can deposit metal throughout the entire bulk volume. Specifically, an oxygen-free precursor, cyclopentadienyl(cycloheptatrienyl) titanium(II), was used in the process under an inert/reducing atmosphere (95% Ar/ 5% H_2) to promote a pure Ti metal deposition. Cross-sectional EDX mapping revealed that CVD successfully achieved diffusion of Ti throughout the entirety of a ~30 µm-thick, porous CNT conductor, demonstrating the capability of CVD as a method to fabricate bulk integrated Ti-CNT conductors for the first time. CVD coating morphology is shown to be tunable via the amount of precursor used, reactor pressure, and temperature, ranging from coatings localized along the individual bundles within the network to a fully connected film formation. Additionally, modification of reactor environment provides control over metal oxidation during growth onto the CNTs, achieving oxide-free to mixed Ti-oxide depositions as validated via Raman spectroscopy. The effectiveness of pure Ti as an adhesion metal on CNTs is benefitted from its wettability, temperature stability, and low contact resistance to CNTs; which can motivate investigating other potential adhesion metals that typically produce stable oxides like tungsten.

Modeling of the temperature dependent electrical characteristics indicates an increase in metallic conduction behavior for the Ti-CNT conductors, with a decrease in the tunneling barrier between CNTs after Ti deposition, demonstrating the benefits of nanometal interconnection and showcasing the utility of temperature dependent modeling as a tool to assess nanoscale interaction of metallized CNT networks. CVD deposited Ti-CNT conductors electroplated with Cu, annealed, densified and then annealed a second time, realize conductivities as high as 43.1 MS/m, which is the highest conductivity reported for a bulk metal-CNT conductor at 98% weight loading. A Ti seeded CNT conductor (~9% w/w) electroplated to 98% total metal mass was demonstrated to achieve

a specific conductivity of 6257 Sm^2/kg, with a TCR (from 300-600 K) of 3.49×10^{-3} K^{-1}, which combined result in a surpassing of the specific conductivity of pure Cu at temperatures above 250 °C. Thus, the overall impact of this work is demonstration of advanced conductors with a combined high conductivity and low TCR, which can provide direct energy savings at elevated temperature operation for applications such as high efficiency motors.

ACKNOWLEDGEMENTS

I would like to thank my advisor, Dr. Brian Landi, for the invaluable guidance and support that he provided throughout my Ph.D. His advice has undoubtedly helped shape my abilities as a researcher and communicator. Moreover, he has shared countless bits of wisdom that extend to all areas of life. He has served as a role model of a leader and provided a work environment that encouraged me to work hard through inspiration. I am very grateful for having had the opportunity to pursue a Ph.D under his advisement.

I would like to thank my committee members: Dr. Ivan Puchades, Dr. Parsian Mohseni, Dr. Karl Hirschman, and Dr. Cory Cress. Their guidance has helped me improve both my fundamental understanding of the research as well my analysis and approach, and ultimately contributed to my growth as a researcher. I'd also like to thank Dr. Michael Pierce and the Microsystems Engineering Department head, Dr. Stefan Preble.

I would like to thank all of my co-workers, fellow students, and staff at RIT: Alireza Abrand, Mohad Baboli, Sam Boyd, Dan Broderick, Andrew Bucossi, Kyle Crompton, Martin Dann, Tristin Del Vecchio, Shannon Driess, Julia D'Rozario, Anastasiia Fedorenko, Soumya Gupta, Stephanie Hart, Q Hernandez, Ryan Hirschman, Ross Hisert, Emily Kessler-Lewis, Elaine Lewis, Erin Loughran, Tomasz Mazur, Sarah Nadzam, George Nelson, Josh Owens, Amber Palka, Steve Polly, Jamie Rossi, Zackary Santos, Meleni Sarantos, Jim Smith, Karen Soule, Jason Staub, Alex Tomkiewicz, Heather Ursino, Thomas Wilhelm, Lisa Zimmerman, and any others that I haven't listed here. You have all made the experience here more enjoyable.

I would also like to thank Dr. Carolina Ilie, Dr. Mohammad Islam, and Dr. Alok Kumar for their indispensable advice and guidance with regards to research, professional development, and life in general throughout my undergraduate studies at SUNY Oswego.

Lastly, I would like to thank all of my family for their endless support and encouragement, and inspiring me the entire way here. You have all played a big role in my life, and I have so much gratitude for each and every one of you.

ACRONYMS

CHT-Ti-Cp, cyclopentadienyl(cylcoheptatrienyl)titanium(ii)

CNT, carbon nanotube

CFH, continuous filament heating

CVD, chemical vapor deposition

EDS/EDX, energy dispersive X-ray spectroscopy

M/L, mass per length

R/L, resistance per length

SEM, scanning electron microscopy

tCp_2-Ti-Me_2, Dimethylbis(t-butylcyclopentadienyl) Titanium (IV)

TCR, temperature coefficient of resistance

TTIP, Titanium Tetrapropoxide

$W(Cp)_2H_2$, bis(cyclopentadienyl)tungsten(iv)dihydride

Contents

1 Introduction

1.1 Individual Carbon Nanotubes

An individual CNT is comprised of a hexagonal arrangement of sp^2 bonded C atoms formed in a cylindrical geometry (as depicted in Figure 1a). The configuration of the terminating atoms is formed based on the chiral angle connecting two crystallographically equivalent points of the hexagonal lattice, which consequently influences the electronic character of the nanotube. The chiral angle can range from 0° to 30°, where 0° forms a zigzag geometry at the terminating edge, while a chiral angle of 30° represents an armchair configuration. The resultant electronic properties of the CNT can be approximated via the zone-folding approximation, which applies a periodic boundary condition to the band structure of graphene to simulate the circular structure of a CNT. In graphene, a Dirac cone is formed in the electronic band structure at the 6 corner points of the 1st Brillouin zone, whereby there is a zero band gap at the center of the cone [1]. Therefore, if the periodic slices intersect the center of the Dirac cones, metallic behavior is observed, which occurs in the case of armchair terminated CNTs. Specific zigzag configurations also result in the metallic behavior due to slices crossing through the center of the corner points of the 1st Brillouin zone. However, chiral angles that result in slices passing through the tapering portion of the Dirac cone will be semiconducting with a band gap related to the location of the slice. Additionally, the number of concentric walls forming the CNT (see Figure 1b) influences the electronic transport. Metallic behavior has been shown computationally for double walled CNTs, even if the concentric walls are comprised of semiconducting nanotubes. The number of concentric walls present tends to be influenced by the methods employed to synthesize the CNTs. Laser vaporization and chemical vapor deposition (CVD) based synthesis

techniques, for example, have been shown to produce either single walled CNTs (SWCNTs), double-walled (DWCNTs), or multi-walled CNTs (MWCNTs), based on the technique used and experimental conditions.

For laser synthesis, a target consisting of graphite mixed with powdered metal catalyst is inserted into a heated tube furnace with inert gas flow, and bombarded by a pulsed laser, which induces local heating to sufficient temperatures for vaporization of the carbon and metal catalysts [2]. The vapor-phase carbon and metals then form nuclei, whereby the carbon diffuses through the metal and creates a site for CNT growth. Additional carbon then joins the graphitic cylinder to continue CNT growth, which is more energetically favorable than nucleating a concentric shell, thereby promoting exclusively SWCNT production.

CVD based synthesis techniques are capable of achieving kilogram amounts of synthesis product and can be adapted in a variety of ways [3]. One particular CVD based approach is floating-catalyst CVD (FCCVD), which is especially relevant for the materials discussed throughout this dissertation. FCCVD utilizes a carbon feedstock and gaseous metal catalyst precursor that are injected into a heated furnace, which provides the temperature necessary to decompose the injected compounds into catalyst particles for CNT growth. The loose aerogel of CNTs that forms in the reactor can be extracted through a condensation and winding process, resulting in a fibrous roving material comprising a bulk CNT network [4, 5].

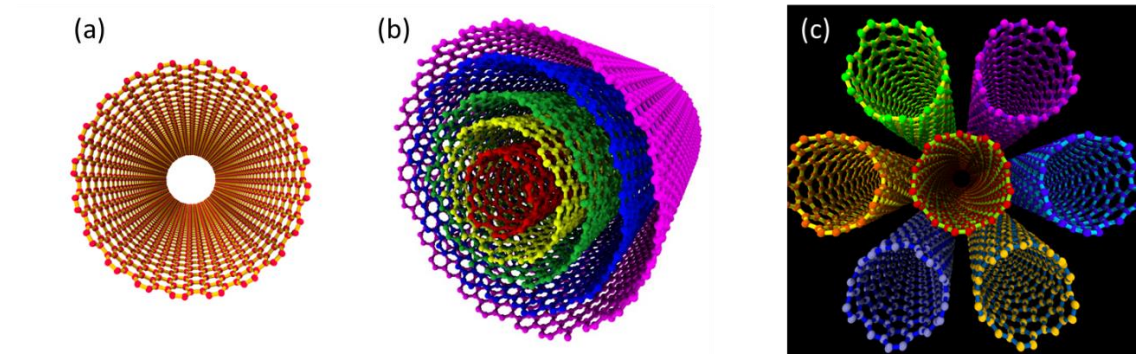

Figure 1 Rendering of a (a) SWCNT, (b) MWCNT, (c) bundle of SWCNTs. Graphics courtesy of Andrew Merrill as part of Dr. Landi's research group.

1.2 Bulk Carbon Nanotube Conductors

Bulk carbon nanotube (CNT) conductors have been extensively studied in recent decades due to their excellent flexibility, corrosion resistance, mechanical, and electrical properties [6, 7]. A driving force for the development of bulk CNT conductors towards electrical applications is the promise of exceeding the conductivity of metals, which is theoretically possible for an individual CNT. Ballistic conduction has been reported both theoretically and experimentally [8–11], which would correspond to conductivities > 10^8 S/m for a 1 nm diameter and 1 μm length. However, these transport properties heavily depend on individual CNT characteristics such as chirality and number of walls, which govern the density of states and electronic band structure [12]. Consequently, a number of issues arise when translating the properties of individual CNTs to the bulk scale. For example, individual CNTs, when in close proximity, tend to agglomerate into bundles of various sizes due to the strong interaction between the delocalized orbitals [13, 14]. The bundling that occurs between the CNTs can, in turn, alter the electronic structure of the CNTs. For example, bundling can induce a bandgap in Armchair CNTs, which otherwise would have a zero-bandgap [15]. In general, bundling has been suggested to induce

scattering between the CNTs [16]. Moreover, the formation of a network leads to additional parameters which impact transport. The overall electrical conduction in CNT networks can be thought of as a sum of the individual electrical contributions stemming from transport along individual CNTs (intra-CNT transport), as well as the conduction between CNTs (inter-CNT transport).

The intra-CNT transport is greatly influenced by the presence of surface defects or impurities located along the nanotube, which can arise as byproducts of synthesis. Individual CNTs have been experimentally measured to have resistance per lengths on the order of the 6 kΩ/μm [17], which is the theoretical quantum resistance limit for SWCNTs [18]. However, this resistance is not reliably achieved due to the random distribution of defects present after synthesis [19]. In fact, the difficulty in producing homogenous defect-free CNTs leads to a large inconsistency in reported mean-free-path (MFP) and R/L values [18, 20, 21]. Defects and impurities can act as scattering sites, which greatly impact the MFP of electrons in 1D conductors.

Inter-CNT transport is otherwise affected primarily by the electrical barrier at the contact point between intersecting CNTs, e.g. the junction sites. Junction resistance has been reported to be a major contributing factor to the overall resistance in pristine CNT networks via C-AFM studies, where current maps of the network reveal the transport characteristics [22–25]. The junction resistance between two CNTs varies depending on the electronic type of each nanotube. The contact resistance between similar electronic type CNTs has been found to be far less than between electronically type mismatched CNTs, with metallic-metallic junctions having the lowest contact resistance [22, 24].

Contact resistance can arise due to thin tunneling barriers present at the contacts, or by the presence of Schottky barriers.

Models of the CNT network conduction have been developed, which describe multiple competing effects in the conduction of electrons [16, 26]. Namely, charge carrier conduction has partial contributions from metallic transport (limited by phonon backscattering), tunneling through thin barriers, and variable range hopping between spatially localized electronic states, which arise in highly disordered systems. The term "variable range" stems from the fact that the electronic transition is not limited to immediate neighbor states, but rather to other energetically favorable states depending on the length of localization (i.e. extent of the wavefunction). An implication of this phenomenon is that, as the temperature of the material increases, electrons in trapped states may adsorb enough phonon energy to transition states and participate in conduction, increasing the conductivity of the network. In fact, traditional metals decrease in conductivity when temperature is increased, due to increased phonon activity, which acts as a scattering mechanism for already free electrons. Bulk CNT networks, on the other hand, have been shown to have an order of magnitude lower variation in resistance with increasing temperature than traditional metals [27], making CNTs an attractive material for high-temperature applications. The conduction behavior in bulk CNT networks, therefore, differs greatly from traditional metals. As such, while traditional metals have the advantage of high conductivity at the bulk scale, bulk CNT networks exhibit favorable temperature dependent electrical properties. However, bulk CNT networks still require advancement to realize their inherent conductive capabilities for electrical applications.

Over the past decade, there has been a lot of attention focused on improving the electrical conductivity of bulk CNT conductors. Post-processing techniques, for example, have been explored to enhance the conductivity of bulk CNT networks via improving alignment, bridging junctions, and/or modifying local electronic structure through stretching [28], chemical doping [29–32], radial, solvent, or planar densifications [7, 33, 34], and thermal treatment [35]. Additionally, a hybridized metal-CNT network has been of high interest in recent years as a means to achieve conductivities close to that of metallic wires by bridging the resistive CNT junctions with highly conductive metals [27, 36, 37], while maintaining the favorable temperature coefficient of resistance (TCR) for the CNT bulk materials [27, 37]. Utilizing metals for adhesion as opposed to non-metallic adhesion materials is benefitted by the delivery techniques that can be adapted, such as Joule-heating driven CVD, which can encourage site-selectivity of deposition to the regions of the network that are benefitted the most [27], as will be discussed in more detail later.

1.3 Metal-CNT Conductors

Hybridizing CNTs with metals is an attractive method toward improving network conductivity, as the metals may serve to lower the electrical barrier between CNTs, as well as fill out the void space with a conductive material. From the other perspective, individual CNTs residing in a metal matrix can be thought of as ballistic transport centers within the metal, improving the local transport throughout metal matrices, as described by Tokutomi et al. [38]. Charge carriers in a metal wire will scatter according to the length of the MFP (see Figure 2). The presence of CNTs can act as local ballistic

pathways with an extended MFP, increasing the collective MFP, and thus providing an enhancement in the conductivity of the metal.

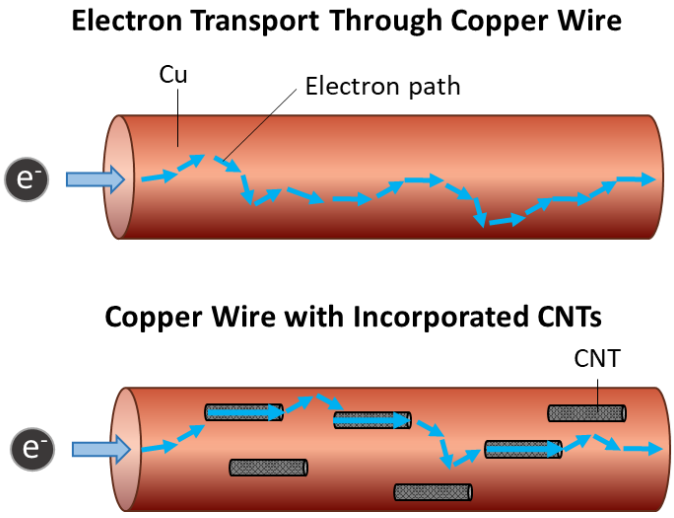

Figure 2 Schematic of the electrical path for charge carriers in Cu with and without CNTs present.

Simulations have predicted that embedding purely ballistic CNTs with perfect alignment into a Cu matrix can double the room temperature conductivity of Cu using only 30-40% CNT filling, assuming ideal electrical contact [39]. Cu is known to interface poorly with CNTs, so another simulation was conducted for a Ti interfaced CNT matrix, and suggested that Cu-Ti-CNT conductors can achieve double the conductivity of Cu for CNT fillings in the range of 30-60%. However, significant challenges must be overcome to realize (or at least approach) such ideal conditions. The primary areas requiring advancement include the synthesis of metallic defect free CNTs in bulk, and improved delivery of metals throughout the CNT network to achieve enhanced electrical contact (especially those metals which interface well with CNTs). The work herein will focus on the latter. Currently there exists multiple routes of interfacing metals with CNTs, each

with their own advantages and disadvantages. The three primary routes that will be explored here are PVD, CVD, and Electroplating.

1.3.1 Physical Vapor Deposition

The use of physical vapor deposition (PVD) can be employed for metalizing CNT networks through methods such as thermal or e-beam evaporation [40–43] and magnetron sputtering [44–48]. Thermal evaporation relies on ejecting atoms from a source material via thermal stimulus and allowing them to condense onto a substrate. The technique is carried out under vacuum, and thus the long mean-free-path for the vapor particles enables uniform deposition along a topologically flat/smooth surface. However, due to the line-of-sight nature of the technique, surface irregularities can cause shadowing to occur, which results in non-uniform deposition. For a porous network (such as that obtained by CNTs), these techniques offer limited penetrability, and provide primarily surface coatings, as the top layer of CNT bundles will effectively mask or shadow the underlying portions of the network. These techniques benefit from providing very pure depositions, and are ideal for constructing layered conductors, or for probing the interfacial interaction between the metals and the CNTs. These advantages make PVD an ideal route for evaluating the surface interaction between metals and CNTs.

It has been hypothesized that the high energy of bombardment upon the CNT substrate induced by incident sputtered metal atoms may lead to defects [49, 50], which are claimed to localize electrons [49]. Electron localization results in an increase in the network resistivity and is attributed to an increased sp^2-sp^3 rehybridization [51]. Janas, et.al, found that, for Pt, Pd, Ag, and Au, sputtering indeed results in an increase in resistance of the metal-CNT hybrid during the initial deposition stages [49]. Sputtering

Au onto a 10 µm thick CNT network had the greatest impact electrically (among the metals studied), with a maximum increase in resistance of 200% compared to the starting CNT network. In fact, for thinner CNT substrates (~100 nm), the impact on increased resistance exacerbated, exhibiting a maximum increase in resistance of 1600% for the Au-CNT network, further emphasizing the surface locality of the effect. However, after a certain threshold of deposition time, percolation pathways formed which lead to a reduction in electrical resistivity. With enough deposition time, the resistivity of the networks eventually decreased beyond their starting resistance for all metals deposited. Thus, PVD techniques can be used to fabricate metal-CNT conductors with improved electrical properties, but may also impact the structure of the underlying CNTs.

1.3.2 Chemical Vapor Deposition

CVD is a popular technique for depositing metals onto topologically non-uniform substrates due to its reactive nature, which allows for better conformality across irregular and high-aspect ratio features [52]. Methods such as ALD are capable of achieving highly controlled conformal coatings on CNT networks, however, can require several hundred cycles (~1 min/cycle) to obtain thicknesses of ~15-30 nm for various metals [53, 54]. CVD otherwise offers a fast, scalable approach toward metal deposition, while still enabling infiltration throughout CNT networks. Typically, a powder or liquid precursor is brought into a vapor phase through applied heat. To reduce the precursor to a pure metal, excess energy in the form of heat must be supplied to crack the ligand and decompose the precursor. This excess heat can be applied after the vapor-phase precursor condenses onto a cool substrate; otherwise the reduction can occur upon contact with an already hot substrate (whereby the temperature exceeds the decomposition temperature).

There are multiple ways to provide heat to a substrate for decomposing the vapor-phase precursor. An intriguing method in the context of CNT networks is Joule-heating (or resistive heating). In this case, the resistive components of the network generate the required energy for decomposing the precursors. At low currents, this lends the heating to be site-specific in nature, spatially localizing the heat adjacent to the resistive regions in the network. Alternatively, at sufficiently high currents, the lowest temperature anywhere along the length of the conductor is above the decomposition temperature of the precursor, in which case the deposition will tend toward a uniform distribution. Joule-heating driven CVD is a novel delivery technique that has been established relatively recently as an effective route for depositing metals into CNT networks for device applications, whereby the metals preferentially deposit at the junctions sites between contacting CNTs [55]. More recently, Leggiero, et al, have expanded this technique to produce the first ever Joule-heating driven CVD-based bulk metal-CNT hybrid, whereby site-specific depositions of $Cu(tBaoac)_2$ were demonstrated, and full integration throughout the thickness of the conductor was achieved [27]. This technique, when combined with electroplating to interconnect the Cu seeds, led to a record conductivity of 28.1 MS/m for a conductor consisting of a mass percentage of 94.2% Cu w/w. Recent advances in this technique render it a promising method toward high-conductivity bulk CNT conductors.

1.3.3 Electrodeposition

A viable and well-studied route for delivering metals onto CNTs is electroplating [27, 37, 50, 56–60]. Electroplating relies on the transfer of metal ions from a counter electrode to a CNT working electrode through an electrolytic solution. Ions in solution

are adsorbed at the CNT surface via electrostatic attraction, and subsequently reduced by the charged CNT interface or impurities [57]. As a result, electroplating can achieve internal depositions within the CNT network via diffusion of ions in solution through the network. The degree of internal plating depends on the rate of ion diffusion through the CNT network relative to the deposition rate. Thus, surface plating can be encouraged by increasing the current to the extent that deposition occurs more rapidly than ionic diffusion through the CNT network [37]. As such, electroplating offers the tunability of internal vs. surface depositions.

Hannula, et al, found that surface functionalization plays an important role in the deposition properties for Cu electroplated CNTs [57]. It was found that Cu deposits in an inhomogeneous manner on a pristine film comprised of >80% MWCNTs because of the lack of active nucleation sites. On the other hand, oxygen functionalized films, produced by thermal treatment in air or anodization, provided a highly active surface resulting in uniform coatings. Surface activation via functionalization, however, increases the defect content in the CNT film, evidenced by an increased D/G ratio. Increasing the functionalization improves the hydrophilicity of the CNT film and provides more active sites, however, excessive functionalization can severely impact the electrical properties of the film. In such a scenario, there exists a trade-off between increased resistance and improved wettability.

An alternative way to increase the amount of active sites is to perform a two-step process, whereby the CNT conductor is first “seeded”, and then electroplated [27, 37, 50]. Such a method has been employed recently by Tran, et al, in which a wet-spun CNT wire purchased through DexMat was sputtered with an Au adhesion layer, prior to Cu

electrodeposition [50]. Notably, electroplating the as-received CNT wire resulted in a non-continuous Cu coating, with few nucleation sites leading to island growth in the initial deposition stages. The Au sputtered CNT wire, however, had greatly improved surface coverage during the initial deposition stages, with smaller and more abundant nuclei. A previous study has shown that the presence of Au improves the hydrophilicity of CNTs, which is important for the wetting of the aqueous electrolyte [49]. Additionally, the Au provides uniform activation sites for nucleation during electroplating. Furthermore, the Cu-Au-CNT wire achieved conductivities up to 80% of pure copper's conductivity and density savings up to 42%. Thus, metal seeding can offer an advantage over oxygen functionalization for improving the electroplating deposition dynamics.

1.4 Metrics and Techniques

To quantify the performance of metals deposited onto CNTs via the aforementioned methods, a variety of metrics are employed. Characterization of the defect and elemental purity, conductivity, temperature dependent electrical properties, and morphology, among other characteristics, provide crucial information toward understanding the metal-CNT characteristics. Evaluating these properties is necessary to quantify the advantages of the different deposition techniques and the improvements they offer to the starting materials.

1.4.1 Conductivity, Specific Conductivity, and Temperature Dependent Resistivity

Volumetric and Specific Conductivity

Volumetric conductivity (or simply, conductivity) is a paramount metric for assessing the performance of bulk CNT networks, and for drawing comparisons to traditional metallic conductors. Bulk conductivity of a material is defined by three

parameters: the cross-sectional area of the conductor, *A*; and the resistance, *R*, over a unit length, *L*. The equation governing conductivity is expressed as:

$$\sigma = \frac{L}{R \cdot A} \tag{1}$$

Linear four-point probe measurements offer a reliable, facile method toward the measurement of a material's R/L, while circumventing the contact resistance of the measurement probes. In this configuration, two outer probes supply current through the conductor, while two inner probes separated by a distance, L, act as a voltage meter. The R/L measurement can then be correlated with cross-sectional area to calculate conductivity. The cross-sectional area can be either calculated based on optical microscopy diameter measurements (for uniform cylindrical conductors) or obtained by SEM (for irregular conductors).

A challenge that can arise when characterizing bulk CNT networks is the non-uniformity in cross-sectional area that may be present along the length of the conductor. In such cases, mass specific conductivity is a preferred metric, which evaluates the electrical performance with respect to mass instead of cross-sectional area. Such a metric can also be useful to determine weight-savings provided by the advanced conductors. The mass specific conductivity is defined as follows:

$$\sigma_{sp} = \frac{\sigma}{D} = \frac{L/RA}{M/LA} = \frac{L^2}{RM} \tag{2}$$

where *D* is the density of the conductor, and *M* is the mass of the conductor. Measurement of the mass can be reliably made using a microbalance to provide the necessary data for calculation of the specific conductivity.

Temperature Dependent Resistivity

Temperature dependent electrical behavior lends insight toward the interaction between metals and CNTs. A vital component to hybridizing the CNTs with metals for conductive applications relies on improving the conductivity of the CNTs while preserving the beneficial temperature coefficient of resistance (TCR) properties inherent to CNT materials. Several physical phenomena are responsible for the change in resistance that materials experience under differing temperature conditions. In the case of metals, phonons increase the amount of collisions that free electrons endure in their conduction path, decreasing the MFP and increasing resistance at elevated temperatures. However, for semiconductors, the extra energy can assist in breaking captive electrons free from their host, allowing them to contribute to conduction at elevated temperatures. In general, the temperature coefficient of resistance for metals, α_0, is expressed as

$$\alpha_0 = \frac{\rho - \rho_0}{\rho_0 (T - T_0)} \tag{3}$$

where ρ_0 is the initial resistivity corresponding to an initial temperature, T_0, and ρ is the final resistivity corresponding to an elevated or reduced temperature, T.

An additional factor governing the temperature dependent electrical properties of metals is the metal grain structure. In fact, the measured TCR for electrochemically deposited Cu interconnects has been demonstrated to vary with grain structure [61]. The resistivity, ρ_0, of a metal consists of two components: the temperature-dependent component, which is influenced by phonon scattering, $\rho_T(T)$; and the scattering at defects, surfaces, and grain boundaries, ρ_R, which is temperature-independent. Thus, the

resistivity can be expressed as $\rho = \rho_T(T) + \rho_R$ [61]. Therefore, to understand the role that grain boundaries impart in the electrical behavior, the TCR can be rewritten as:

$$\alpha_0 = \frac{\rho_T(T) - \rho_T(T_0)}{(\rho_T(T_0) + \rho_R)(T - T_0)} \quad (4)$$

Consequently, it is evident that α_0 will decrease with an increased ρ_R, which can arise from a reduced grain size (or increased impurity concentration/crystal defects). While grain expansion can be induced in thin copper films via annealing, the maximum size is ultimately restricted based on film dimensions. A consequence of this is that, while the thickness of a surface Cu film may be tuned by deposition parameters, depositions internal to porous structures will ultimately be constricted in dimensions in accordance to the pore confinements.

CNTs exhibit a more complex conduction behavior. Previous efforts have been made to model the temperature dependent conduction behavior of CNT networks by considering the different contributing factors to network conduction [16, 26], expressed as:

$$\sigma(T) = \left[A\exp\left(-\frac{T_m}{T}\right) + B\exp\left(\frac{T_b}{T_s + T}\right)\right]^{-1} + H\exp\left(-\left(\frac{T_0}{T}\right)^{\gamma}\right) \quad (5)$$

where A and B are coefficients related to morphology of the network (alignment, density, etc.). The three terms correspond to the contributions from metallic conduction, fluctuation assisted tunneling through thin barriers, and variable range hopping, respectively. Energies of the respective components can be obtained by multiplying the parameters by Boltzmann's constant, k_b. The energy k_bT_m is the metallic component that

corresponds to the backscattering energy of zone-boundary phonons for quasi 1-D conductors. Charge carriers that exhibit metallic character in this way have improved conduction at lower temperatures due to the lesser phonon activity. k_bT_b represents the typical tunneling barrier energy which occurs between contact regions (CNT junctions), and T_s/T_b relates to magnitude of the quantum resistivity in the low-temperature limit. T_0 is a function of the electronic wave function localization length, which governs the carrier's ability to tunnel between localized states with assistance from phonon absorption (VRH). As such, the relative sensitivity of this term to change in temperature strongly depends on the localization length. Additionally, the dominance of this term is influenced by the degree of localized states within the network. For thicker networks, a greater number of metallic percolation pathways become available, and the VRH term becomes negligible. For thinner networks, however, localized states represent a greater proportion of the network, and the VRH term becomes an important consideration. The location of localization is represented by $\gamma = \frac{1}{1+d}$, where d is the dimensionality. In this case, a dimensionality of 1 suggests intra-CNT localization, whereas d = 2 or 3 suggests inter-CNT localization. These models have had success in fitting to measured data for CNT networks and lends insight toward the character of different networks.

Temperature dependent conductivity measurements can be made at RIT are using a commercial JANIS cryostat (see Figure 3) which handles temperatures ranging between 77 K – 800 K under vacuum (low 10^{-6} mbar). The temperature controller and four-point probe equipment are interfaced with LabVIEW for precise temperature control and electrical measurements. Measurements are typically made by recording IV sweeps at 5 degree increments at temperatures ranging from 300 – 600 K.

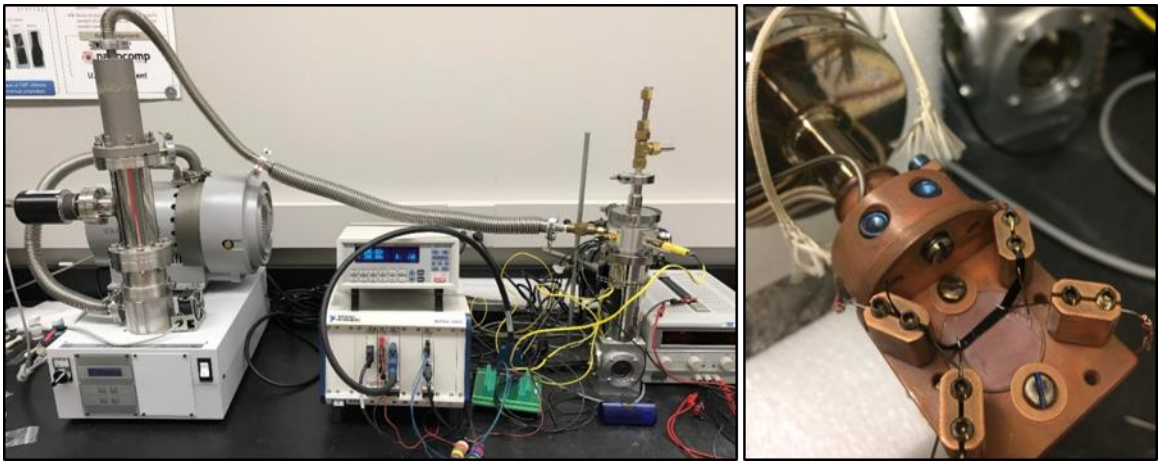

Figure 3 Left image: Vacuum pump (left), temperature controller (center), and JANIS cryostat (right). Right image: JANIS cryostat four-point probe stage.

To gain insight toward the interaction between CNTs and deposited metals, a parallel resistor model was developed [27] which treats the systems as two independent layers (no interaction between CNTs and Cu), and can be expressed as

$$\frac{1}{R(T)_{tot}} = \frac{1}{R(T)_{Cu}} + \frac{1}{R(T)_{CNT}} \tag{6}$$

where R(T) is the resistance as a function of temperature. In this case, resistance is obtained via each materials' measured specific conductivity, and R(T) is subsequently calculated by using each materials' corresponding TCR values. A sample which adheres to the model reflects a non-interacting bilayer system. Deviation from this model otherwise suggests that interaction between the materials exists. Thus, various models can be applied to understand the conduction behavior of the metal-CNT networks as well as whether interaction exists between the hybrid components.

1.4.2 Morphology Analysis (SEM)

Scanning electron microscopy (SEM) is a powerful tool for qualitatively identifying the presence of particles (such as catalysts) in the network, as well as

assessing the microscopic morphology of the network and particles within it. Additionally, SEM can be used to directly measure the cross-sectional area of the CNT conductors. Due to the irregular nature of bulk CNT networks, cross-sectional measurements may require specialized techniques to prepare the samples for SEM imaging. Several methods exist to achieve cross-section preparation, each with their own advantages and disadvantages. RIT has the capability to perform cross-sectioning via epoxy-setting followed by microtoming, laser-cutting using a Forest Scientific 30 W VLS2.30 CO_2 laser, or razor slicing. The first option, microtoming, offers minimal distortion to the cross-sectional area size, but is time and labor intensive. Laser-cutting provides a rapid method of cutting CNT wires for cross-sectional assessment, however, the local heat generated may lead to metal migration and/or flaring of the CNT bundles in the network, distorting the cross-sectional area. Razor slicing also offers the advantage of speed, however, may disturb the morphology of the cross-section area by pulling out CNTs, and distorts the area through compression. As such, each of these techniques presents their own challenges. Therefore, careful consideration must be made when selecting the technique, depending on the application and desired analysis.

1.4.3 Elemental Characterization (XRD, Raman, EDX)

Scanning electron microscopes are capable of performing X-ray microanalysis to determine the elemental profile present within a specimen. The technique is performed by bombarding the sample with electrons whose energies are on the order of the binding energy of the element's core electrons. The excited core electrons then relax, emitting photons in the X-ray range. The amount of orbital shells and occupancy of the subshells within the host atom dictate the amount of energy required to excite the electron. Thus,

each element can be uniquely identified by collecting the characteristic X-ray emission using a detector that is equipped on the SEM. This technique, referred to as energy dispersive spectroscopy (EDS), is useful for analyzing the carbon and metal distribution in the CNT hybrids.

Another X-ray related technique that can be used to identify the presence of specific elements is X-ray diffraction (XRD). In compliance with the Bragg condition, an X-ray beam of a particular energy is directed at a crystalline sample and undergoes constructive interference at allowed diffraction angles dependent on the lattice spacing. The sensitivity of this technique to the lattice parameters provides characteristic measurements for elements as well as compounds such as oxides. Thus, XRD can help determine whether the deposition of metals onto CNTs results in a metallic film, or forms carbides/oxides.

A third spectroscopy technique, which is powerful for probing low-frequency modes (e.g. vibrational and rotational), is Raman spectroscopy. In this case, incident radiation in the visible, near-UV, or near-IR region is inelastically scattered (i.e. the photons exhibit a different energy upon scattering) with an energy shift related to the molecule's nuclear vibrations. Molecules may exhibit multiple types of vibrational states which may be unique to the molecule, enabling the identification of compositional information as well as crystallinity of a structure. In the context of CNTs, the relative defect ratio can be revealed through the presence of the D peak, as phonons responsible for this signal are forbidden in sp^2-bonded carbon. Additionally, the presence of certain carbides and oxides can be identified by their vibrational modes, enabling this technique to determine the state of certain metal films deposited onto the CNTs, lending insight

toward the bonding characteristic of the metals with the CNTs. In general, the variety of characterization techniques described above are paramount for understanding the metal:CNT interaction, and helps to identify the compatibility of the different metals with CNTs.

1.5 Interaction of Metals and CNTs

1.5.1 CNT-Metal Compatibilities

An issue that arises with the integration of certain metals, such as Cu, is their poor adhesion when deposited onto CNTs [45, 62], which prevents full utilization of the potential electrical benefits provided by the hybrid conductors. A qualitative indication of the wettability of metals on CNTs is the morphology that they take upon deposition, which can be observed using SEM or TEM. The morphology of a fairly thorough survey of metals as deposited onto individual CNTs has been performed by Zhang, et al, in 2000 [63, 64]. Specifically, Ti, Ni, Pd, Au, Al, and Fe were deposited at 5 nm and 15 nm thicknesses using e-beam evaporation. Ti is shown to exhibit the best wettability amongst the metals studied, as it deposits uniformly and continuously along the CNTs. Ni and Pd are also shown to deposit mostly continuously, in the form of discrete particles, with some degree of interruptions along the length of the coating. Au, Al, and Fe, on the other hand form discrete islands as deposited. In fact, the size of the deposited Au clusters have a bigger diameter than the thickness of the deposited coating, indicating migration of the Au to minimize surface energy.

The deposition dynamics are largely dependent on the interaction between the substrate and the condensate. The diffusion rate of adatoms on a surface is proportional to the energy required for diffusion (E_{diff}) by $\exp(-E_{diff}/k_BT)$, where k_B is the

Boltzmann constant, and T is temperature [65]. Thus, a lower diffusion energy results in a higher rate of diffusion. The diffusion energy has been empirically determined to be proportional to the binding energy, E_B, as $E_{Diff} \sim E_B/4$ [65]. Accordingly, a strong binding energy between the two constituents results in slow surface diffusion, which results in a higher nucleation density. A weak binding energy, otherwise, permits fast surface diffusion such that adatoms can find already formed nucleation centers and merge to induce island growth. Thus, the morphology observed for the deposited metal atoms on CNTs gives qualitative insight toward their binding energy and interaction.

Attempts to explain the interaction between CNTs and metals has proven challenging, and groups have focused on correlating a variety of different parameters to explain the behavior observed. For example, Zhang, et al, explained the results observed in their evaporation studies described earlier [63, 64] based on the reactivity of bulk carbon with the respective metals. Metals can interact with carbon in a variety of ways. Fe, for example, is capable of dissolving carbon well for catalytic applications, while Ti limits the mobility of the carbon as it locks the carbon into a carbide [66]. Metals like Cu are otherwise inert to carbon. The range of interactions is explained by the bonding behavior between carbon and the respective transition metals, for which, the carbon p-orbitals tend to overlap with the corresponding metal d-orbitals. A general trend has been noted by Sung, et al, that an increasing amount of d-orbital vacancies in transition metals is correlated to an increase in melting point temperature of their respective bulk carbides (see Table 1), as well as the maximum carbon solubility [66]. A higher melting point is generally indicative of strong bonding energy. Furthermore, carbon solubility is indicative of the reactivity of the metals with carbon. Thus, metals like Ti, which have 8

d-orbital vacancies, react very readily with carbon to form carbides, and as such have limited solubility. Metals like Fe and Ni, on the other hand, are capable of dissolving a substantial amount of carbon without fully locking up in carbides, due to their moderate reactivity [66]. Lastly, metals like Cu have very limited interaction with carbon and exhibit no carbon solubility as a result.

Metal	Vacant 4s and 3d orbitals	Carbide	M.P. (°C)	Solubility of C in Metal
Sc	9	ScC_2	—	0.7
Ti	8	TiC	3067	1.2
V	7	VC	2648	9.1
W	6	WC	2776	8.4
Cr	5	Cr_3C_2	1810	9.1
Mn	5	Mn_7C_3	1340	8.9
Fe	4	Fe_3C	1227	14.7
Co	3	Co_3C	—	9.0
Ni	2	Ni_3C	—	5.2
Cu	0	—	—	3.6
Zn	0	—	—	2.4

Table 1: A list of metals and their corresponding number of d-orbital vacancies, as well as the melting point for the respective stable carbide types. Lastly, effective eutectic solubilities at 1000 °C for C in molten transition metals. All data obtained from Sung, et al [66].

The reactivity of metals with carbon is an important factor regarding the expected bonding and adhesion characteristics. However, the electrical interaction between metals and CNTs is another critical factor when considering their use for fabricating hybrid conductors. A primary consideration is the contact resistance between the metals and the CNTs, which can arise from the tunneling barriers generated by work function mismatch [67, 68] as well as the contact geometry [69]. Furthermore, the electrical contact can be influenced by adsorbates present on the CNTs, which modify the local density of states

(DOS) [70–72]. Adsorbates can arise from atmospheric or environmental exposure, whereby the CNT's non-localized π-electrons enable the sidewalls to form weak van der Waals bonds with ambient molecules. Such adsorbates have been reported to measurably influence the electrical conductivity of CNTs [73, 74], and in some cases decrease the contact resistance [75].

More generally, however, wetting geometry imparts a significant role in contact resistance between metals and CNTs. It is reported that, with poor wetting, the contact area between the metal and the CNT decreases, and the work function difference dominates the resistance [67]. Thus, these two factors must be considered when assessing metal-CNT compatibility for electrical interfacing. Lim, et al., created a plot of metal-CNT contact resistances versus the work function of the metals [67]. While Ti deviates from the typical range of CNT work functions, it exhibited the lowest contact resistance as a result of its excellent wetting to CNTs. Metals like Cu, on the other hand, exhibited moderate contact resistance, despite having a matched work function, due to its poor wettability.

As mentioned previously, good wettability has been associated with a high amount of d-orbital vacancies. This trend has been observed for contact resistance as well, in a study performed by Liebau, et al [76]. In this study, individual CNTs were contacted by either Au/Fe, Pd, or Co electrodes to measure contact resistance via a two-point probe method, which measures the intrinsic CNT resistances as well as the contact resistances. A four-point probe method was used to measure the intrinsic resistance of 5 individual CNTs, which would serve as the CNT contribution to the resistance obtained via the two-point probe measurements. In the case of the Au/Fe electrode, the CNTs

exhibited the highest resistances measured (20 MΩ – 2.5 GΩ). Pd exhibited much lower resistances, between 70 – 450 kΩ. Co contacted CNTs, having the most d-orbital vacancies, resulted in resistances below 150 kΩ. This demonstrates a trend that higher metal d-orbital vacancy leads to improved contact resistance with CNTs, both of which have previously been correlated with good wettability.

Metals with the highest conductivities often have few to no d-orbital vacancies (such as Ag and Cu), and thus, interact poorly with CNTs. Therefore, when preparing bulk metal-CNT hybrid conductors, an interfacial layer is necessary to improve the contacting and interaction between the CNTs and the respective conductive metal coating. Table 2 shows a summary of all the important considerations to bear for metal-CNT conductor design, with metals ordered by their number of d-orbital vacancies. A green cell indicates properties that are well aligned with intermixing of metals and carbon, and suitable for high performance. Yellow cells indicate limited interaction or performance, while red indicate very poor interaction or performance. Information for some metal:CNT interaction properties are not readily available and are shaded grey. Based on the collection of reported values, metals such as Al, Cu, Au, and Ag, while highly conductive, will require an interfacing component if to be used with CNTs. Ti and Ni are two candidates that stand out as promising adhesion metals, with overall good compatibility with CNTs. As such, Ni and Ti have been selected for evaluation herein.

Property	σ (MS/m)	α_{300K} (10^{-3} K^{-1})	Wettability	Carbide (Max. C/M)	d-orbital vacancies
Al	37.7	3.9	Non-uniform[c]	Non-stable[d]	
Cu	58.7	3.83	145° Contact angle[k]	0/1[h]	1[f] 0[h]
Au	44.2	3.4	Non-uniform[c]	Non-stable[d] 0/1[h]	1[f]
Ag	62.1	3.8	~125° Contact Angle[g]	0/1[h]	1[f]
Pd	9.46	3.79	Partially uniform[b,c]	0/1[h]	2[f]
Ni	14.3	5.9	Mostly uniform[c]	1/3[h]	2[f,h]
Pt	9.26	3.92	Discrete[b]	0/1[h]	2[f]
Rh	23.1	4.57	Small nodules[j]	0/1[h]	2
Ru	14.3	2.71	Small particles[j]	0/1[h]	3
Co	17	6.0		1/3[h]	3[h]
Fe	10.3	5.67	Non-uniform[c]	1/3[h]	4[f,h]
Cr	7.9	3.0	Reduces Cu contact angle to 40° [i]	2/3[h]	6[f] 5[h]
W	17.9	4.5	Highly uniform[l]	1/1[h]	6
Ta	7.7	3.8		1/1[h]	7
Ti	2.38	3.8	Highly uniform[c]	1/1[h]	8[f]

Table 2: A summary of metal, carbon, and metal-CNT properties reported in the literature. Values obtained from reports are referred to accordingly: a [18], b [77], c [63], d [78], e [69], f [79], g [80], h [81], i [82], j [83], k [84], l [85].

1.5.2 Ni Compatibility for CNT Hybrids

Previous studies have shown that Ti and Ni have favorable wettability on CNTs, as well as good electrical contact [63, 86], whereas metals such as gold, aluminum, and iron show poor wetting properties[63]. In the case of Ni, Menon et al. found computationally that the curvature of the CNTs can promote rehybridization of the carbon sp^2 orbital with the Ni d-orbital, altering the bonding characteristics from that experienced between Ni and bulk carbon [87]. This motivates the use of Ni for use in bulk metal-CNT hybrid conductors.

Zou et al. used electrodeposition to fabricate a bulk Cu-Ni-CNT conductor consisting of a nanoscale Ni layer and a 2 μm thick Cu layer. Samples were annealed in Ar for 30 minutes at 300 °C, resulting in a conductivity greater than 20 MS/m, and a temperature coefficient of resistance as low as 1.14×10^{-3} K^{-1} [62]. Zou et al. showed via cross-sectional electron microscopy that an annealed Cu-CNT conductor fabricated without a Ni adhesion layer resulted in microgaps at the Cu-CNT interface, due to poor wettability of the Cu. With the use of a Ni buffer layer, however, a well-connected interface was formed, demonstrating the ability of Ni to interface well with CNTs. However, another important aspect to note is that the Ni diffuses through the Cu layer due to the mutual compatibility of the metals, as evidenced by an EDX line scan.

The impact that annealing has on the diffusion of Ni within the Cu layer was further illustrated using surface EDX mapping, whereby the Ni signal became more homogeneous after annealing. This can have a variety of consequences on the electrical properties of Cu. For example, a previous study has shown that the conductivity of electrodeposited Ni-Cu alloys decreases with increasing Ni content [88]. In this case,

diffusion of Ni into Cu should be limited. On the other hand, constantan is a Ni/Cu (~45%/55%) alloy, which is known for its extremely low TCR of ~5.0×10^{-6} K^{-1} [89]. Thus, the observed low TCR for this Cu-Ni-CNT hybrid may be partially benefited by the diffusion of the Ni into the Cu layer, although the true origin of this low TCR is not fully understood. In this paper, it is speculated that partial elastic scattering at the surface could possibly be reducing the TCR, however no evidence is provided. Regardless, Ni is shown to interface well with CNTs as well as Cu, showing promise from a wettability standpoint.

Milowska et al. have studied the interaction between Cu, Ni, and Cr with CNTs as deposited (via magnetron sputtering) and after exposure to elevated temperatures (ranging from 400 to 1000 °C) [45]. Electron microscopy images indicate that melting of the Cu is observed at temperatures as low as 400 °C, leading to severe de-wetting at 600 °C, and eventually evaporation at 1000 °C. In the Cu-Ni-CNT system, however, significant beading was not observed until 800 °C, with Ni remaining at 1000 °C after the Cu evaporates. Furthermore, some amount of metal was visible beneath the CNT surface in the Cu-Ni-CNT, suggesting a much greater interaction between the metals and the CNTs. However, the high degree of interfacial interaction provided by the Ni comes at the cost of degradation of the CNT structure. Milowska et al. measured higher D/G ratios for the Cu-Ni-CNT system as the annealing temperature increased, attributed to the solubility of carbon in Ni (which is corroborated by EDX measurements). The solubility of carbon within the Ni is decreased with the presence of Cu, and thus, while Ni provides great surface interaction with CNTs, careful considerations must be made regarding applied temperatures and metal combination selection.

1.5.3 Ti-CNT Interaction

Ti is among the most reactive metals with CNTs, indicating superior wettability [63] and binding [66], as well as electrical contact [67]. Computational studies performed by Yang et al. investigated the adsorption of continuous Ti, Au, and Al chains (linear connection of metal atoms) on various SWCNT surfaces and found that Ti is energetically more favorable [90]. Their *ab initio* calculations determined binding energies of 0.25 eV/metal atom and 0.52 eV/atom for Au and Al, respectively, while Ti had binding energies as high as 2.04 eV. Moreover, it was found that the Ti chain imparts a DOS at the Fermi level for the Ti deposited SWCNT, giving rise to metallic behavior for an otherwise semiconducting SWCNT. First principle calculations were also carried out on the bonding distance and electrical contact properties of metals on graphene and SWCNTs by Matsuda et al. [91]. Ti was shown to exhibit the smallest bonding distance on graphene at 2.17 Å, and a high binding energy of 2.09 eV. Further calculations were conducted for (13,0) SWCNTs, resulting in an even smaller bonding distance of 2.11 A, attributed to the curvature of the SWCNT. Matsuda's calculations determined that the interaction between the d-orbitals of the metals and carbon's pπ orbitals have a critical impact on the electrical and bonding characteristics imparted to the metal-CNT systems. Electrical characteristics were probed by constructing I-V models to calculate the contact resistances of the metals with the CNTs. Ti was found to have an extremely low contact resistance on (7,7) SWCNTs of 6.9 kOhm/nm, an order of magnitude lower than the next best contact resistance found (63.7 kOhm/nm for Pd-SWCNT). Overall, computational studies have good agreement that Ti has highly favorable characteristics as deposited on CNTs.

Zhang et al. also provided experimental evidence of the strong adhesion between Ti and CNTs [63, 64]. As mentioned previously, Zhang coated individual CNTs with various metals and found that Ti forms continuous coatings along the surface of the CNTs [63]. In a follow up study, they coated CNTs with 1 nm of Ti and investigated the coating properties of various other metals deposited onto the Ti-CNT system [64]. Electron microscopy images showcased that 5 nm coatings of Au, Pd, Fe, Al, and Pb onto individual SWCNTs resulted in mostly discontinuous coatings as deposited. However, a 1 nm Ti adhesion layer was capable of significantly improving the wettability of all metals studied, resulting in nearly continuous coatings for even the least compatible metals.

Experimentally, the use of a Ti layer on CNTs has also been prevalent in nanoelectronics, whereby Ti improves the contact resistance between CNTs and their respective substrate [92, 93]. Srividya et al. found that as-grown vertically aligned CNTs using an Fe catalyst exhibited poor adhesion with a Si substrate (with CNTs detaching from the surface), whereas a Ti buffer layer provided sufficient support to maintain adhesion of the CNTs [93]. Additionally, it has been reported that the high CNT-substrate contact resistance can lead to excessive Joule-heating, eventually damaging/evaporating the CNTs, resulting in a reduction in emission current for the CNT devices [94]. This effect is witnessed in the CNT devices that Srividya et al. fabricated without the Ti adhesion layer. However, the use of a Ti adhesion layer maintains a stable emission current for extended periods of time, attributed to the lowering of the contact resistance from the Ti-CNT interface (resulting in less Joule-heating).

Additionally, in a study performed by Chu et al., Ti was shown to exhibit strong interfacial interaction in a Cu-Ti/CNT metal composite matrix while having no negative impact on electrical conductivity with up to 15% CNTs by volume [95]. In this study, Cu-Ti/CNT composites were prepared via mechanical ball milling of either Cu or prealloyed Cu-Ti (0.85% Ti, 8-20 μm in size) powders and MWCNTs. The prepared composites consisted of 0, 5, 10, and 15% wt CNTs and were tested for yield strength and electrical conductivity. A measurably higher yield strength was evident for the Cu-Ti/CNT composite and is attributed to a couple of factors. Namely, the presence of Ti itself can slightly improve the resistance to plastic deformation by impeding the movement of lattice dislocations. Moreover, Chu et al. observed the presence of TiC (111) lattice fringes via HRTEM imaging, the presence of which may significantly improve the interfacial interaction between the Cu and the CNTs and the corresponding load-transfer ability. Furthermore, while the yield strength is improved significantly with the presence of a Ti buffer, the electrical conductivity is unaffected. This suggests that Ti is a very effective adhesion metal for use in Cu-CNT composites, which can improve the interfacial interaction without negatively impacting the electrical performance.

2 Opportunities for Advancement & Dissertation Goals

2.1 Evaluation of Adhesion Metals for Metal-CNT Hybrid Conductors

Ti and Ni have shown promising adhesion properties as-deposited, however, studies to date have focused on room temperature electrical variation and microscale behavior, whereas understanding how adhesion metals on bulk networks are stable at increased temperature due to operation conditions (such as motors) or under increasing applied current [7, 27] is warranted. As highlighted earlier, Milowska et al. have studied

the effects of high-temperature annealing (400 °C to 1000 °C) on Cu-Ni-CNT composites, finding that the Ni experiences a complex solubility with both Cu and CNTs [45]. The effectiveness of Ti as an adhesion layer for conductive Cu-CNT hybrids at elevated temperatures is yet to be reported. In fact, there has been very limited research in general investigating the use of Ti as an adhesion layer for bulk metal-CNT hybrid conductors. Much of the research to date on Ti-CNT structures are based in microelectronics or MMC's for mechanical purposes, which have demonstrated the clear advantages that Ti shows as an electrical interface for CNTs. Utilizing Ti as an adhesion layer for metal-CNT hybrids could offer the advantages of improving wettability of conductive metal overcoats as well as provide an electrical interface capable of allowing charge transfer due to its low contact resistance with CNTs.

2.2 Scalable Fabrication Methods Towards Ti-rich Integrated Conductors

One of the critical challenges with integrating Ti into bulk CNT networks is the high reactivity of Ti and its corresponding tendency to form oxides. As a result of its high reactivity, electrodeposition of metallic Ti is particularly challenging, often resulting in depositions of various Ti compounds based on the media used [96–98]. Therefore, PVD techniques offer an easy route for the deposition of pure Ti. However, due to the limited penetrability of PVD techniques, they are not a viable solution for fabricating integrated metal-CNT conductors. Joule-heating CVD based delivery offers a promising route toward the fabrication of integrated Ti-CNT conductors, with the advantage of maximizing metal-CNT interfacial area for enhanced interaction. There has been limited work on the deposition of pure Ti onto bulk CNT networks through the Joule-heating CVD method, as the technique is relatively recently developed for bulk CNT networks..

Such a technique would be suitable as a scalable fabrication method for fully integrated Ti-CNT conductors, which can then be processed further to bridge the CNT bundles and junctions with highly conductive metals that are typically incompatible with CNTs. Ultimately, CVD deposited Ti-CNT conductors can enable the fabrication of high-performance metal-CNT hybrids, mitigating the connectivity issues, improving their temperature stability, and enhancing their electrical performance.

2.3 Dissertation Objectives

The aim of this dissertation is to optimize the fabrication of 3D Cu-Ti-CNT hybrids for development of highly conductive, temperature-stable wires with favorable temperature dependent electrical properties to provide energy savings in elevated temperature applications. Developing an understanding of the relationship between metallization processing conditions and resultant material characteristics is key for the fabrication of high performance metal-CNT hybrids. The major focus areas in this dissertation are subdivided below:

1. Evaluation of the electrical performance, temperature stability, and wettability of 2-D Ti and Ni as adhesion metals for bulk Cu-CNT conductors via thermal evaporation.
2. Fabrication of high conductivity 3-D Cu-Ti-CNT hybrids combined with low TCR by means of a Joule-heating CVD technique and electroplating.
3. Demonstration of Ti-rich depositions achieved via development in CVD processing conditions. Assessment of the influence of CVD conditions on the nanoscale interconnection characteristics by employing temperature-dependent electrical modeling.

3 Evaluation of Ti and Ni as Adhesion Metals

Objectives

- Assess the morphology of Ti and Ni deposited onto CNTs via thermal evaporation.
- Determine the stability of 10 nm Ti and Ni layers, and 100 nm Cu layer, on CNTs after exposure to elevated temperature
- Study the electrical properties of Cu-M_A-CNT hybrids and their temperature stability.

3.1 Thermal Evaporation and Annealing

The use of physical vapor deposition (PVD) can be employed for metalizing CNT networks through methods such as thermal or e-beam evaporation [40–43] and magnetron sputtering [44–48]. In our recently published work, a thermal evaporation technique was used to deposit thin metal films onto a CNT conductor, followed by annealing, for assessing adhesion via scanning electron microscopy (SEM) analysis and electrical characterization [99]. PVD was selected as a means to achieve a well-defined thin-film interface for assessing the benefits of an adhesion layer towards scalable designs. Samples were annealed at temperatures between 100 °C and 400 °C, a temperature range which could be reached during the operation of motor applications or during fabrication of the Cu-CNT conductors [27]. Furthermore, temperature-dependent electrical measurements were conducted from 26.85 °C to 326.85 °C (300 K to 600 K) to understand the permanent electrical effects that processing at elevated temperatures has for the various hybrid conductors. Identification of a conductive adhesion metal for the Cu-M_A-CNT is critical for designing hybrid conductors, which can eventually replace conventional conductors in applications in which they are exposed to elevated temperatures. The following work in this section has been reprinted with permission from (McIntyre, D. J., et al, Enhanced Copper–Carbon Nanotube Hybrid Conductors with

Titanium Adhesion Layer, *Journal of Materials Science* 55 (2020): 6610-6622).

Fabrication and processing

Miralon® roving from Nanocomp Technologies Inc. (a Huntsman International LLC. company) is used as the carbon nanotube conductor in this study. The roving product is produced on the kilometer scale [100] and is obtained prior to the yarn spinning process, yielding a ribbon-like form (~30 μm × 1.53 mm) with an average density of 0.12 g cm^{-3}. The width of the roving product has a standard deviation of 20%, based on 360 width measurements taken over ~ 50 cm via optical microscopy. A 10 ± 1 nm-thick adhesion metal layer of either Ni (99.98% purity pellets) or Ti (99.995% purity pellets) was deposited onto the CNT ribbons via thermal evaporation (Kurt J. Lesker PVD 75) under a vacuum base pressure of < 10^{-6} mbar and a deposition rate of 3.5 ± 0.5 Å s^{-1}. All metal pellets were obtained from Kurt J. Lesker. Deposition rate monitoring was carried out using a quartz oscillating crystal to obtain effective film thicknesses. The samples were subsequently removed from vacuum and separately subjected to a 95% Ar / 5 % H_2 anneal in a Lindberg/Blue M(HTF55322A) tube furnace at temperatures of 100, 200, 300, and 400 °C for 1 hour (as depicted in Figure 4). After the corresponding anneal, thermal evaporation of a 100 ± 2 nm Cu layer (99.99% purity Cu pellets) was then performed at a deposition rate of 10.0 Å s^{-1}. Control samples were generated with and without the adhesion metal layer. After copper deposition, the Cu-M_A-CNT conductors were annealed to the same temperature and gas conditions as the first annealing step. The fabrication sequence involving a break in vacuum between deposition of the adhesion metal layer and the copper layer is referred to here as the

"two-step" deposition process. An additional set of samples were fabricated by depositing the adhesion metal layer and copper layer sequentially, without breaking vacuum, referred to as the "one-step" deposition process.

Characterization

Analysis of film morphologies was performed using a Hitachi S-900 scanning electron microscope (SEM) equipped with a secondary electron detector and biased at 2 kV accelerating voltage. Current-voltage sweeps (up to 100 mA) were conducted in an ambient atmosphere at room temperature using a four-point-probe configuration with a National Instruments NI PXI-5652 source/measure unit and NI PXI-4071 digital multimeter. The probe tips were bent in a configuration that applies firm contact but prevents penetration through the top layers of the samples (i.e. a dull contacting point rather than a sharp contacting point). Temperature-dependent electrical measurements were performed in a Janis cryostat under 10^{-6} mbar vacuum. Two cycles of temperature sweeps over 26.85 – 326.85 °C (300 – 600 K) were performed with four-point probe I-V sweeps being carried out at 5 °C increments. A National Instruments NI PXI-4110 programmable power supply and NI PXI-4072 digital multimeter were used to acquire the electrical measurements.

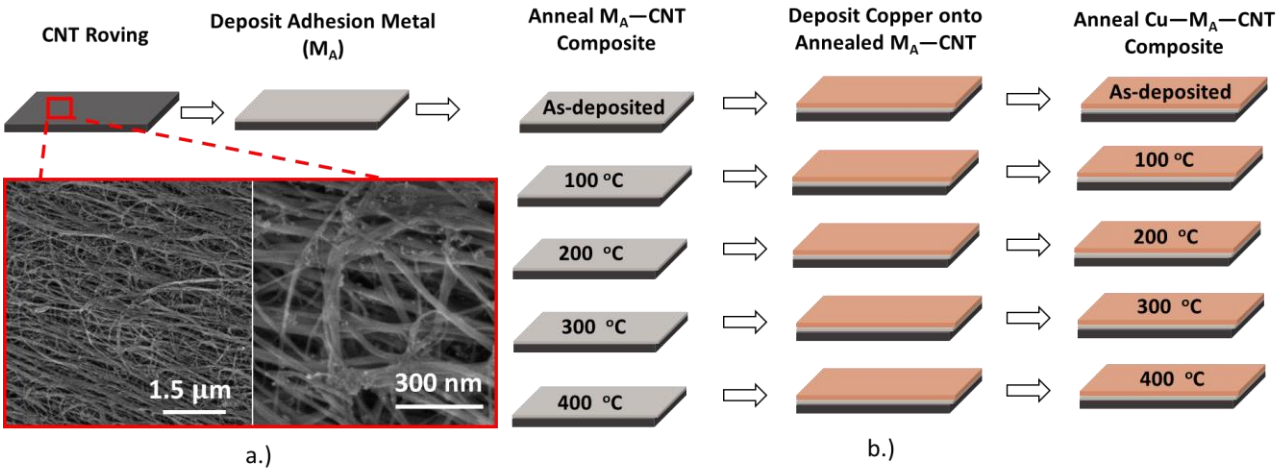

Figure 4 (a.) SEM images of the starting CNT conductor material. (b.) Experimental process for studying the CNT-metal interfacial interactions [99].

SEM Analysis

The SEM image in Figure 4a was acquired from the surface of the CNT conductor used in this study, showing the network morphology of the CNT bundles. The presence of residual iron catalyst and carbonaceous material from synthesis is visible. The porosity of the network on the nanoscale enables infiltration of the metals and a greater surface area for deposition. Meanwhile, the planar ribbon geometry of the material provides a relatively flatter surface for line-of-site metal deposition than a wire-like format.

The processing steps used for the study of adhesion metals are summarized in Figure 4b. Additionally, as a point of comparison for the Cu-M_A-CNT conductors, a Cu-CNT conductor was fabricated and subjected to the annealing steps. The SEM images in Figure 5 show the morphology of a 100 nm Cu layer directly deposited onto the CNT conductor followed by subsequent annealing treatments at 100, 200, 300, and 400 °C. The morphology at each processing step was analyzed and compared against electrical measurements to quantify the performance of the Cu-CNT system. The annealing sequence performed on the Cu-CNT conductor provides a benchmark by which the

performance of the Cu-M_A-CNT may be compared. Due to its thickness, the Cu layer initially forms a continuous film along the CNT network as-deposited, with an average grain size of 58 ± 6 nm measured based on SEM images. A gradual evolution of the Cu grain structure is observed upon exposure to elevated temperatures. At an annealing temperature of 100 °C, the onset of grain growth is observed with grain size increasing to a measured 71 ± 1 nm. As the temperature is increased to 200 °C, more evident coalescence is observed as the average grain size increases to approximately 137 ± 9 nm. Grain growth appears to peak toward an average size of about 167 ± 7 nm at temperatures of 300 °C. Similar grain growth effects have been observed on nanocrystalline Cu thin films sputtered onto Cu substrates, whereby grain growth is observed at temperatures as low as 100 °C and increases at temperatures of 300 °C [101]. However, the Cu grain size appears to decrease for the 400 °C anneal, with an average size of 121 ± 7 nm. The reduction in size is attributed to the Cu layer beginning to discretize, confining the area for grain expansion. This is accompanied by delamination into an independent film, consistent with a previous report in the literature, where melting of thin Cu films on MWCNTs was observed at temperatures of 400 °C [45], and attributed to nanoscale induced melting point depression [102]. Furthermore, poor wettability is evidenced by the non-coated CNTs becoming visible between gaps generated during delamination in the post-annealed Cu layer (as shown in Figure 5e). The observed delamination indicates a need to introduce an adhesion metal to the Cu-CNT conductor to improve the stability of the Cu overlayer when exposed to high temperatures. For applications in which the conductors operate at elevated temperatures, the electrical performance of Cu-CNT wire technologies must be stable upon exposure to these increased temperatures.

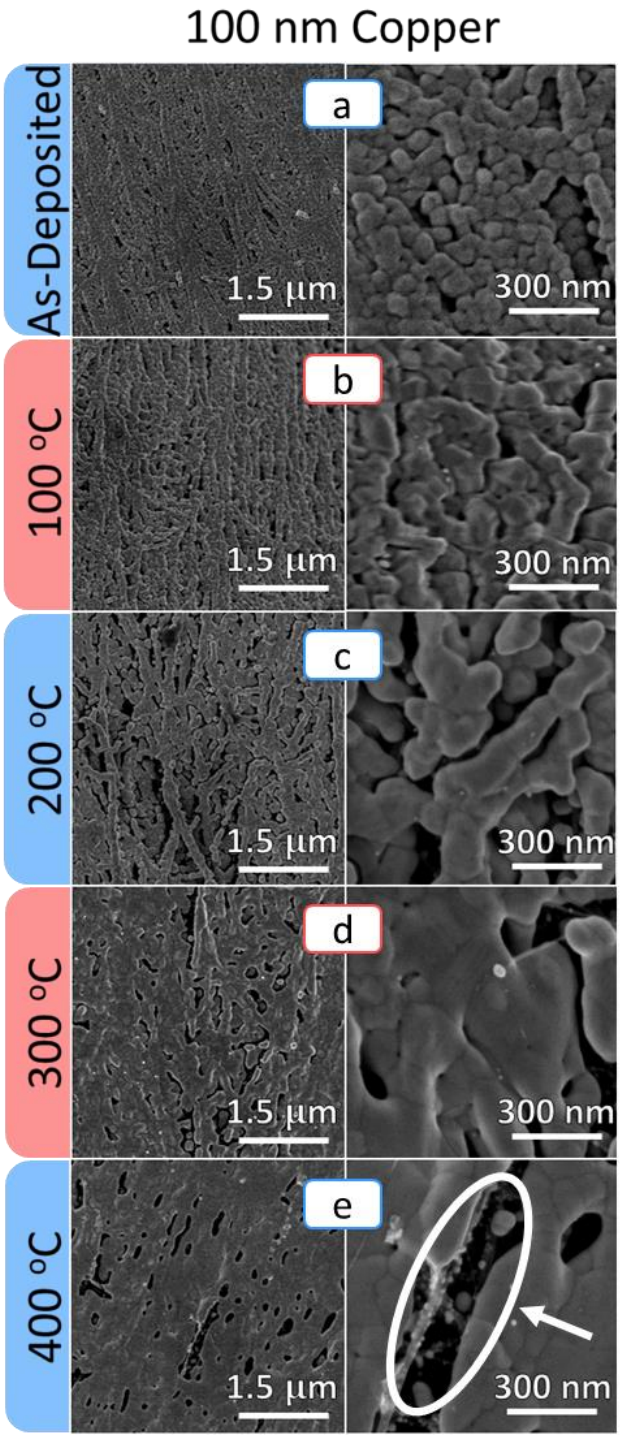

Figure 5 SEM images of (a) as-deposited 100 nm Cu with samples separately annealed at (b) 100 °C, (c) 200 °C, (d) 300 °C, and (e) 400 °C for 1 hour under 95% Ar / 5% H_2 environment. Circled region with arrow indicating the presence of exposed CNTs [99].

Figure 6 shows SEM images of the CNT conductor after deposition with 10 nm of Ni thermally evaporated and after a 1 hour anneal in 5% H_2 / 95% Ar at different temperatures. From Figure 6, the gradual formation of discrete structures by the 10 nm thick Ni can be observed as the temperature is increased to 400 °C. The as-deposited Ni layer consists of well-distributed nanocrystallites, giving it a textured appearance. The nanoscale textured surface features have been attributed to fast surface diffusion of adatoms upon deposition, implying a low diffusion activation energy (i.e. weak binding energy) characteristic of poor condensate-substrate interaction [65]. As the annealing temperature is increased to 200 °C, the Ni layer begins to coalesce together. As the temperature further increases to 300 °C, the layer continues to discretize, and Ni island formation occurs. At 400 °C, the Ni island formations evolve into larger isolated particles, which is attributed to Ostwald ripening effects, whereby the Ni atoms reduce their total interfacial energy with the CNTs via coalescence into larger particles, minimizing the total surface area due to poor interaction with the CNTs [103]. Such a phenomenon has previously been observed for nanoscale Ni on TiO_2/n-Si substrates, whereby temperatures as low as 300 to 500 °C were found to induce dispersed island formation for Ni thicknesses up to 8 nm as a result of Ni atoms being weakly bound to the substrate [103]. Thus, the textured surface after deposition, combined with the discrete particle formation observed upon annealing in this study, demonstrate characteristics of weak binding of Ni with CNTs.

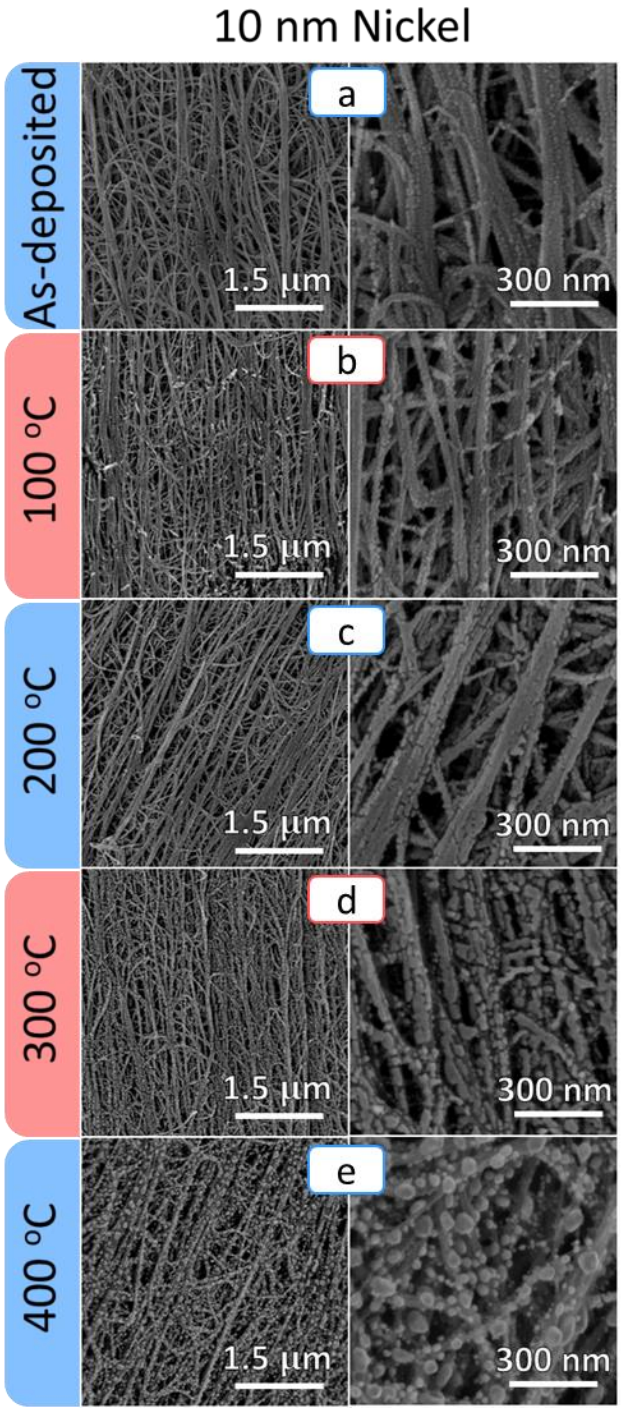

Figure 6 SEM images of (a) as-deposited 10 nm Ni with samples separately annealed at (b) 100 °C, (c) 200 °C, (d) 300 °C, and (e) 400 °C for 1 hour under 95% Ar / 5% H_2 environment [99].

Figure 7 shows SEMs of the samples with 10 nm of Ti thermally evaporated onto the CNT conductor (and after the 1 hour anneal) at different temperatures. The SEM of the as-deposited Ti layer shows that the CNT bundles are uniformly coated when compared to the starting CNT conductor. The presence of sparse particulates is attributed to the residual iron catalyst present on the as-received CNT conductor as highlighted in Figure 1. In contrast with the observations made with the Ni deposition, the Ti layer does not exhibit visible surface irregularity upon deposition. In addition, it remains uniform upon annealing. No observable differences can be made between the Ti coating as-deposited and after annealing, suggesting favorable adhesion properties. The evolution of the coating upon exposure to temperatures up to 400 °C reveal important insight toward the effectiveness of the adhesion layers as part of conductors that will be subjected to elevated temperatures.

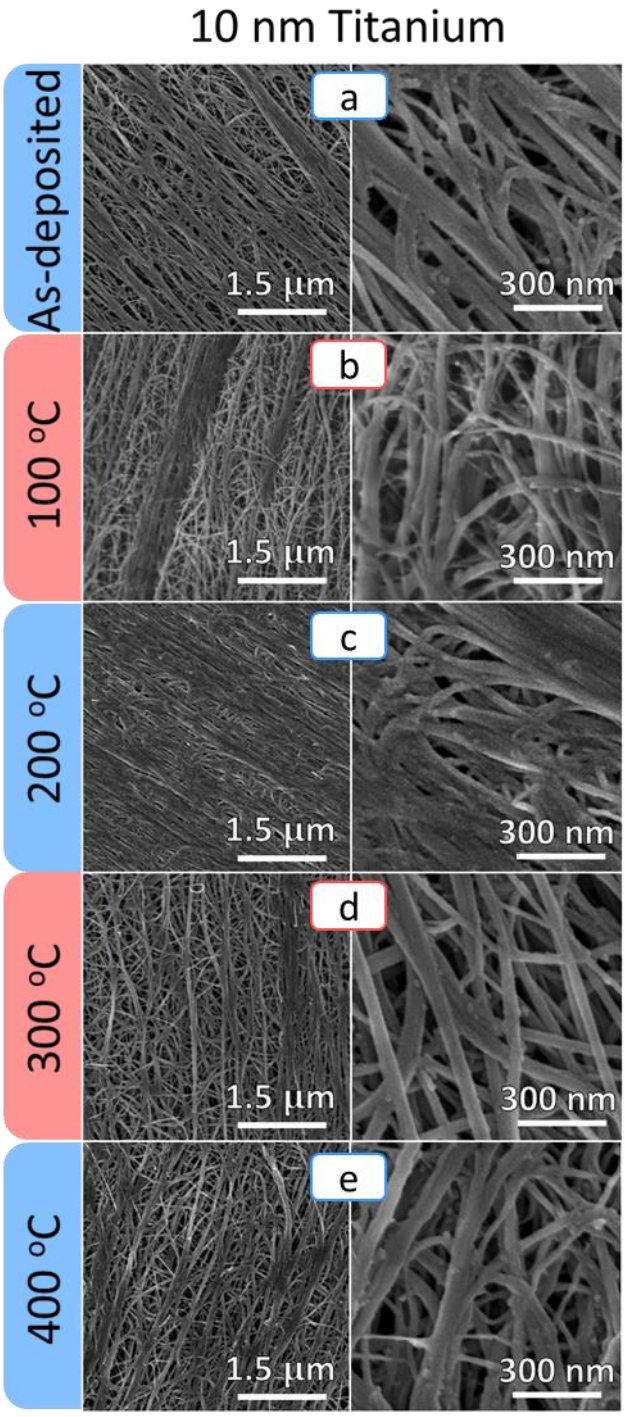

Figure 7 SEM images of (a) as-deposited 10 nm Ti with samples separately annealed at (b) 100 °C, (c) 200 °C, (d) 300 °C, and (e) 400 °C for 1 hour under 95% Ar / 5% H_2 environment, showcasing sustained uniformity [99].

After annealing the deposited adhesion metals, a 100 nm layer of Cu was then deposited to form the Cu-M_A-CNT conductors. To assess the performance of Ti and Ni as adhesion layers, the entire conductor was subjected to the same annealing treatment as performed on the underlying adhesion metal. Figure 8 shows the surface morphology of the Cu-Ni-CNT system upon exposure to elevated temperatures. In this case, exposure to 100 °C has little effect on the Cu coating, retaining the small grain size typically observed in the as-deposited state. At temperatures of 200 °C and above, grain restructuring can be seen, though with varying morphological surface features as a result of the progressive discretization of the underlying Ni layers. Contrary to the Cu-CNT system, the presence of exposed CNTs was not visible even after annealing to a temperature of 400 °C.

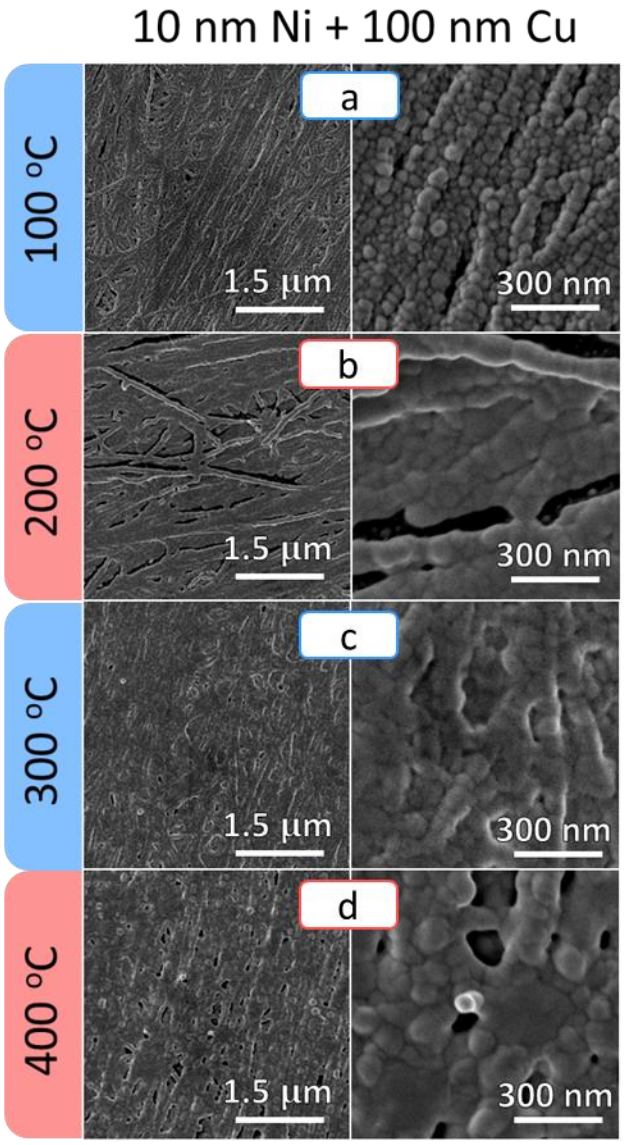

Figure 8 SEM images of an annealed 10 nm thick Ni layer overcoated with 100 nm Cu, undergoing a subsequent annealing step corresponding to the same conditions as the underlying Ni layer: (a) 100 °C, (b) 200 °C, (c) 300 °C, and (d) 400 °C for 1 hour under 95% Ar / 5% H_2 environment [99].

Figure 9 shows the progression of the surface morphology for the Cu-Ti-CNT system after annealing. Similar to the Cu-Ni-CNT system, an annealing step of 100 °C remains relatively unchanged compared to that typically observed for as-deposited Cu. The evolution of grain restructuring is also visible at temperatures above 200 °C, however, contrary to the Cu-Ni-CNT case, the surface remains relatively uniform due to

the enhanced adhesion of the Ti layer at all temperatures. The Cu-CNT system without the use of an adhesion layer demonstrates poor interaction at annealing temperatures of 400 °C, as film gap formation occurs, exposing underlying CNTs (see Figure 5e). In the case of both Ni and Ti adhesion layers, however, suppression of significant Cu delamination is observed, with no underlying CNTs exposed, demonstrating improved bonding between the Cu overcoat and the CNT conductor.

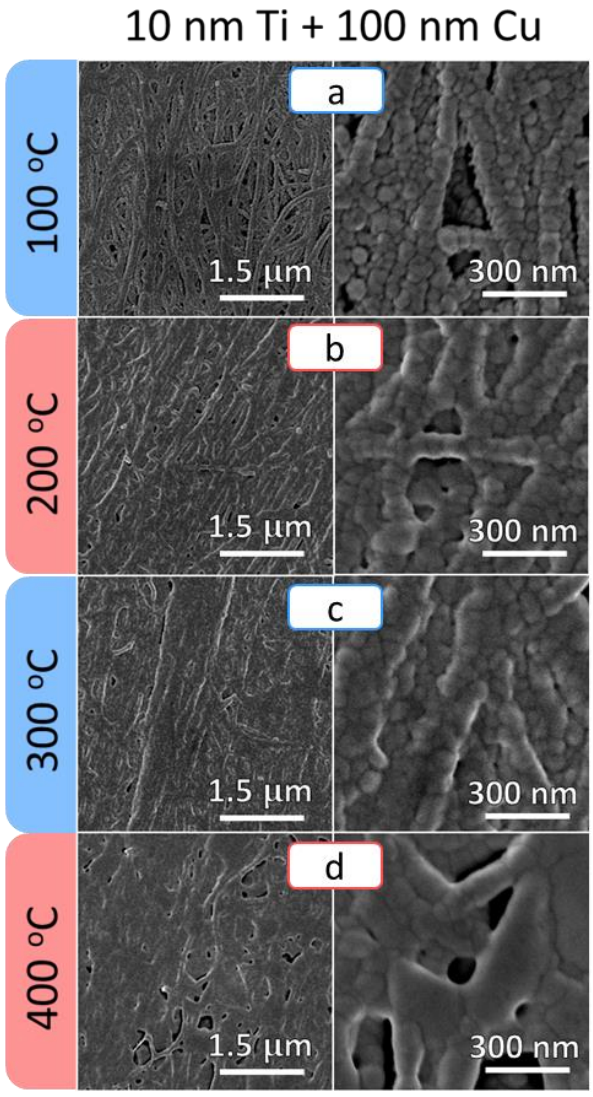

Figure 9 SEM images of an annealed 10 nm thick Ti layer overcoated with 100 nm Cu, undergoing a subsequent annealing step corresponding to the same conditions as the underlying Ti layer: (a) 100, (b) 200, (c) 300, or (d) 400 °C for 1 hour under 95% Ar / 5% H_2 environment [99].

Electrical Performance

Physical analysis via SEM shows clear changes in nanoscale morphology for the metal-CNT conductors upon exposure to the elevated temperatures, and the impact of those effects on electrical transport is measured via four-point probe measurements. The CNT conductor material starts with an average resistance per length (R/L) of ~ 340 Ω m^{-1} and increases by 8.8% after annealing at 400 °C, as seen in Figure 10. It is observed that the deposition of Cu always decreases the R/L of the conductor, as observed without the presence of an adhesion metal. Upon deposition of a 100 nm Cu layer, the R/L of Cu-CNT hybrid reduces to 140 Ω m^{-1}. However, due to the poor interaction between the Cu film and the underlying CNT conductor, there is an irreversible increase in room temperature resistance from 140 Ω m^{-1} to 200 Ω m^{-1} (40% increase) upon annealing up to 400 °C (see Figure 10). The increase in electrical resistance is attributed to the presence of gaps generated via the annealing process as observed in Figure 2e, inducing discontinuous conduction pathways [60]. Nevertheless, in all cases, this is an improvement from the as-received CNT conductor and provides a benchmark by which the electrical performance of the adhesion metals used in this study may be compared.

The resistance of the metal-CNT conductor is influenced by the width of the deposited metal layer, which is dependent on the width of the starting conductor. Therefore, the R/L values are corrected based on width measurements for each sample to ensure that the samples are directly comparable. The corrected R/L values reported for the Cu-CNT conductors have an average standard deviation of 4.6% based on measurements taken across 2-4 samples fabricated and treated under the same conditions.

Figure 10 also shows that prior to Cu deposition, the R/L of the M_A-CNT system is similar to that of the as-received CNT conductor, with the anneal temperature having no significant effect (~2% variation). The presence of a 10 nm metal layer is not sufficient to strongly influence the electrical properties of the conductor due to the bulk conductivity of the metals. The small difference observed between the two adhesion metals prior to Cu deposition likely arises due to Ni having an order of magnitude greater conductivity than Ti in bulk form (1.43×10^7 and 2.38×10^6 S m^{-1}, respectively).

The deposition of 100 nm of Cu onto the CNT conductors leads to a decreased R/L compared to that achieved from the as-deposited adhesion metals. The inclusion of a 10 nm Ni adhesion layer to form a Cu-Ni-CNT hybrid results in a slight decrease in the as-deposited R/L compared to the Cu-CNT conductor, as seen in Figure 10. However, the measured R/L of the Cu-Ni-CNT hybrid increases continuously after each anneal for temperatures up to 300 °C, followed by a sharp increase in R/L up to 309 Ω m^{-1} around 400 °C. The R/L values reported for the Cu-Ni-CNT hybrids have an average standard deviation of 6.2%.

In the case of a 10 nm Ti adhesion layer to form a Cu-Ti-CNT hybrid, a higher as-deposited R/L is observed than the as-deposited Cu-CNT conductor. On the other hand, the measured R/L of the Cu-Ti-CNT hybrid decreases after exposure to any elevated temperature, stabilizing around 166 Ω m^{-1} after being annealed to 200 °C. The R/L values reported for the Cu-Ti-CNT hybrids have an average standard deviation of 5.3%. Furthermore, the Cu-Ti-CNT conductor exhibits lower R/L than the Cu-CNT conductor after exposure to 400 °C, likely due to Cu grain expansion enabled by favorable adhesion. These results are supported by the observations made in Figure 7 and Figure 9,

which indicate that Ti maintains a continuous layer on the CNT surface, and thereby preserves the Cu layer upon exposure to any temperature up to 400 °C. As such, Ti acts as an effective conductive adhesion metal, promoting stability to the Cu film upon exposure to elevated temperatures, as well as providing an electrically superior conductor to Cu-CNT alone, achieving a stable R/L of 166 Ω m^{-1} at 400 °C.

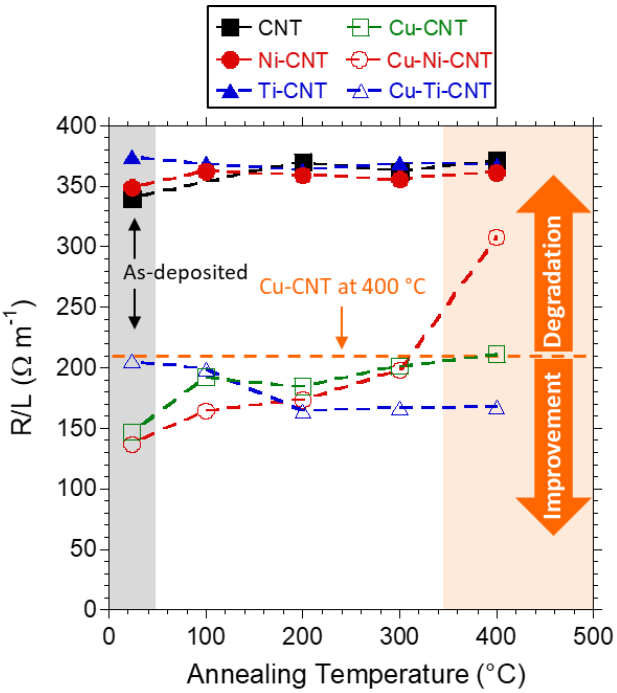

Figure 10 Electrical performance of the CNTs and metal-CNT hybrids as-deposited, and upon annealing at temperatures of 100 °C, 200 °C, 300 °C, and 400 °C for 1 hour in a 95% Ar / 5% H_2 environment [99].

Additional samples were prepared by depositing the adhesion metal and copper overcoat onto the CNT conductor in succession (without breaking vacuum between depositions), referred to here as the "one-step" deposition process. The one-step deposition process was performed to investigate if exposure to ambient conditions between depositions impacts the performance of the hybrid conductors. In the case of Cu-Ni-CNT, the one-step deposition process shows an increase in R/L from 186 to 250.9 ± 8.4 Ω m^{-1} upon annealing to 400 °C (see Figure 8a). The measured R/L for the one-step

process is also higher than the Cu-CNT conductor exposed to the same conditions, demonstrating the detrimental behavior of the Ni/Cu combination. The initial R/L of the Cu-Ti-CNT samples prepared using the one-step process are lower than those fabricated with a break in vacuum in-between deposition steps (see Figure 8b). However, after annealing to 400 °C, the final R/L still maintains 157.9 ± 11.1 Ω m^{-1}, in line with the results observed for the two-step deposition. Thus, the annealing process in a reducing environment at 400 °C is sufficient to reconcile any impact on the electrical properties induced by exposure to the atmosphere (e.g. formation of surface oxides) between deposition steps.

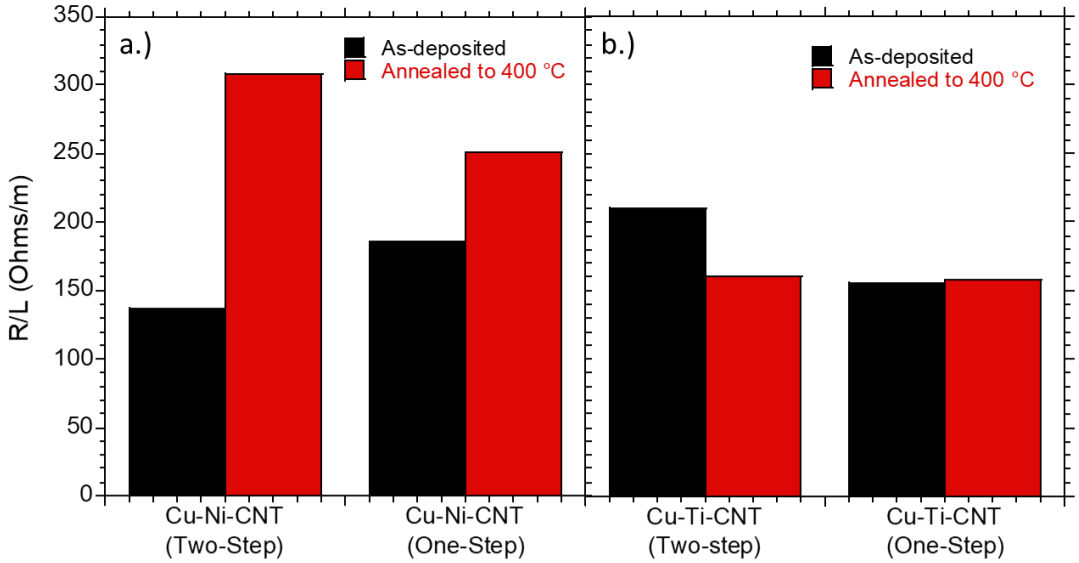

Figure 11 Electrical measurements comparing the two-step and one-step deposition processes as-deposited (black) and after annealing to 400 °C (red) for the (a.) Cu-Ni-CNT and (b.) Cu-Ti-CNT hybrids [99].

Temperature-dependent measurements of the resistance of the constructed hybrids were performed under vacuum at a constant up-ramp rate of 3.3 C min^{-1} in order to assess their stability and variability after deposition. Measuring the resistance at incremental temperatures provides complementary data to understand the dynamic changes in

electrical behavior compared to measurements after the static annealing conditions in Figure 10.

Figure 12 shows the 1st and 2nd cycle temperature-dependent resistance measurements for the CNT conductors. The resistance values are normalized to the starting resistance (R/R_0) at 26.85 °C (300 K) and show the relative change as a function of temperature. Two cycles were measured to assess any permanent effects in conductor transport due to exposure to higher temperatures. The measured R/R_0 of the as-received CNT conductor shows a non-linear behavior (see Figure 9a), as reported previously for the complex CNT electronic behavior between resistivity and temperature [104]. The 2nd cycle demonstrates that the as-received CNT response undergoes no change during the up and down ramps indicating that the sample has stabilized. The observed increase in as-received CNT starting resistance from the 1st to 2nd cycle is attributed to the reversible desorption of oxygen or other ambient dopants, after exposure to elevated temperatures, which directly influences the CNT electronic transport [105–107].

In the case of the Cu-CNT conductor (Figure 12b), the starting resistance of the 2nd cycle shows little variation from that of the 1st cycle. The lack of change under vacuum may be attributed to the presence of a CuO passivation layer, as there is no evidence suggesting that the film will coalesce into larger grains leading to more discrete particles (and increase in R/L) as compared to the annealing studies above. Additionally, the positive linearity in the slope is typical of metals, as increasing the temperature increases phonon activity, decreasing the mean-free-path of electrons, thereby increasing resistance [108].

Figure 12c shows the 1st and 2nd cycle data for the Cu-Ni-CNT conductor. The 1st cycle up-ramp shows a steady increase in resistance until around 270 °C, where the resistance begins to increase more steeply. The resistance returns to a starting resistance that is 14% higher than the starting resistance of the 1st cycle. The permanent increase in resistance upon annealing in vacuum is consistent with the trend observed for the annealing measurement data presented in Figure 10, rendering Ni an ineffective adhesion metal in Cu-Ni-CNT conductors exposed to elevated temperatures in either vacuum or reducing environments.

Figure 12d shows the temperature-dependent measurements for the Cu-Ti-CNT conductor. During the 1st cycle, a steady increase in resistance up to ~ 270 °C is observed, however, in contrast with Cu-Ni-CNT, the slope of the resistance begins to reverse as the temperature goes to 327 °C (600 K). The resistance steadily decreases to a starting resistance that is 12% lower than the starting resistance of the 1st cycle. The ability of Ti as an adhesion metal to provide a permanent decrease in room temperature resistivity when subjected to elevated temperatures in a reducing atmosphere is complemented by the measurements conducted under vacuum, whereby the resistivity of Cu-Ti-CNT conductors decreases between the 1st and 2nd cycle, further validating the benefit of Ti as an adhesion metal in elevated temperature applications.

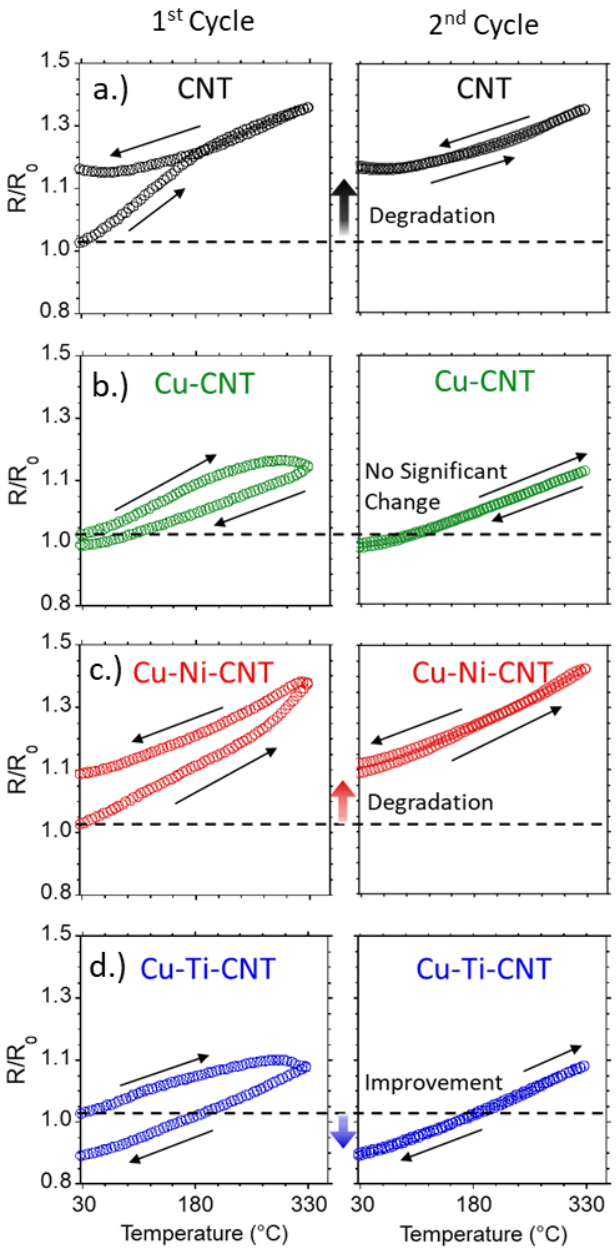

Figure 12 1st cycle and 2nd cycle temperature-dependent electrical data for the (a) as-received CNT, (b) Cu-CNT, (c) Cu-Ni-CNT, and (d) Cu-Ti-CNT conductors. Resistance values are normalized to the start of the first cycle at ~~300 K~~ 26.85 °C (300 K). Narrow black arrows correspond to the ramp direction, while the wider arrows compared to the dashed lines indicate the change in room temperature resistance from the 1st cycle to the 2nd cycle [99].

The behavior observed for the physical and electrical properties of the conductors upon static annealing is further verified via temperature-dependent electrical measurements performed under vacuum, whereby the strong interaction between the Ti

and the CNTs results in a reduction in room temperature resistance from the first cycle to the second cycle. The performance observed for the hybrids fabricated here can be explained by the interaction expected between the various metals and the CNTs. Previous studies have suggested that metals with a higher amount of vacancies in the d-orbital react more readily with carbon [66], and thus exhibit better wettability on CNTs [79]. Since Cu has a full d-orbital, it exhibits the worst interaction with carbon. Ni exhibits improved characteristics over that of Cu, due to having two d-orbital vacancies, however, still exhibits weaker interaction with CNTs than Ti, forming quasicontinuous coatings (when < 5 nm thick) as-deposited onto individual CNTs [63]. Ti exhibits the strongest reactivity (of the three metals investigated here) with carbon owing to its eight d-orbital vacancies [66]. Moreover, computational studies have calculated that Ti has a high binding energy with CNTs of various chiralities [90, 109], which supports the formation of continuous Ti chains on the surface [90], corroborating experimental findings of the tendency of Ti to wet individual CNTs [63, 64]. It has been suggested that the high binding energy calculated between Ti and CNTs may stem from hybridization of the 3d orbitals of the Ti with the 2p orbitals of carbon, as the 3d orbitals in Ti tend to behave as valence orbitals facilitating bonding [90, 110, 111]. The weakness/strength of these interactions are also evidenced here by the textured nanostructure morphology of as-deposited Ni (Figure 6a), and the uniform coating of the as-deposited Ti (Figure 7a), respectively. While fast surface diffusion accompanied by low nucleation rate are responsible for the formation of surface roughness upon deposition, a conformal coating corresponds to a strong binding energy and condensation coefficient between the metals and the CNTs [64].

The electrical properties of the conductors also reveal insight toward the metal-CNT interaction. While Ni exhibits weaker interaction with carbon than Ti, it is capable of providing some benefit to the electrical properties in a Cu-Ni-CNT conductor over that of Cu-CNT alone when exposed to temperatures up to 300 °C in a reducing environment. At temperatures of 400 °C, however, degradation is observed in the electrical benefits of the Cu-Ni-CNT conductor, as the resistance sharply increases beyond that of the Cu-CNT. The sharp rise in resistance may be attributed to the fact that the Ni layer on its own minimizes its area on the surface of the CNTs at this temperature, thereby exposing bare CNT surface prior to the Cu deposition as observed in Figure 6. Furthermore, the Ni may be negatively impacting the CNT structure due to the high carbon solubility [45]. Additionally, the Cu and Ni are likely forming a low concentration Ni/Cu alloy which is also contributing to an increase in R/L beyond that expected for Cu-CNT alone. It is known that metallurgically processed [112] and electrodeposited [88] Ni-Cu alloys experience an increase in resistivity over that of pure Cu as the Ni content is increased. Moreover, nano-phase Ni-Cu is expected to have a depression in the liquidus and solidus curves compared to its bulk form [113]. The high surface energy between the CNTs and the Ni (as indicated by the formation of discrete Ni particles in Figure 6e) may further reduce the temperatures required to form an alloy. The electrical data presented here suggests that an alloy may be forming at temperatures as low as 400 °C, which is detrimental for operation or processing of such metal-CNT hybrids at elevated temperatures when using Ni as an adhesion metal. In contrast, enhanced interaction between Ti and the CNT conductor enables the Cu grain structure to expand while maintaining adhesion. In addition, the material compatibility between Ti and Cu sustains

the electrical benefits induced by the annealing to temperatures up to 400 °C. As a result, the Cu-Ti-CNT conductor outperforms the Cu-CNT and Cu-Ni-CNT conductors upon exposure to 400 °C, and, therefore, Ti emerges as an effective adhesion metal for metal-CNT conductors.

In conclusion, interfacing CNTs and Cu with a Ni or Ti layer proves to mitigate Cu-CNT connectivity problems, providing stability to the Cu overcoat upon exposure to elevated temperatures. Without the use of an adhesion metal, Cu deposited onto the CNT conductor coalesces at elevated temperature, which is relevant for motor applications, and is accompanied by an irreversible increase in resistance. Ni showed poor adhesion to the CNTs at elevated temperatures, however, the use of Ni in a Cu-Ni-CNT system suppressed the delamination of the Cu layer. The electrical properties, however, were still unfavorable at temperatures reaching 400 °C, ultimately increasing resistance by up to 125%. In the case of Ti, on the other hand, uniformity of the coating was preserved upon heat treatment, and with the addition of a Cu overcoat, delamination was mitigated. In addition, the conductive properties of the Cu overcoat in the Cu-Ti-CNT conductor improved upon annealing, with room temperature resistances decreasing by up to 12%. Furthermore, temperature-dependent electrical measurements performed under vacuum demonstrate similar trends as seen in the static anneals in a reducing atmosphere. As a result, Ti has been identified as an effective interfacing metal for metal-CNT conductors, which when exposed to elevated temperatures (either through operation or processing), can provide superior electrical and adhesion benefits, enabling a path forward for conductor designs.

4 Fabrication of Composites Through CVD & Electrodeposition

Objectives

- Identify a viable Ti precursor for CVD delivery.
- Assess Interaction of Ti Deposited via CVD.
- Electroplate to form Cu-Ti-CNT hybrids.
- Optimize metal depositions for high conductivity and favorable TCR.

Ti is known to exhibit excellent interfacial interaction with CNTs and enhances the electrical performance for Cu-CNT hybrids. A simple route for depositing Ti to form integrated Ti-CNT bulk conductors is warranted to increase the total metal:CNT interfacial contact area. Delivery of Ti rich films is difficult due to the high reactivity of Ti. Physical vapor deposition techniques offer a facile route toward deposition of pure Ti; however, these techniques deposit material primarily in the line-of-sight, resulting in surface coatings. Chemical vapor deposition, on the other hand, is known for its capability in providing more uniform coverage across irregular topographies [52], and is suitable for penetrating porous networks [27]. Leggiero et al. have demonstrated the successful deposition of metals on CNTs using a Joule-heating CVD technique, whereby a CNT substrate is resistively heated to provide thermal energy sufficient for decomposition of organometallic precursors [27]. Among the commercially available CVD precursors, cyclopentadienyl(cycloheptatrienyl) titanium (II) [CHT-Ti-Cp] has been demonstrated to have the potential to form Ti rich films (24). A potential fragmentation pathway of the C_7H_7 and C_5H_5 rings can occur, in which a disproportionation results in

two stable benzene rings being eliminated in turn from the parent ion (24,25). The research herein reports the utilization of the Joule-heating CVD technique to fabricate integrated Ti-CNT conductors, whereby the Ti is assessed as an adhesion metal for bulk Cu-CNT conductors. Delivery of Ti via CVD enables the penetration of Ti into the CNT network, maximizing the metal:CNT interfacial contact area in the bulk conductor. The following work in this section has been reprinted with permission from (McIntyre, D. J., et al, Integrated Titanium-Carbon Nanotube Conductors via Joule-Heating Driven Chemical Vapor Deposition, *ECS Transactions* 97.7 (2020): 321-327). Copyright (2020) ECS https://doi.org/ 10.1149/09707.0321ecst.

4.1 Fabrication of Ti-CNT Conductors Using Joule-heating Driven CVD

4.1.1 CVD experimental setup

Fabrication and processing

The CNT conductor used in this study is Miralon® roving (lot 954738) obtained from Nanocomp Technologies Inc. (a Huntsman International LLC. company). This free-standing unspun CNT conductor takes a ribbon geometry (~30 μm × 1.53 mm), and the full physical characteristics have been reported previously [27, 99]. A one-hour vacuum dry at 100 °C is performed on the CNT conductor prior to analysis and processing.

Joule-heating driven chemical vapor deposition (CVD) was performed in accordance to a previous study [27]. Flat Cu clips crimped to Cu electrical leads are passed through rubber septa at two opposing necks in a three-neck flask. Three 12 cm long CNT conductors are suspended in parallel by the Cu clips, sharing a common electrical contact point at each clip. Precursor masses of 1 mg, 5 mg, and 25 mg cyclopentadienyl(cycloheptatrienyl) Titanium(II) (CAS# 51203-49-7, Strem Chemicals

99%), were loaded into the bottom of the flask within a glovebox, in an inert Ar atmosphere. A heating mantle temperature of 200 °C was used to sublimate the precursor. The center neck of the flask was connected to a Schlenk line via a hose-barb adapter with a stopcock, which allowed for pulling vacuum or supplying 5% H_2 / 95% Ar (mol/mol) gas. A constant current of 350 mA per CNT conductor is continuously applied for one hour while the precursor is subliming, to provide sufficiently high temperatures required for decomposing the metal-organic precursor upon contact with the CNTs. A target vacuum pressure of 0.3 Torr was regulated by opening the stopcock as needed. The Ti-CNT conductors were then subjected to a 95% Ar / 5 % H_2 anneal in a tube furnace at a temperature of 300 °C for one hour.

Electroplating in a sandwich cell configuration was performed as reported previously [27] on the 5 mg CHT-Ti-Cp seeded CNT conductor. A constant-current condition of 7.4 A/g_{CNT} was applied for 354 minutes to achieve a target total metal mass of 98% wt/wt. Due to irregularities in surface area, plating rate is calculated based on mass of the CNT conductor. To determine the amount of mass/length needed to be added in the form of Cu to obtain 98% total metal mass, the following equation is used:

$$\left(\frac{M}{L}\right)_{Added\_Cu} = \frac{\left(\frac{M}{L}\right)_{As-received\_CNTs}}{0.02} - \left(\frac{M}{L}\right)_{Ti-CNT\_Composite} \quad (7)$$

The chosen plating rate then determines how much time is necessary to achieve the target amount of added Cu mass. After electroplating, the Cu-Ti-CNT conductor was then densified to a target 30 µm using a rolling mill, and subsequently subjected to a 95% Ar / 5 % H_2 anneal in a tube furnace at a temperature of 300 °C for three hours.

Characterization

Analysis of deposition morphologies was performed using a Hitachi S-4000 scanning electron microscope (SEM) equipped with a secondary electron detector and 10 kV accelerating voltage. Cross-sections for the Cu-Ti-CNT samples were prepared via razorblade sectioning of the conductors. Energy dispersive X-ray measurements were performed on the 25 mg CHT-Ti-Cp deposited sample using a Tescan Mira3 SEM equipped with a Bruker XFlash 6|30 EDS at a 20 kV accelerating voltage. Cross-sections for EDS mapping were epoxy-set and ultramicrotomed. The room temperature electrical properties of the conductors were measured in an ambient atmosphere by applying current-voltage sweeps (up to 100 mA) using a four-point-probe configuration with a National Instruments NI PXI-5652 source/measure unit and NI PXI-4071 digital multimeter. Temperature-dependent electrical measurements were performed by sweeping the temperature from 300 to 600 K under 10^{-6} mbar vacuum in a Janis cryostat. Four-point probe I-V sweeps were carried out at 5 K increments for two cycles of temperature sweeps. Measurements were acquired using a National Instruments NI PXI-4110 programmable power supply and NI PXI-4072 digital multimeter. The temperature coefficient of resistance (TCR) was calculated based on the average slope of resistance with respect to temperature, whereby the resistance is normalized to the starting resistance at 300 K. TCR calculations are based on the second cycle data. Mass measurements were made using a Mettler Toledo XP-2U microbalance.

4.1.2 CVD deposited Ti properties

CHT-Ti-Cp

The surface-view SEM image acquired in Figure 13a shows the network morphology of the starting CNT conductor. A loose network morphology is observed

with the presence of nanoscale pores. Joule-heating driven CVD was performed using 25 mg of CHT-Ti-Cp precursor, leading to an average deposition mass loading of 67.2 ± 2.5% wt/wt. The standard deviation reported here is based on three samples fabricated together at the same conditions. As shown in Figure 13b, a fully connected film forms at the surface of the Ti-CNT conductor at this mass loading. An ultramicrotomed epoxy-set cross-section of the Ti-CNT conductor is shown in Figure 13c, with the corresponding EDS Ti signal overlay shown in Figure 13d. A higher concentration of Ti localizes at the surface and is likely resultant of deposited Ti blocking the pores at the surface, preventing further penetration as the CVD process evolves. However, Ti is observed to be present throughout the entire cross-section of the conductor, indicating successful penetration of the precursor during the initial stages of the CVD process. Additionally, a strong Ti peak is observed in the surface-view EDS data (Figure 13e), demonstrating the successful deposition of Ti. The presence of O is also observed, which may result from residual adsorbed oxygen within the CNT network, or the formation of surface oxides after exposure to atmosphere. The oxygen content may be reduced by performing a heat-treatment to the CNT network, which is known to desorb oxygen and other ambient dopants [105]. Furthermore, surface oxidation may be minimized by performing a subsequent CVD deposition using Cu to passivate the Ti surface and improve the Cu-Ti interface. Nevertheless, the Joule-heating driven CVD technique utilized here has shown to successfully deposit Ti, and achieve penetration throughout the entirety of the bulk CNT network.

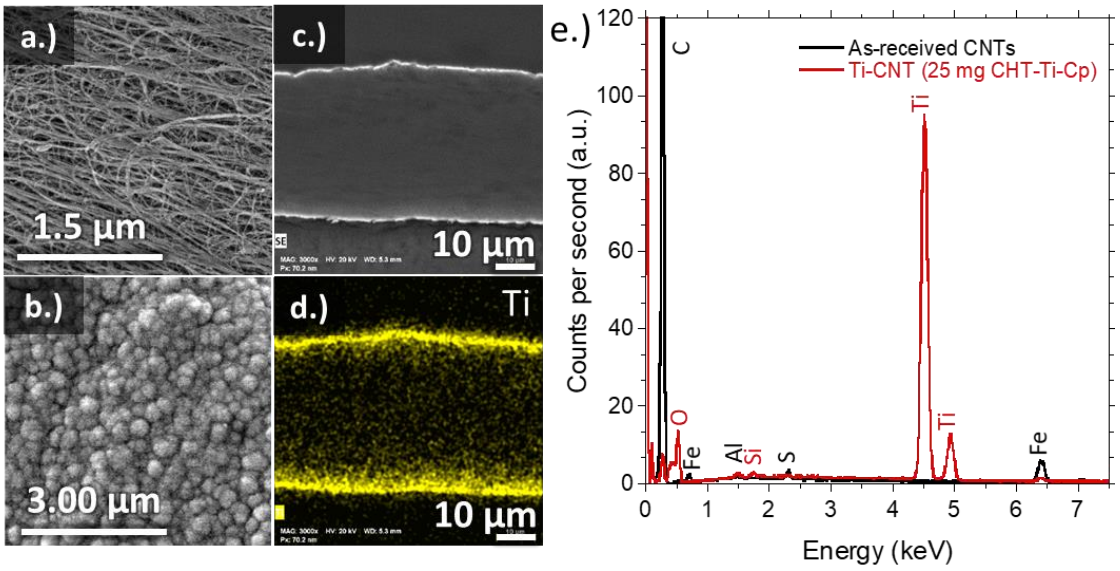

Figure 13 Surface SEM images of (a) as-received CNT conductor and (b) Ti-CNT conductor fabricated via Joule-heating driven CVD using 25 mg of CHT-Ti-Cp precursor. Cross-sectional SEM image of (c) the same Ti-CNT conductor with (d) an EDS overlay of the Ti component. (e) Signal intensity of the observed elemental peaks obtained via EDS from the surfaces of the as-received CNT conductor and a 25 mg deposition of CHT-Ti-Cp [114].

Joule-heating driven CVD was additionally performed using 1 mg, and 5 mg of CHT-Ti-Cp precursor, leading to 10.6 ± 5.1%, and 31.3 ± 1.8% deposition mass respectively. Figure 14a-c shows the surface morphology of the as-deposited Ti coatings. It is observed that 1 mg of precursor is sufficient to coat the CNT bundles while maintaining the network morphology. Increasing the precursor amount to 5 mg and beyond results in full surface coverage of the CNTs, forming a continuous Ti film which blocks the nanopores and prevents further network penetration. Figure 14d-f shows the surface morphology of the corresponding depositions after annealing to 300 °C in 95% Ar / 5% H_2 for 1 hour. Upon exposure to 300 °C, some grain restructuring can be observed. However, the deposited Ti indeed maintains a continuous coating for all depositions, resulting from the strong interaction between Ti and CNTs. The stability of Ti on CNTs observed here is in agreement with that reported for thermally evaporated Ti on CNTs. The CVD technique used here, however, has the advantage of network

penetration and has demonstrated the ability to tune the morphology of coatings to localize along the CNTs or form a thin film.

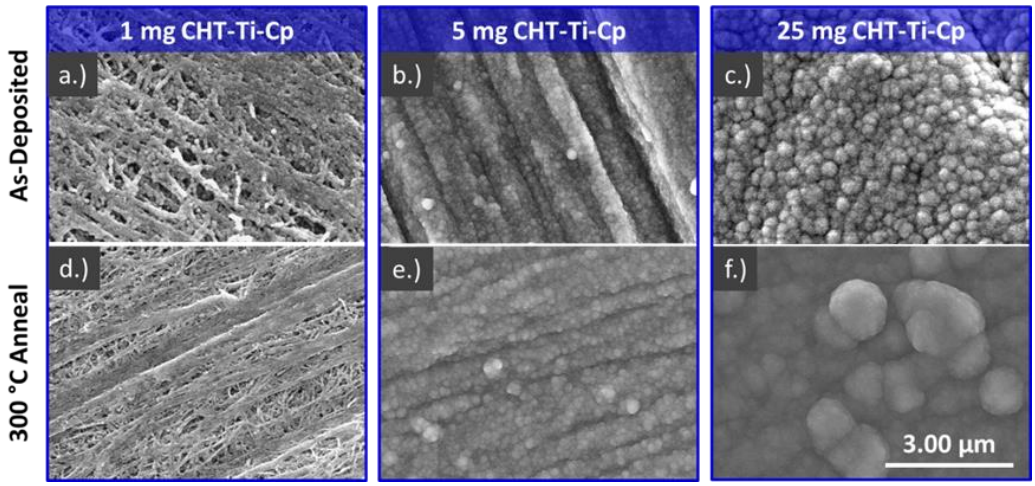

Figure 14 SEM images of CVD deposited CNT roving with a.) 1 mg, b.) 5 mg, and c.) 25 mg of CHT-Ti-Cp precursor as-deposited. (d-f) SEM images of the corresponding conductors annealed at 300 °C for 1 hour under 95% Ar / 5% H2 environment, showcasing sustained continuity [114].

4.2 Electroplating to form Cu-Ti-CNT hybrids

4.2.1 Hybrid conductor performance

Electroplating of Cu was performed on the 5 mg CHT-Ti-Cp deposited CNT conductor to fabricate a Cu-Ti-CNT hybrid comprising 97.1%/0.9%/2% wt/wt of each respective component. Based on cross-sectional SEM images (see Figure 15a) and room temperature electrical measurements, the conductivity of the Cu-Ti-CNT conductor was determined to be 32.3 MS/m. Insight toward the interaction between the metals and the CNTs can be gained by analyzing how the conductor performs at increasing temperatures. Two cycles of temperature-dependent electrical measurements were taken from 300 to 600 K. The resistance was normalized to a starting resistance at 300 K and plotted to show the relative change in resistance for the second cycle, shown in Figure

15b. A temperature coefficient of resistance (TCR) for the Cu-Ti-CNT conductor of 3.18 × 10^{-3} K^{-1} was calculated based on the average slope of the relative resistance with respect to temperature. The Cu-Ti-CNT hybrid presented here exhibits a higher conductivity and a lower TCR than that reported for a similar Cu-CNT conductor fabricated without a Ti adhesion layer [27], demonstrating the direct benefits that interfacing the CNTs and Cu with Ti has.

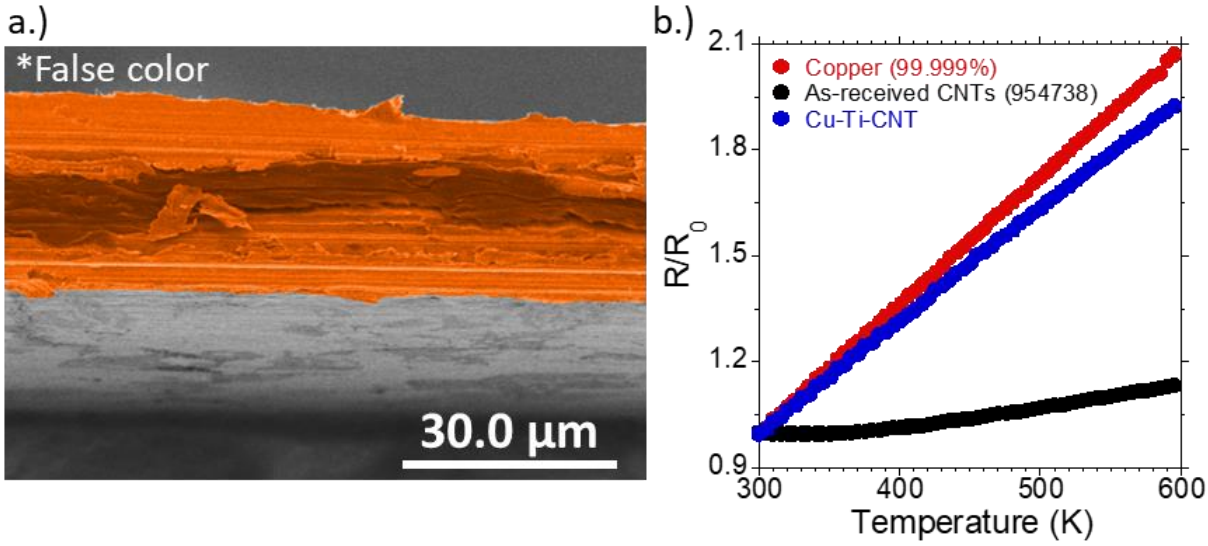

Figure 15 Cross-sectional SEM of a.) the 5 mg CHT-Ti-Cp deposited CNT roving, electroplated with copper to 98% total metal mass and b.) temperature dependent electrical measurements of the Cu-Ti-CNT hybrid, as-received CNT conductor, and 99.999% pure copper [114].

Utilization of the Joule-heating driven CVD technique with a CHT-Ti-Cp precursor enables the fabrication of integrated Ti-CNT conductors. CVD depositions carried out using 1 mg of precursor lead to Ti coatings which localized along the CNT bundles, preserving the nanopore integrity for further metal infiltration. On the other hand, depositions using 5 mg or more of precursor lead to fully continuous thin film formation. Thus, varying the amount of precursor used for the CVD process offers control over the resulting deposition morphology. In all cases, the Ti films remained adhered to the underlying CNTs upon exposure to temperature of 300 °C for 1 hour in

95% Ar/ 5% H_2, demonstrating the strong interaction between the Ti and CNTs. Cu-Ti-CNT hybrids constructed via electrodeposition of Cu resulted in a high conductivity of 32.3 MS/m and a corresponding TCR of $3.18 \times 10^{-3}\ K^{-1}$. Thus, the CVD technique shows promise as a delivery route for fabricating integrated Ti-CNT conductors for use in high-performance metal-CNT hybrids.

4.3 CVD and Electroplating Controls

Further optimization has been carried out by performing studies investigating the impact that metal mass loading has on the room temperature electrical and temperature dependent electrical performance of the Cu electroplated hybrids.

4.3.1 CVD & Electrodeposition Weight Loading Impact

95% Total Metal Mass / 5 mA Electroplating Current

CVD of CHT-Ti-Cp was performed onto the CNTs as described in 4.1.2 and electroplated in a sandwich cell configuration with 5 mA cathodic current to a total metal mass loading of 95% w/w (see Figure 16). Upon planar densification and annealing, the Cu-Ti-CNT conductors seeded with 5 mg and 25 mg CHT-Ti-Cp exhibited a conductivity of 1.1 MS/m and 4.9 MS/m, respectively, with TCR_{300K} values of 1.5 and $2.5 \times 10^{-3}\ K^{-1}$. Conductivities were calculated using cross-sectional SEM images to determine the area, and temperature dependent electrical measurements were performed in the Janis cryostat as described earlier [114]. Electroplated coatings at 95% total metal mass loading led to spotty coatings that weren't well connected at the surface. The lack of sufficient electrical connection is attributed to the low conductivities obtained at the 95% metal mass loading. Thus, evaluation of higher electroplated weight loadings are investigated to promote additional circuitous pathways and enhance the performance of the hybrid conductor.

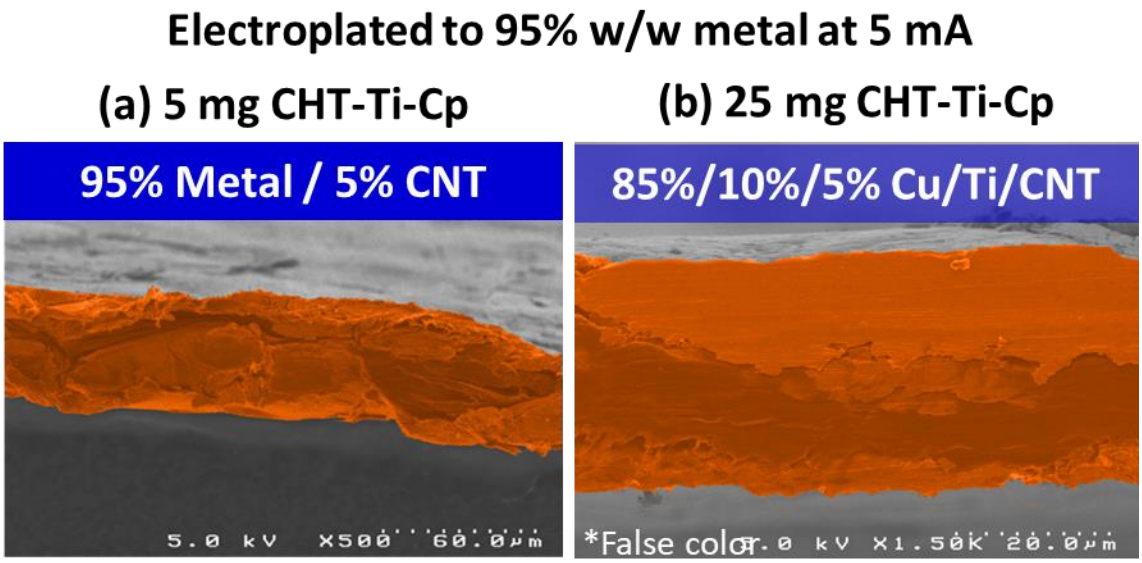

Figure 16 Cross-sectional SEM images of (a) 5 mg, and (b) 25 mg CHT-Ti-Cp deposited CNT roving, electroplated with Cu to a total metal mass of 95%, using 5 mA current, and further processed by densification, and annealing in 5% Ar / 95% H_2 for 3 hours at 300 °C.

98% Total Metal Mass / 5 mA Electroplating Current

CVD of CHT-Ti-Cp was performed onto the CNTs as described in 4.1.2. Additionally, a Ti-CNT conductor was fabricated using 0.625 mg of CHT-Ti-Cp precursor to assess the impact on electrodeposition behavior. As shown in Figure 17, the deposited Ti with 0.625 mg precursor maintains the network morphology and had greater retention to the pore structure than achieved at higher weight loadings. Samples were electroplated in a sandwich cell configuration with 5 mA cathodic current to a total metal mass loading of 98% w/w (see Figure 18). Electroplating the 0.625 mg CHT-Ti-Cp seeded conductor (97.9% Cu / 0.1% Ti / 2.0% CNT) led to a surface coating consisting of gaps and discontinuous regions, resulting in a specific conductivity of 2263 Sm^2/k.

Previously, densification has been shown to increase the resistance of the conductors; however, there exists a trade-off between cross-sectional area and resistance

per length when targeting high conductivity. To assess the conductivity trade-off from densification, the 0.625 mg CHT-Ti-Cp seeded conductor was first annealed directly after electroplating at 300 °C for 3 hours in 5% H_2 / 95% Ar, resulting in a conductivity of 14.9 MS/m. Afterwards, the sample was densified and annealed again, resulting in a final conductivity of 16.4 MS/m, indicating that the rise in resistance resulting from densification doesn't outweigh the benefit of the reduced cross-sectional area.

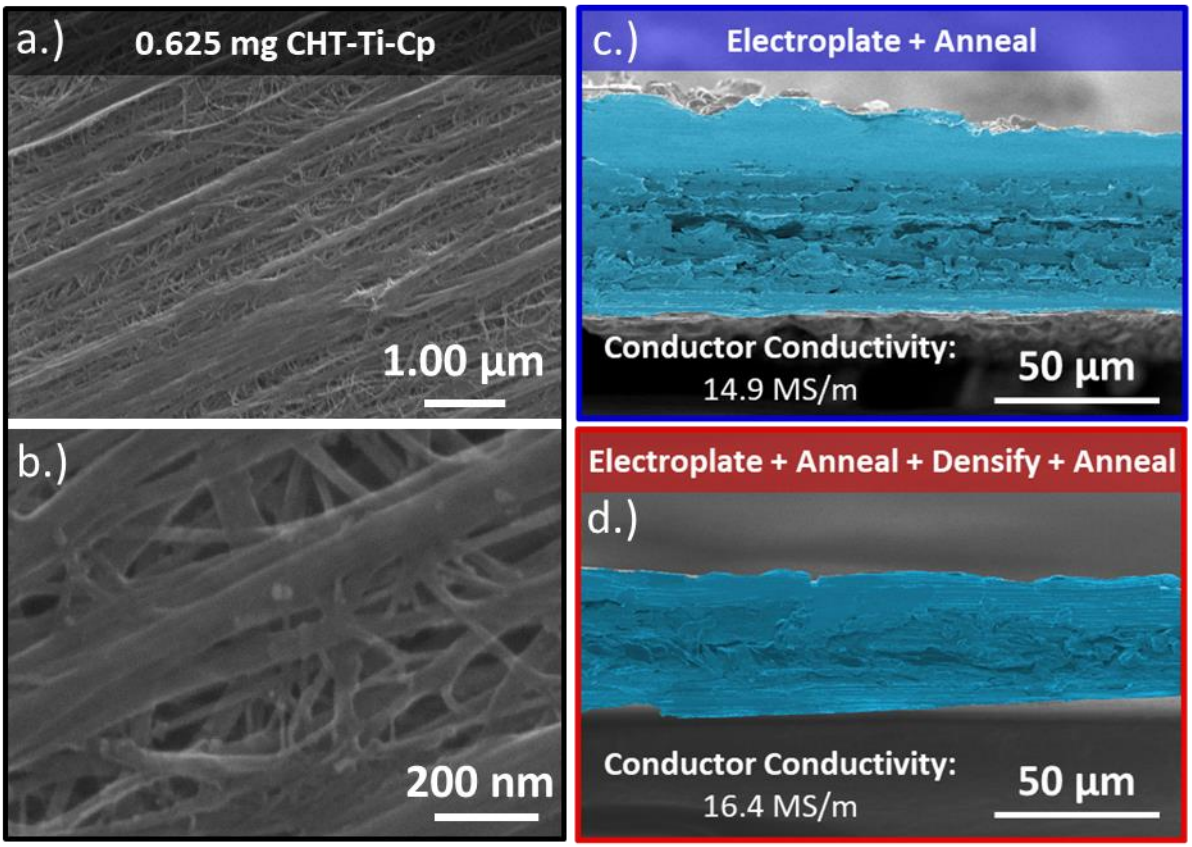

Figure 17 Surface SEM images of a,b.) 0.625 mg CHT-Ti-Cp seeded CNT conductors. Cross-sectional SEM images of the seeded conductors after c.) electroplating (5 mA current) and annealing, as well as after d.) electroplating (5 mA current), annealing, densification, and a final anneal in 5% Ar / 95% H_2 for 3 hours at 300 °C.

Electroplating the 1 mg CHT-Ti-Cp seeded conductor (97.6% Cu / 0.2% Ti / 2.2% CNT) led to a specific conductivity of 6604 $S \cdot m^2/kg$, which reduced to 6044 $S \cdot m^2/kg$ after

densification, and recovered to 6257 $S \cdot m^2/kg$ upon annealing. The improved performance in the 1 mg seeded sample is attributed to a combination of the retention of pore access after CVD allowing for additional Cu filling, as well as improved surface activity for electrodeposition resulting in a uniform surface coating of Cu. The fully connected Cu film at the surface is expected to increase the number of circuitous pathways, improving the overall electrical performance. The conductivity of the finished 1 mg seeded conductor reached 43.1 MS/m, based on cross-sectional SEM (see Figure 18) and electrical measurements, representing the highest conductivity and specific conductivity ever reported for a bulk CNT conductor at 98% weight loading or lower.

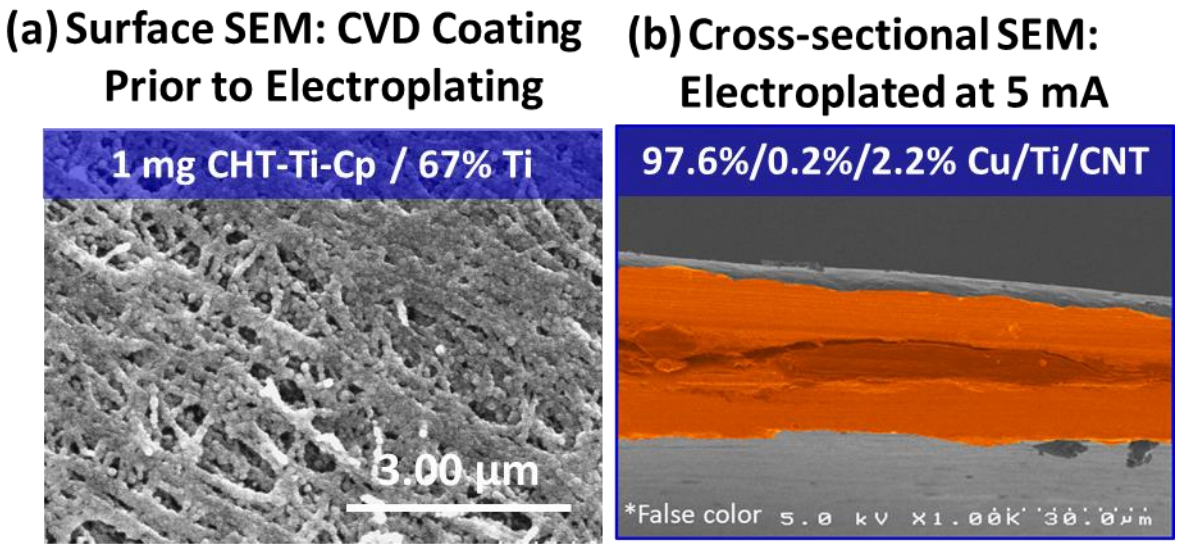

Figure 18 Cross-sectional SEM images a (a) 1 mg CHT-Ti-Cp deposited CNT roving, (b) electroplated with Cu to a total metal mass of 98%, using 5 mA current, and further processed by densification, and annealing in 5% Ar / 95% H_2 for 3 hours at 300 °C.

4.3.2 Electrodeposition Rate

98% Total Metal Mass / 10 mA Electroplating Current

Electroplating of the 0.625 mg CHT-Ti-Cp seeded CNT conductors (97.8 % Cu / 0.3% Ti / 1.9% CNTs) was performed with a current of 10 mA (as opposed to the 5 mA

used previously), to encourage better connectivity of the Cu at the surface, which was observed to have a positive impact in previous depositions. After electroplating the 0.625 mg seeded sample with a 10 mA electroplating rate, a uniform, well connected Cu film was achieved at the surface. A specific conductivity of 5179 $S \cdot m^2/kg$ was achieved with the 10 mA electroplating current, compared to the 2263 Sm^2/kg achieved on the 0.625 mg seeded conductor with 5 mA electroplating current. Annealing the conductor brought the specific conductivity to 5962 $S \cdot m^2/kg$, while densification reduced the conductivity to 5869 $S \cdot m^2/kg$. A final anneal brought the specific conductivity to 5976 $S \cdot m^2/kg$. A conductivity of 34.1 MS/m was achieved based on the cross-sectional measurements (Figure 19). The high specific conductivity and conductivity observed for this sample is attributed to the continuity in the surface coating provided by the higher electroplating rate, and thus the surface coverage of the Cu is attributed to being an important factor in the final electrical performance for the Cu-Ti-CNT conductors.

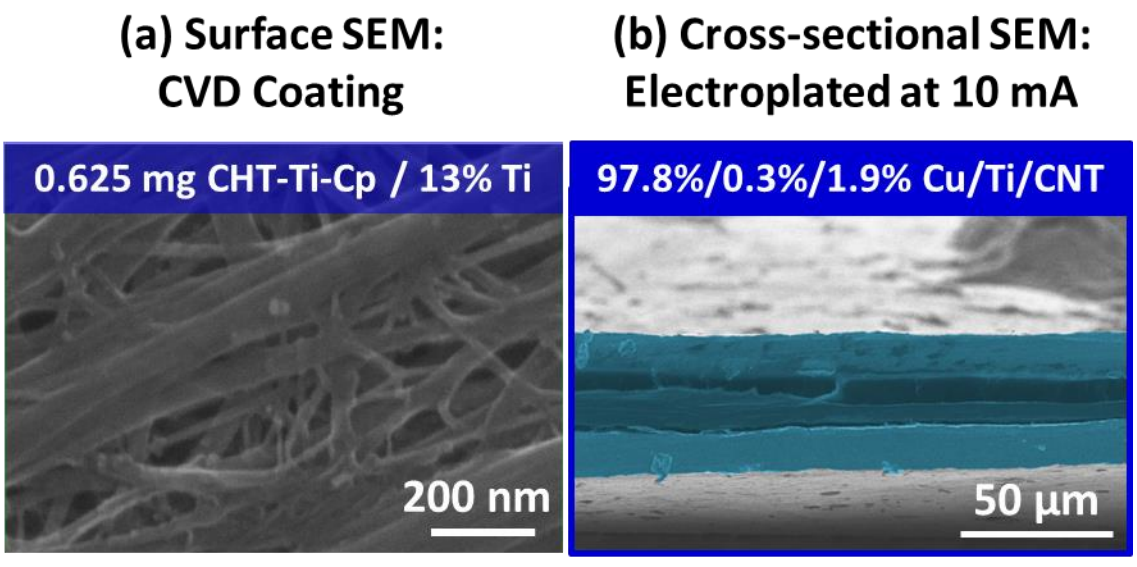

Figure 19 Cross-sectional SEM images of (a) 0.625 mg CHT-Ti-Cp deposited CNT roving, (b) electroplated with Cu to a total metal mass of 98%, using 10 mA current, and further processed by annealing, densification, and a final anneal in 5% Ar / 95% H_2 for 3 hours at 300 °C.

4.3.3 Temperature Dependent Electrical Behavior

Temperature dependent electrical measurements of the electroplated and fully processed CHT-Ti-Cp seeded conductors have been conducted under vacuum (10^{-6} mbar) in the temperature range of 300 – 600 K (see Figure 20a). Samples electroplated (5 mA current) to a total metal mass loading of 95% exhibited the lowest TCR_{300K} values for any of the Cu-Ti-CNT conductors evaluated, at 1.5 and 2.5×10^{-3} K^{-1} for 1 mg and 5 mg CHT-Ti-Cp seeded conductors respectively. As the weight loading is increased to 98% metal w/w (at 5 mA current), the TCR values correspondingly increase, attributed to the better connected surface Cu playing a more prominent role in the electrical transport. TCR_{300K} values of 3.12, 3.49 and 3.18×10^{-3} K^{-1} were obtained for 0.625, 1, and 5 mg CHT-Ti-Cp seeded conductors, respectively. Lastly, a TCR_{300K} value of 3.53×10^{-3} K^{-1} was obtained for the 0.625 mg CHT-Ti-Cp seeded conductor that was electroplated to 98% total metal mass at 10 mA electroplating current. Due to the extensive processing and measurement time required for each sample, repeats for exact conditions have not been performed. The results are thus assessed based on the general trends observed. It is generally observed here that higher total mass loading as well as higher electroplating rates both lead to more conductive coatings at the expense of a higher TCR, which is consistent with studies that have found TCR to be dependent on the amount of filling and intermixing with the underlying CNTs. Moreover, samples that had a better connected Cu film at the surface tended to exhibit higher specific conductivities as well as higher TCR values as a result of the increased participation of the Cu.

In all cases, the TCR is lower for the Cu-Ti-CNT hybrids, and thus a metric is needed to assess whether the combination of TCR and conductivity indicates a lack of

interaction or favorable interaction. To evaluate the performance for conductivity or specific conductivity, a simple rule of mixtures comparison is sufficient to indicate whether the electrical performance exceeds that of two non-interacting conductors (i.e. Cu and CNTs). For assessing the TCR, a model has been developed to calculate an expected TCR for a non-interacting, parallel resistor combination of CNTs and Cu at any Cu mass fraction from 0 to 100% [27], as shown in the curve in Figure 20b. The Cu-Ti-CNT hybrids fabricated here have been plotted against the curve. Conductors with higher specific conductivity and lower TCR than the curve represent cases where favorable interaction leads to enhanced electrical properties. It is observed that the samples fabricated at 95% total mass loading don't interact well, and instead perform worse than two independent resistors. Potentially the deposition in these cases led to increased scattering and were not connected well enough to provide enhancements to the electrical transport. However, samples with higher mass loading (98%) as well as faster electroplating rates are observed to exceed the rule of mixtures performance, indicating enhanced electrical interconnection. In fact, the 1 mg CHT-Ti-Cp seeded conductor has a specific conductivity of 6257 Sm^2/kg, combined with a TCR_{300K} of 3.49×10^{-3} K^{-1}, and thus outperforms pure Cu in terms of specific conductivity at any temperature above 250 °C, demonstrating direct energy savings for elevated temperature applications.

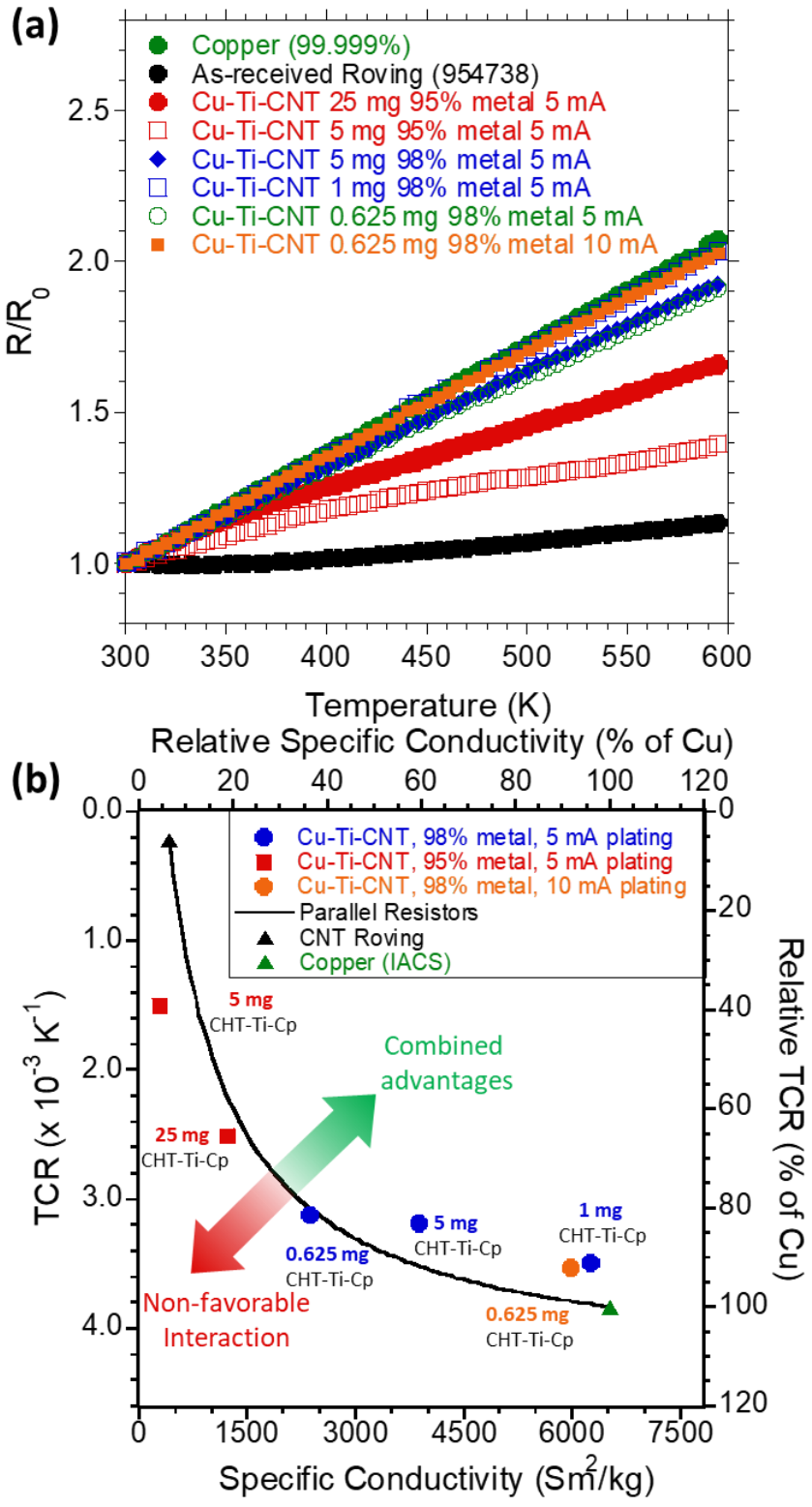

Figure 20 (a) Temperature-dependent resistance measurements for the various Cu-Ti-CNT hybrids, as well as (b) a comparison the TCR versus specific conductivity for the various CHT-Ti-Cp seeded conductors.

5 Surface Modification towards Enhanced Ti-CNT Interface

Objectives

- Purify NCTI roving to remove catalyst and improve interaction with CVD deposited metals.
- Develop control over oxide formation during CVD depositions
- Evaluate the influence of CVD on the electrical properties by modeling the temperature dependent electrical properties.

5.1 Contact Modification and Oxidation Prevention

5.1.1 Material Processing: Purification and Joule-heating Annealing

The non-localized electrons in CNTs leads to ambient susceptibility due to van der Waals attractions at the sidewalls, whereby molecules adsorb out-of-plane to the CNTs [71, 72, 74]. Specifically, moisture and oxygen from the ambient are known to adsorb well to CNTs [105]. The presence of adsorbed molecules alters the density of states for CNTs and can negatively impact the contact between metals and CNTs [69]. In fact, previous work demonstrated that current stressing provides enough Joule-heating to drive off adsorbed molecules [115, 116], and was separately shown to drastically improve the contact resistance between CNTs and metals [69]. Thus, the presence of foreign molecules can strongly influence the overall electrical properties and must be considered for metal-CNT hybrid conductor design.

In the context of Ti deposition onto CNTs, oxygen removal is especially important, as Ti is highly reactive and forms non-conductive oxides. In addition to adsorbed oxygen at the CNT walls, metal catalysts used during the synthesis of CNTs can also remain trapped within the network and may be susceptible to oxide formation. Such oxides (e.g. Fe_2O_3) may undergo a redox reaction with the highly reactive Ti, or

otherwise alter the contacting properties. Thus, in the pursuit of a Ti-rich film, multiple sources of oxygen must be considered and managed. As seen in Figure 13e, a non-negligible oxygen EDS signal is present upon CVD deposition of Ti onto the CNTs. Since the CHT-Ti-Cp precursor doesn't inherently contain oxygen, the only source of oxygen is that within the CNT network, and that from exposure to atmosphere.

Pretreatment steps are employed here to reduce oxygen content and encourage the deposition of Ti-rich or TiC films. A CNT purification technique has been previously developed to remove carbonaceous impurities and catalysts [117]. This purification technique is adapted and optimized for the CNT materials used herein for the removal of the catalyst to provide a cleaner surface for contacting. The as-received Miralon is loaded into a tube furnace and ramped to 560 °C at 10 °C/min in air to burn carbonaceous material and oxidize the metal catalyst, and subsequently submerged in concentrated HCl for 30 minutes to dissolve the catalyst. A final burn to 560 °C is performed with identical conditions to the first burn to remove any residual acid. The efficiency of purification is assessed via thermogravimetric analysis (see Figure 21), from which the residual catalyst remaining within the CNTs after purification is shown to be < 1.4%. The amount of catalyst remaining determined by TGA is corroborated with EDX measurements, which shows <1 % Fe remaining, in close agreement with the TGA data (see Figure 22). It should also be noted that purification leads to a reduction in the overall mass of the conductors, reducing the mass/length to ~8 tex, and correspondingly increasing the R/L to ~350 Ω/m. As such, the thermal response to an electric bias is also altered and must be accounted for, for use in CVD experiments.

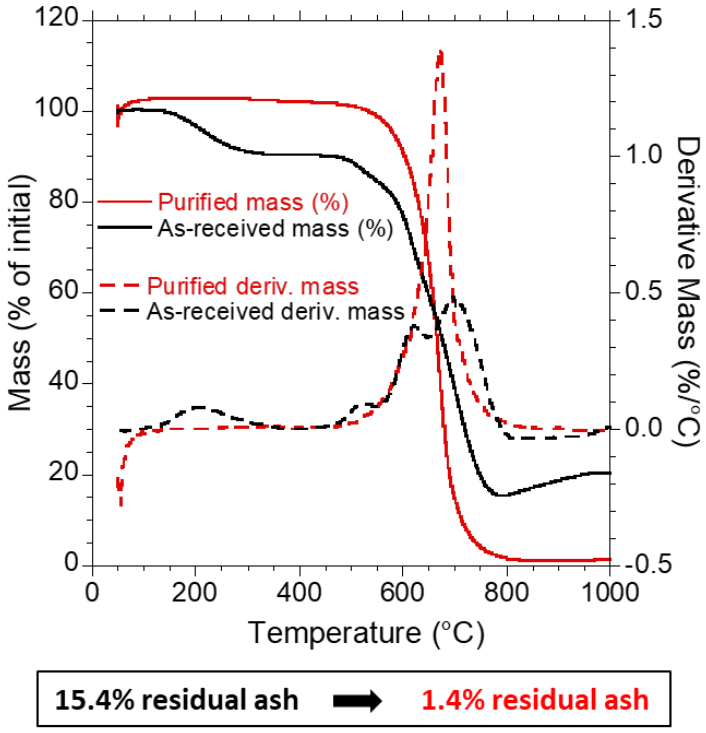

Figure 21 Thermogravimetric analysis of as-received and purified Miralon (Lot 955388) showing a reduction in residual catalyst ash from 15.4% down to 1.4%.

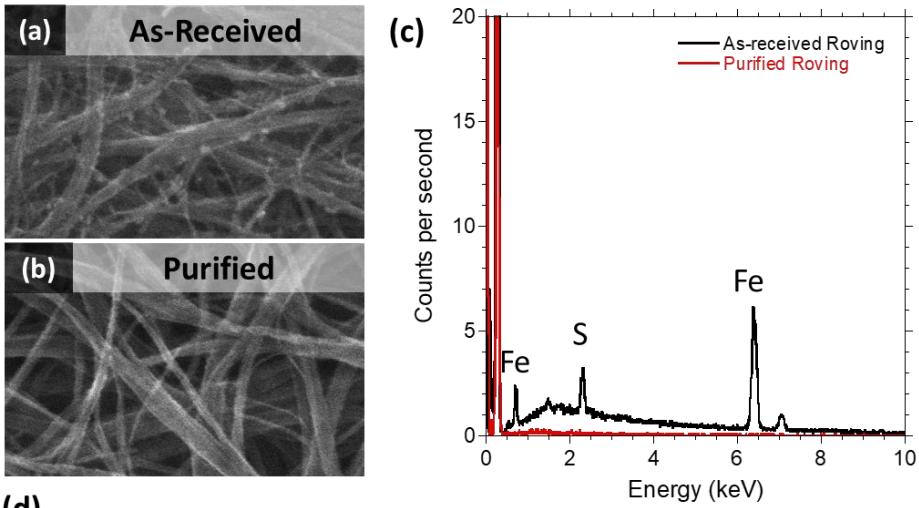

(d)

As-Received Miralon	C	Fe	S	O	Ti
	84.71	13.54	0.93	0.54	0.02
Purified Miralon	**C**	**Fe**	**S**	**O**	**Ti**
	98.74	0.89	0	0.29	0

Figure 22 Surface view secondary electron SEM images of (a) as-received and (b) purified Miralon roving, as well as (c) their corresponding EDX spectra and (d) elemental composition.

A range of currents in 50 mA intervals between 100 mA and 350 mA were applied to the purified Miralon roving and the resultant temperature profile was measured via an IR camera to establish a calibration for targeting specific temperatures during Joule-heating driven CVD experiments (see Figure 23). Average temperatures were calculated by first exporting the IR image data into an excel sheet, whereby every cell contains a temperature value corresponding to a pixel in the image. Therefore, the region of the image that corresponds to the sample can be defined by filtering pixels with a temperature value greater than a specified threshold temperature. As such, the image with the hottest temperature profile is selected for defining the sample region as it has the most contrast between the sample and the surrounding environment. This defined area is then applied to every image within the set for accurate calculations at low temperatures. When the region is defined, the average temperature of the sample is calculated by averaging every cell within the defined area. Given that the sample is suspended between copper clips for electrical biasing, it is expected that the regions nearest the contact points are cooler than in the center due to heat-sinking. Additionally, the edges of the ribbon-shaped conductor may have a different behavior than the bulk. A standard deviation is calculated to reflect the differences in temperature along the entire sample, as represented by the error bars in Figure 23.

To ensure comparability of results between CVD depositions performed on as-received versus purified Miralon roving, currents were selected to provide the same average temperature across the sample. An applied current of 350 mA was applied during the CVD runs shown earlier on as-received roving, and as such, 250 mA has been

selected for experiments involving purified Miralon, based on the temperature calibration in Figure 23.

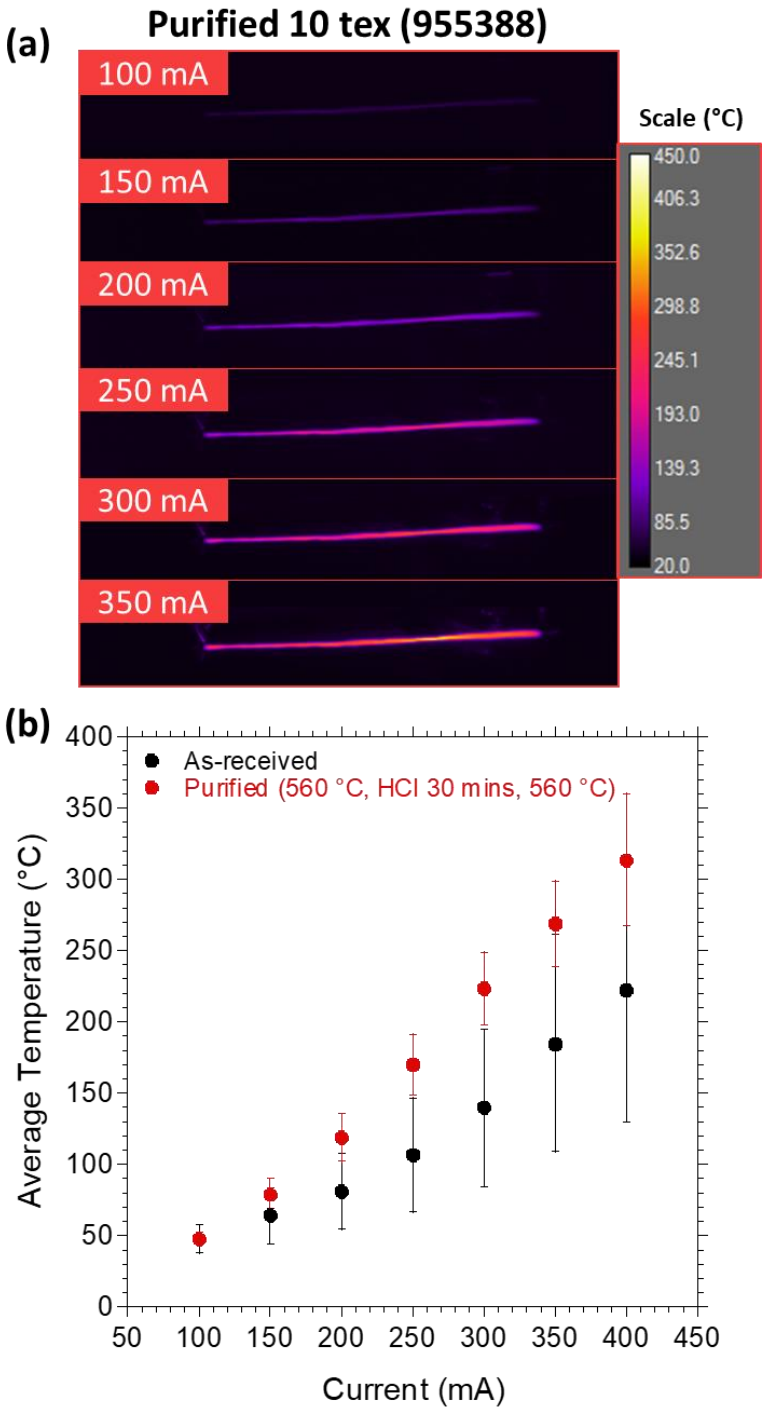

Figure 23 (a) IR images of the purified Miralon roving biased at currents ranging from 100 to 350 mA, as well as (b) the corresponding average temperature of the conductors at each applied current.

5.1.2 Vacuum CVD (< 0.250 Torr)

Using a purified CNT template helps to ensure that the impact of the CVD experiments can be attributed to the deposited metal, and to reduce any unexpected interactions with catalysts and/or species adsorbed at the surface of the CNTs. Thus, in the remaining sections, CVD conditions are developed for purified Miralon roving, and the resulting material properties are assessed via a mixture of electron microscopy, energy dispersive X-ray spectroscopy, mass and electrical measurements, and Raman spectroscopy.

In this study, an as-received Miralon CNT roving material is subjected to the purification procedure outline in section 5.1.1 to remove carbonaceous material, and catalyst metals trapped within the network. After purfication, there is a potential for oxygen to be adsorbed at the CNT sidewalls and/or bonded through functionalization. EDX spectroscopy indicates an elemental purity of ~99% carbon after purification; however, for extra caution, a reducing step is applied to clean the network. An in-situ hydrogen reduction is performed wherein the CNT network is Joule-heated in a 5% H_2/95% Ar atmosphere for 1 minute to reduce any potential functionalization, followed by 1 minute under vacuum, with sufficient current to reach temperatures > 300 °C (shown to drive off ambient dopants during temperature dependent resistance measurements shown in Figure 12). To monitor the impact of the treatment in-situ, applied current is increased in 50 mA steps for 1 minute intervals. In between each interval, the resistance of the sample is measured at 50 mA of applied current to ensure that the resistance isn't influenced by temperature during the measurement. The applied current for reducing the CNTs is increased in 50 mA steps until the room-temperature resistance is stabilized, indicating that the reaction is finished.

The Joule-heating pretreatment was performed on purified Miralon roving within the three-neck flask reaction chamber as described above, and then transferred to a glovebox with no exposure to atmosphere in between. The precursor was then massed inside of the glovebox within an argon atmosphere using a Mettler Toledo XP-2U to measure masses as low as < 1 mg. Cyclopentadienyl(cycloheptatrienyl) Titanium(II) (CAS# 51203-49-7, Strem Chemicals 99%) [CHT-Ti-Cp] was used as the precursor in this study. After massing the precursor, it was transferred into the three-neck flask within the glovebox and the flask was transferred into a hood while closed under argon. At this point, Joule-heating driven CVD was performed (as described in earlier works [27, 83, 114]) using CHT-Ti-Cp onto purified Miralon roving at a pressure of < 250 mTorr, a mantle temperature of 200 °C, and a continuously applied current of 250 mA for 1 hour.

The coating morphology of CVD deposited CNTs is assessed using a Hitachi S-4000 scanning electron microscope via secondary electron imaging, using a working distance of 8 mm and an accelerating voltage of 10 kV. Cross-sections were obtained via epoxy-setting and ultramicrotoming, and analyzed using a Tescan Mira3 SEM equipped with a Bruker XFlash 6|30 EDS at a 10 kV accelerating voltage. A Mettler Toledo XP-2U microbalance is used to acquire the mass before and after deposition in order to determine weight loading. Electrical properties were measured at room temperature in an ambient atmosphere by using a four-point-probe configuration with a National Instruments NI PXI-5652 source/measure unit and NI PXI-4071 digital multimeter and applying current-voltage sweeps up to 100 mA.

The results of one hour depositions using precursor masses of 0.7, 1.2, and 4.7 mg at 200 °C and < 0.250 Torr onto purified Miralon CNT roving biased at 250 mA are

presented in Figure 24. Mass measurements indicate that an increase in metal mass loading is obtained as the amount of precursor mass is increased, as expected, and is consistent with that observed for other precursors [27, 83]. Three samples were separately fabricated for the 4.7 mg condition to assess the reliability of targeting a specific weight loading using a specified precursor mass. The three samples resulted in a standard deviation for the weight loading of 4%, demonstrating the reliability of the method, and is within the range of standard deviations observed for depositions performed onto as-received Miralon CNTs with varied weight loadings (1.8-5.1%) [114]. All further depositions are performed on individual samples and the reliability is confirmed through the observation of consistent trends as established on prior sample sets. SEM imaging shows that a light coating is deposited using 0.7 mg of precursor, which is localized along the network morphology and preserves the mesoporous accessibility to an extent. As the precursor mass is increased to 1.2 mg, thickening of the coating around the bundles is observed and correspondingly, the void space between CNT bundles begins to fill in. At 4.7 mg, a fully connected film coats the CNT network, and the network morphology is no longer visible. As such, tunability of the coating morphology is demonstrated. Additionally, the Ti coating is observed to be uniform and continuous in all cases, with no observation of discrete crystallite formation, owing to its favorable interaction with CNTs.

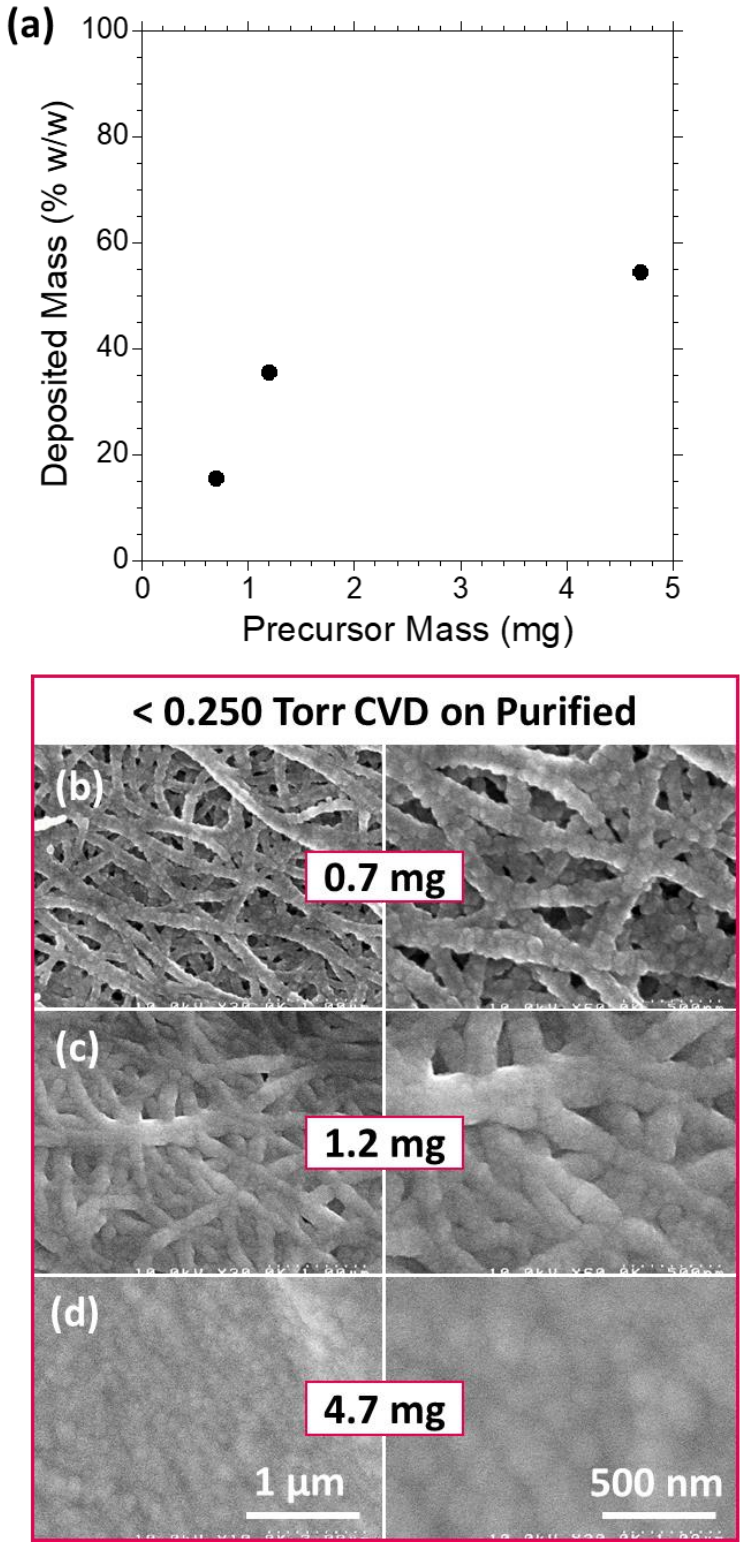

Figure 24 (a) Plot of the weight loading %w/w versus the starting precursor mass for CHT-Ti-Cp depositions performed at < 0.250 Torr, with a 200 °C mantle temperature, and 250 mA applied current for 1 hour. SEM images showing the morphology of the corresponding depositions with (b) 0.7 mg, (c) 1.2 mg, and (d) 4.7 mg CHT-Ti-Cp precursor.

Raman spectroscopy was performed to assess the characteristics of the hybrids after deposition. After CVD was conducted, samples were transported in glass vials held under an argon environment and sealed with Parafilm to prevent exposure to the atmosphere. Samples were subject to only minutes of exposure to atmospheric conditions while the Raman measurements were actively being taken. The measurements obtained via Raman spectroscopy show the standard graphitic peak at 1583 cm^{-1} associated with sp^2-bonded carbon, as well as a defect peak at 1331 cm^{-1} associated with sp^3-bonded carbon. Additionally, peaks are observed to be present that are identified for TiO_2 at locations of 218, 440, and 604 cm^{-1}, compared to those reported at 219, 443, and 609 cm^{-1}. Given that the precursor itself contains no oxygen, and the CNT network is treated to provide > 99% carbon purity, it is hypothesized that the reactor chamber is susceptible to trace amounts of oxygen insertion during the experiment at the inlets of the rubber setpa whereby the electrical leads are passed through. To ensure an oxygen-free environment, modifications to the reactor set-up were investigated.

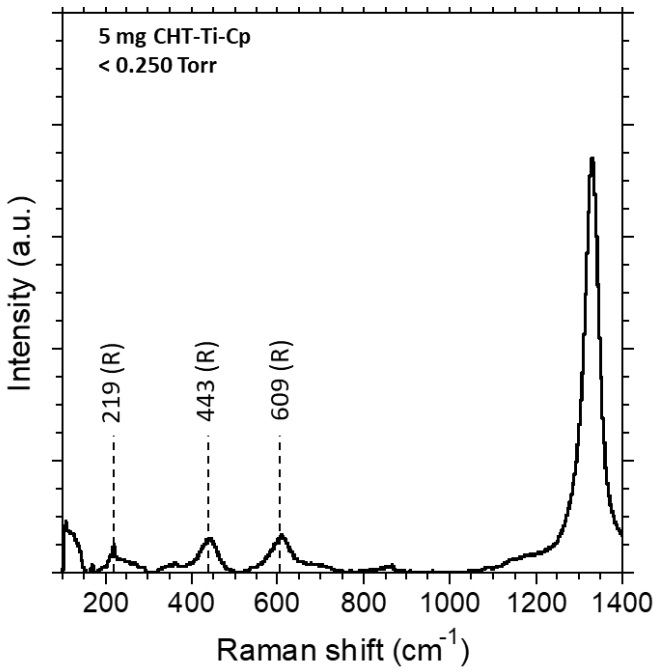

Figure 25 Raman spectroscopy measurements of a 5 mg CHT-Ti-Cp deposition onto purified Miralon CNT roving performed at < 0.250 Torr, with a 200 °C mantle temperature, and 250 mA applied current for 1 hour.

The standard three-neck flask set-up was modified to accommodate pressures greater than atmosphere, allowing for a continuous flow of 95% Ar / 5% H_2 (mol/mol) carrier gas throughout the reactor flask as shown in Figure 26. In this configuration, a pressure > 760 Torr is first applied, and then two 22 Ga. needles are quickly implemented to act as pressure release outlets, restricting entry of any foreign species at flask connection points. Throughout a CVD experiment, a constant flow of the argon formulate gas is maintained. Due to the presence of a carrier gas, it is expected that convective cooling will result in a lower temperature of the purified Miralon roving for a given applied bias. To account for this, CVD experiments presented here are conducted with an increased applied current of 300 mA, compared to the 250 mA used for vacuum experiments. Additionally, due to the higher pressure within the reactor flask, it is expected that the vapor phase precursor will encounter a greater amount of collisions prior to reaching the sample, and thus less

diffusion throughout the conductor is expected. Lastly, a mantle temperature of 200 °C is maintained to sublimate the CHT-Ti-Cp precursor, consistent with the temperature utilized for CVD depositions at < 0.250 Torr pressure, as the temperature of the mantle is in direct contact with the medium contacting the precursor and not expected to be influenced by pressure.

Figure 26 Picture of the three-neck flask set-up used for Joule-heating driven CVD, with 22 Ga. needles inserted into the outer necks' rubber septa to act as pressure releases.

The influence of precursor mass on the resultant deposition mass loading and morphology are presented in Figure 27a, using 10, 15, and 20 mg of precursor. Similar to experiments performed at < 0.250 Torr, the weight loading after deposition increases correspondingly with increasing precursor mass. However, it is notable here that for a given precursor mass, the resultant weight loading after deposition at > 760 Torr pressure was lower when compared to < 0.250 Torr depositions. A number of factors contribute to this phenomenon; it is expected that precursors will more readily sublimate at lower pressures, and additionally, a higher mass fraction of vapor phase precursor in the

gaseous phase will increase the amount of decomposition at the CNT surface. Moreover, convective cooling may lead to a reduction in temperature at the CNT surface, which is known to affect the mass deposited for some precursors [83]. A potential benefit in obtaining lower weight loadings via the > 760 Torr method is the ability to more finely control the mass loading at lower precursor masses, as precursor masses below 0.5 mg become increasingly challenging due to the accuracy of microbalances in a glovebox environment.

Secondary electron images reveal the morphology obtained at the various weight loadings. As seen in Figure 27b, utilization of 10 mg of CHT-Ti-Cp precursor lead to a coating that is closely bound to the CNT surface, following the network morphology and retaining pore structure. The morphology for the 10 mg deposition at >760 Torr deposition closely resembles that obtained for 0.7 mg depositions conducted at < 0.250 Torr pressure, which may be expected as the weight loading is similar between the two samples. However, an additional insight that can be leveraged from this observation is that the expected decrease in mean-free-path for the vapor phase precursor at > 760 Torr pressure likely had limited effects on the penetrability of the precursor throughout the network, evidenced by the similar levels of surface coating at similar weight loadings. Possibly the direction of gas flow aids in carrying the precursor through the network. Figure 27c shows that 15 mg precursor results in a coating of a film across the network, filling in the pores and only slightly retaining the visibility of the network morphology. Using 20 mg of precursor at >760 Torr pressure results in a full surface coverage, as seen with 4.7 mg at < 0.250 Torr pressure.

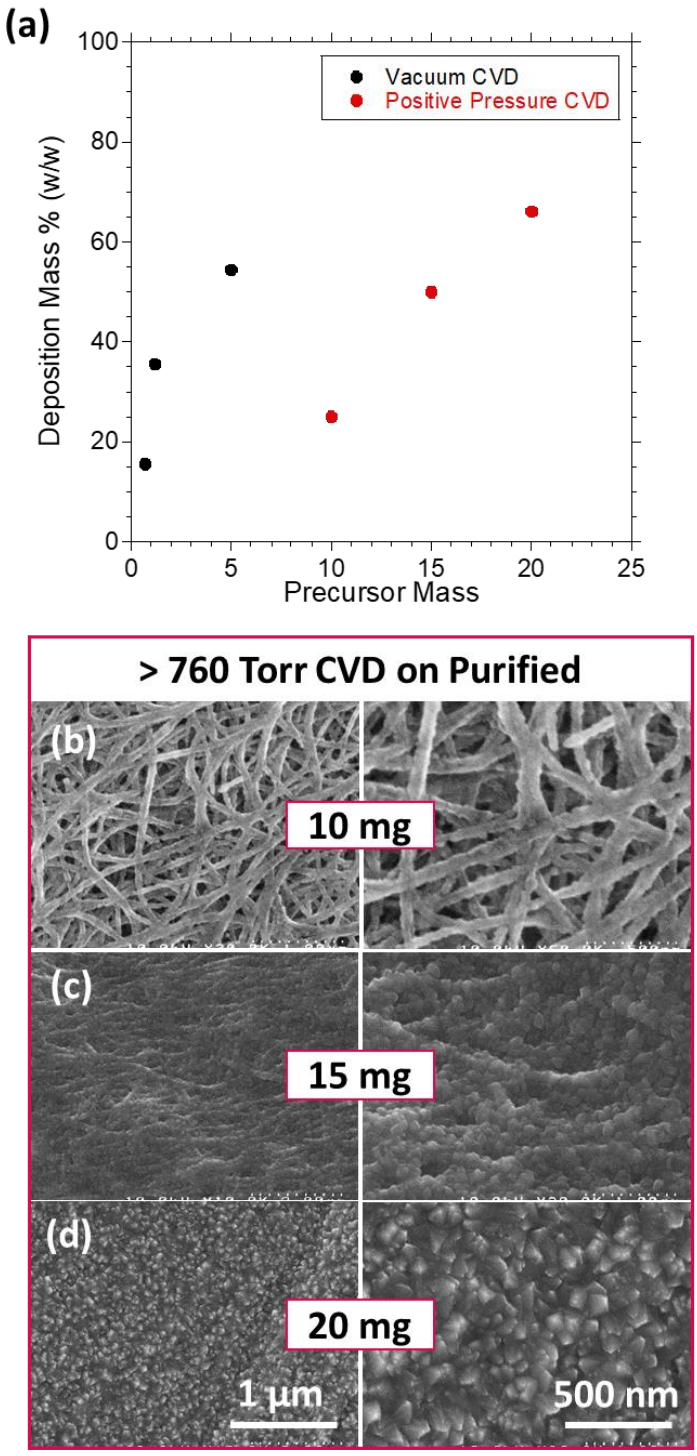

Figure 27 (a) Plot of the weight loading %w/w versus the starting precursor mass for CHT-Ti-Cp depositions performed at > 760 Torr, with a 200 °C mantle temperature, and 300 mA applied current for 1 hour. SEM images showing the morphology of the corresponding depositions with (b) 10 mg, (c) 15 mg, and (d) 20 mg CHT-Ti-Cp precursor.

Cross-sectional EDX mapping was performed to assess the diffusion of CHT-Ti-Cp throughout the volume of the CNT template for a >760 Torr CVD deposited sample with 25% w/w Ti (10 mg CHT-Ti-Cp precursor). It is observed that the precursor does successfully penetrate throughout the entire thickness, however, a higher concentration at the surface of the composite is noted, similar to that observed in previous studies, however, at a lower weight loading in this case [114]. The spectrum shown in **Figure 28**b confirms the presence of Ti with signal being registered for the Lα and Kα transitions.

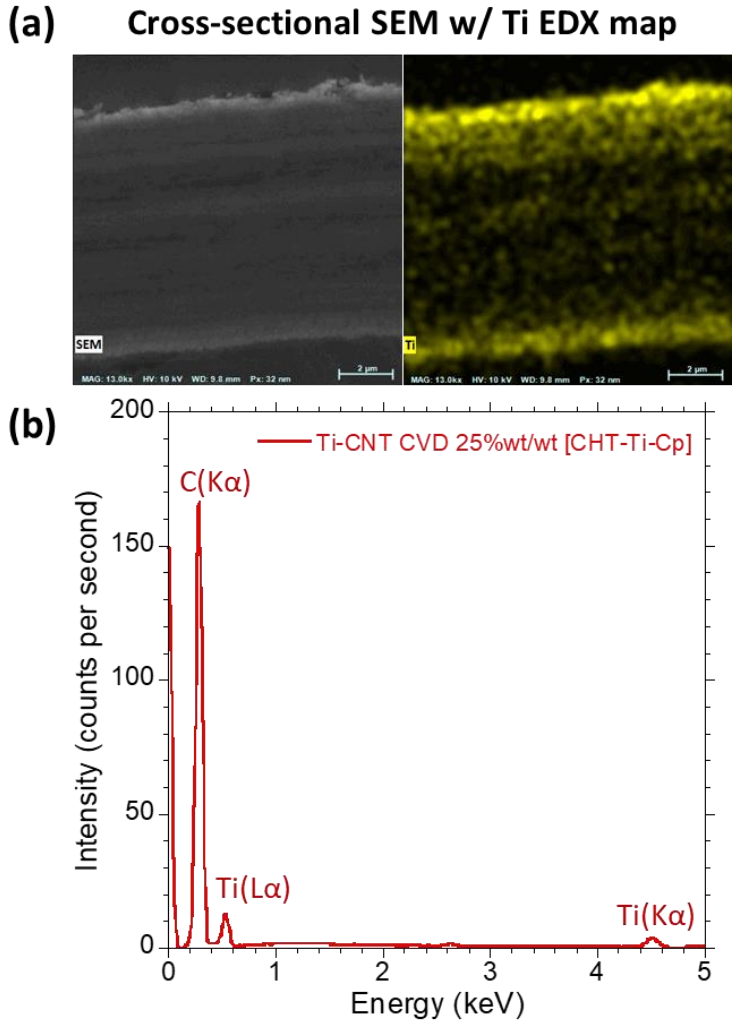

Figure 28 (a) Cross-sectional SEM of a 10 mg CHT-Ti-Cp deposition onto purified Miralon roving performed at > 760 Torr, with a 200 °C mantle temperature, and 300 mA applied current for 1 hour. (b) An overlay of the Ti signal, and (c) the corresponding EDX spectrum.

Raman spectroscopy showcases the standard graphitic peak and defect band associated with CNTs as described earlier, however, a lack of any peak corresponding to the vibrational modes for TiO_2 are present (see Figure 29), in contrast with that observed for the depositions performed at < 0.250 Torr. Environmental control is thus attributed as being a major factor influencing oxidation during growth. The reduction in amount of oxide present after CVD deposition demonstrates a path forward toward Ti-rich depositions throughout a 3-D CNT network, providing a direct approach toward the fabrication of fully interconnected Ti-CNT hybrids.

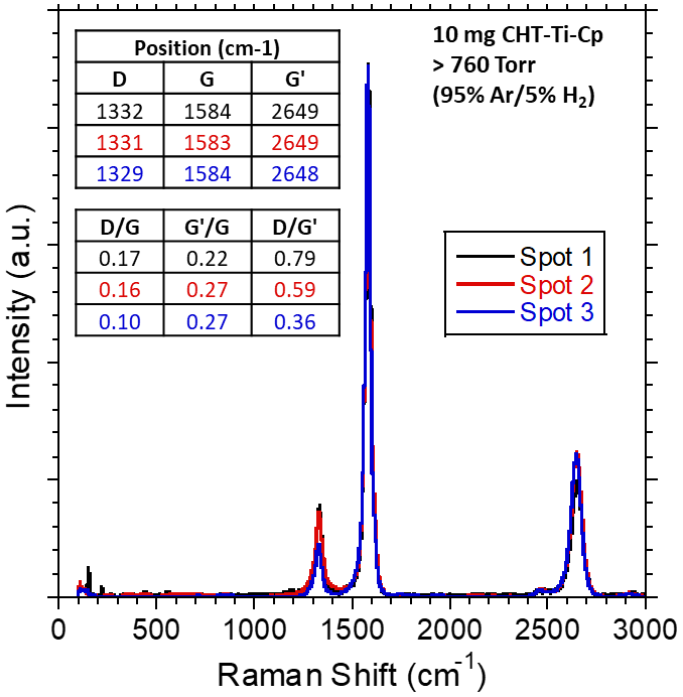

Figure 29 Raman spectroscopy measurements of a 10 mg CHT-Ti-Cp deposition onto purified Miralon CNT roving performed at > 760 Torr, with a 200 °C mantle temperature, and 300 mA applied current for 1 hour.

5.2 Evaluation of Metal Grain Structure on Hybrid Electrical Properties

To understand the impact of metallization on the electrical interconnection between CNT bundles, temperature-dependent electrical measurements were taken and

analyzed via electron transport modeling. A Janis VPF-800 cryostat was used to perform the temperature-dependent electrical measurements under 10^{-6} mbar vacuum. Multiple cycles of temperature sweeps from 80 – 600 K were performed with four-point probe I-V sweeps being carried out at 5 °C increments, using a National Instruments NI PXI-4110 programmable power supply and NI PXI-4072 digital multimeter to acquire the electrical measurements. **Figure 30** shows a typical I-V sweep measurement for metallized CNT hybrids, which is used to calculate resistance values. As shown previously, the first temperature cycle can modify material properties either through annealing, or desorption of weakly bound ambient species [99]. To ensure that analysis of the curves are representative of the permanent material characteristics, multiple temperature cycles were carried out until the temperature response during an up and down ramp remained stable (i.e. no change in response regardless of ramp direction).

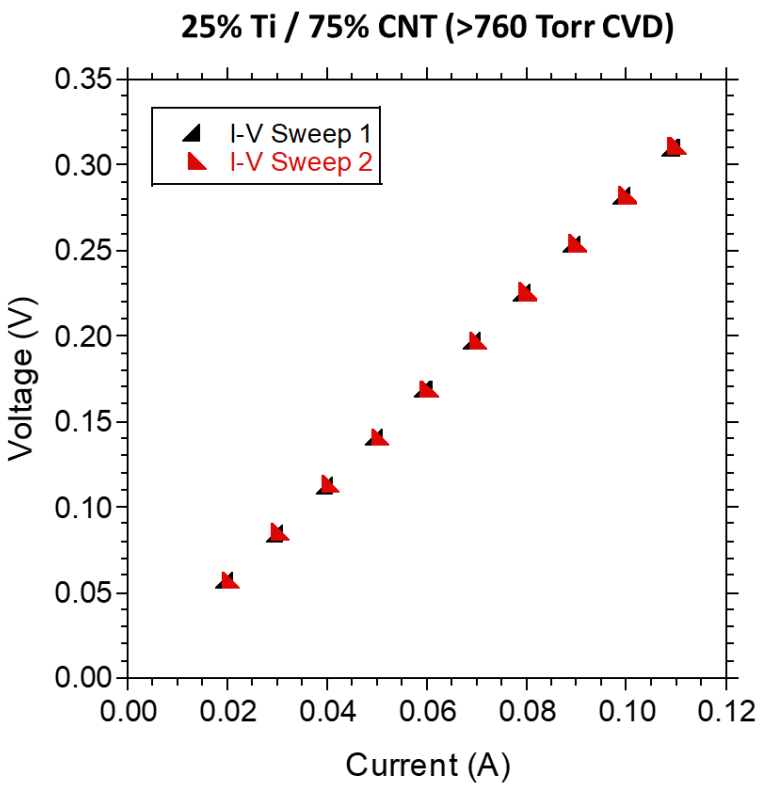

Figure 30 Individual I-V sweeps for a Ti-CNT sample fabricated using 10 mg CHT-Ti-Cp deposition onto purified Miralon CNTs performed at > 760 Torr, with a 200 °C mantle temperature, and 300 mA applied current for 1 hour. The I-V sweep in this figure represents a typical I-V response for the metallized CNT hybrids and is used to determine the resistance values for temperature dependent electrical data.

Figure 31 shows temperature-dependent electrical data taken for Ti-CNT composites fabricated with 0.7 and 5 mg CHT-Ti-Cp precursor at < 0.250 Torr pressure (16% and 54% w/w Ti respectively), as well as 10 mg CHT-Ti-Cp precursor deposited at > 760 Torr pressure (25% w/w Ti). Additionally, the samples prepared at < 0.250 Torr pressure were subjected to a 6 hour, 400 °C (673.15 K) vacuum anneal within the Janis cryostat at 10^{-6} mbar pressure to assess the impact of annealing on the temperature dependent properties. Conductivities were estimated based on average cross-sectional area of the Miralon. Fitting of the curves was performed using the Kaiser model [16] described in

1.4.1 using a generalized gradient algorithm that minimizes the sum of residual squares. The variable range hopping term generally plays a bigger role in thin film networks [29] and was correspondingly found to be insignificant for the networks used in this study; thus, the term was omitted for the fits presented here.

Generally, it is observed that after annealing to 400 °C for 6 hours, the conductivity of the Ti-CNT composites permanently decreases overall, at any given temperature. In the case of both 0.7 mg and 5 mg CHT-Ti-Cp depositions, an increase in both the phonon backscattering energy (calculated as $T_M \cdot k_B$) and the tunneling barrier energy ($E_B = T_B \cdot k_B$) is observed after annealing, which accounts for the decreased conductivity. For as-deposited samples, it is shown that increasing the weight loading of Ti when deposited at pressures of < 0.250 Torr leads to a decrease in the values of both T_M and T_B, which indicates a lower phonon scattering energy as well as a decreased tunneling barrier between CNT bundles. In fact, the calculated barrier energy is 4.92 meV at a weight loading of 16% w/w Ti, which is very similar to that observed for 21% w/w Pt seeded roving shown in other studies (4.66 eV) [118]. Moreover, the barrier energy decreases to 3.32 meV as the weight loading increases to 54% w/w Ti, another trend of which is also observed in Pt seeded conductors. The addition of metal at higher weight loadings contribute to a lower average tunneling barrier as additional contact points are bridged within the CNT network, providing evidence that the metal deposition is leading to electrical interconnection.

The Ti-CNT conductors fabricated at pressures < 0.250 Torr are shown earlier to have some amount of TiO_2 present, however, some amount of the deposited coating is in the form of Ti or TiC, evidenced by the fact that the samples are still conductive. Thus,

the Ti present is attributed to the low tunneling barrier obtained. Temperature-dependent electrical measurements were also taken for a Ti-CNT conductor that was fabricated via CVD at > 760 Torr pressure, to assess if the presence of TiO_2 in the samples fabricated at < 0.250 Torr influence the electrical interface. In this case, a Ti-CNT conductor with 25% w/w Ti was modeled and exhibits a tunneling barrier energy of 2.40 meV, which is lower than that obtained for samples fabricated at < 0.250 Torr pressure even with higher weight loadings. Thus, minimizing the amount of TiO_2 in the deposited coatings is attributed to providing a lower barrier height between CNTs.

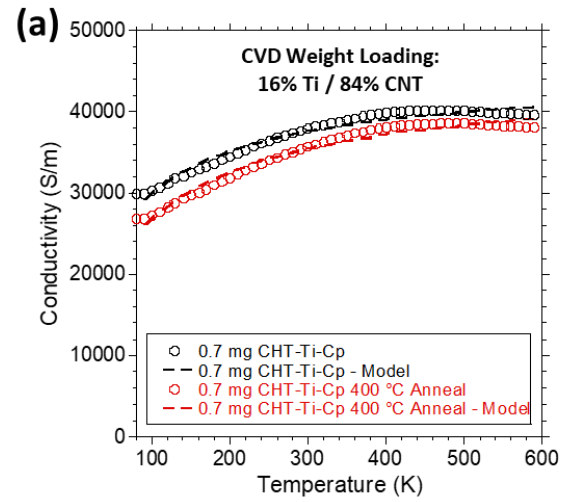

<250 mTorr CVD

Model Parameter	As-deposited	400 °C Anneal
A (Ω·μm)	15.78	15.78
T_m (K)	26881	27043
B (Ω·μm)	22.55	22.66
T_b (K)	57.11	78.75
T_s (K)	55.38	68.49
SQRT x^2/SUM	0.23%	0.25%
k_bT_b (meV)	4.92	6.79

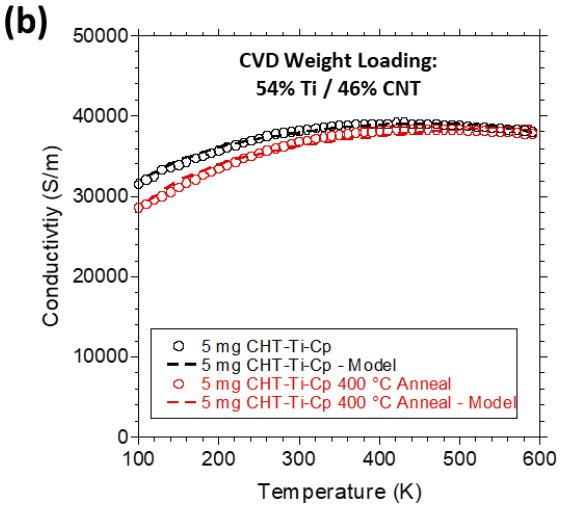

<250 mTorr CVD

Model Parameter	As-deposited	400 °C Anneal
A (Ω·μm)	851	15.78
T_m (K)	3778	12304
B (Ω·μm)	23.42	24.01
T_b (K)	38.48	43.42
T_s (K)	28.42	22.76
SQRT x^2/SUM	0.10%	0.23%
k_bT_b (meV)	3.32	3.74

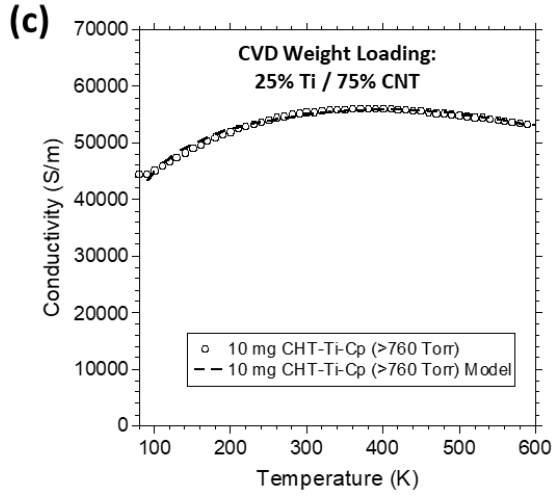

>760 Torr CVD

Model Parameter	As-deposited
A (Ω·μm)	96.88
T_m (K)	2442
B (Ω·μm)	16.53
T_b (K)	27.80
T_s (K)	2.92
SQRT x^2/SUM	0.11%
k_bT_b (meV)	2.40

Figure 31 Temperature-dependent electrical measurements with curve fitting results for (a) 0.7 mg, and (b) 5 mg CHT-Ti-Cp depositions onto purified Miralon CNTs performed at < 0.250 Torr, with a 200 °C mantle temperature, and 250 mA applied current for 1 hour. (c) 10 mg CHT-Ti-Cp deposition onto purified Miralon CNTs performed at > 760 Torr, with a 200 °C mantle temperature, and 300 mA applied current for 1 hour.

5.3 Transferability of Process Principles to another Material System: W-CNT Hybrids

The effectiveness of pure Ti as an adhesion metal on CNTs is benefitted from its wettability, temperature stability, and low contact resistance to CNTs. W is an alternative metal that exhibits similar properties to Ti with respect to CNTs, but also has a tendency to form stable oxides. The processing principles developed for the Ti-CNT system are evaluated in this section for a W-CNT composite to assess the effectiveness of the process and establish the basis for an alternative metal-CNT system.

5.3.1 Vacuum CVD (< 0.250 Torr)

In this study, the purified Miralon roving described in section 5.1.1 is used as the base CNT material, and the resulting material properties after CVD are assessed via a combination of electron microscopy, energy dispersive X-ray spectroscopy, mass measurements, and Raman spectroscopy.

A three-neck flask set-up is used for the deposition of W via Joule-heating driven CVD as described in earlier works. A single strand of purified Miralon CNT roving is suspended between two electrical leads passed through rubber septa enclosing the outer two necks. The flask is brought into a glovebox purged under an argon environment. The precursor was massed inside of the glovebox using a Mettler Toledo XP-2U microbalance to measure masses as low as 3 mg. Bis(cyclopentadienyl) Tungsten(IV) (CAS# 1271-33-6, Sigma-Aldrich 97%) [$W(Cp)_2H_2$] was used as the precursor in this study. The massed precursor was transferred into the three-neck flask within the glovebox and the flask was transferred into a hood equipped with a Schlenk line to control the environment of the flask. The Schlenk line system consists of two lines; one line for delivering 95% Ar/5% H_2 gas, and the other for pulling vacuum on the system.

Joule-heating driven CVD was performed (as described in earlier works [27, 83, 114]) using $W(Cp)_2H_2$ onto purified Miralon roving at a pressure of < 0.250 Torr, a mantle temperature of 150 °C, and a continuously applied current of 250 mA for 1 hour.

The coating morphology of CVD deposited CNTs is assessed using a Hitachi S-4000 scanning electron microscope via secondary electron imaging, using a working distance of 8 mm and an accelerating voltage of 10 kV. Elemental analysis of the surface of the composite was performed using a Tescan Mira3 SEM equipped with a Bruker XFlash 6|30 EDS at a 10 kV accelerating voltage. A Mettler Toledo XP-2U microbalance is used to acquire the mass before and after deposition in order to determine weight loading.

The results of one hour depositions using precursor masses of 3, 11, and 18 mg at 200 °C and < 0.250 Torr onto purified Miralon CNT roving biased at 250 mA are presented in **Figure 32**. As expected, an increase in the amount of precursor mass leads to an increase in metal mass loading after deposition, which is observed for other precursors as well [27, 83]. SEM images show that the W precursor deposits a coating with spikey morphology when using 3 or 11 mg of precursor. As seen in **Figure 32**b, the network morphology is still visible at low magnification, however, the pores within the network are fully filled at the surface. A thicker coating is observed when using 11 mg, and the spike-shaped features are more pronounced. As the precursor mass is increased to 18 mg, a smoother surface is observed.

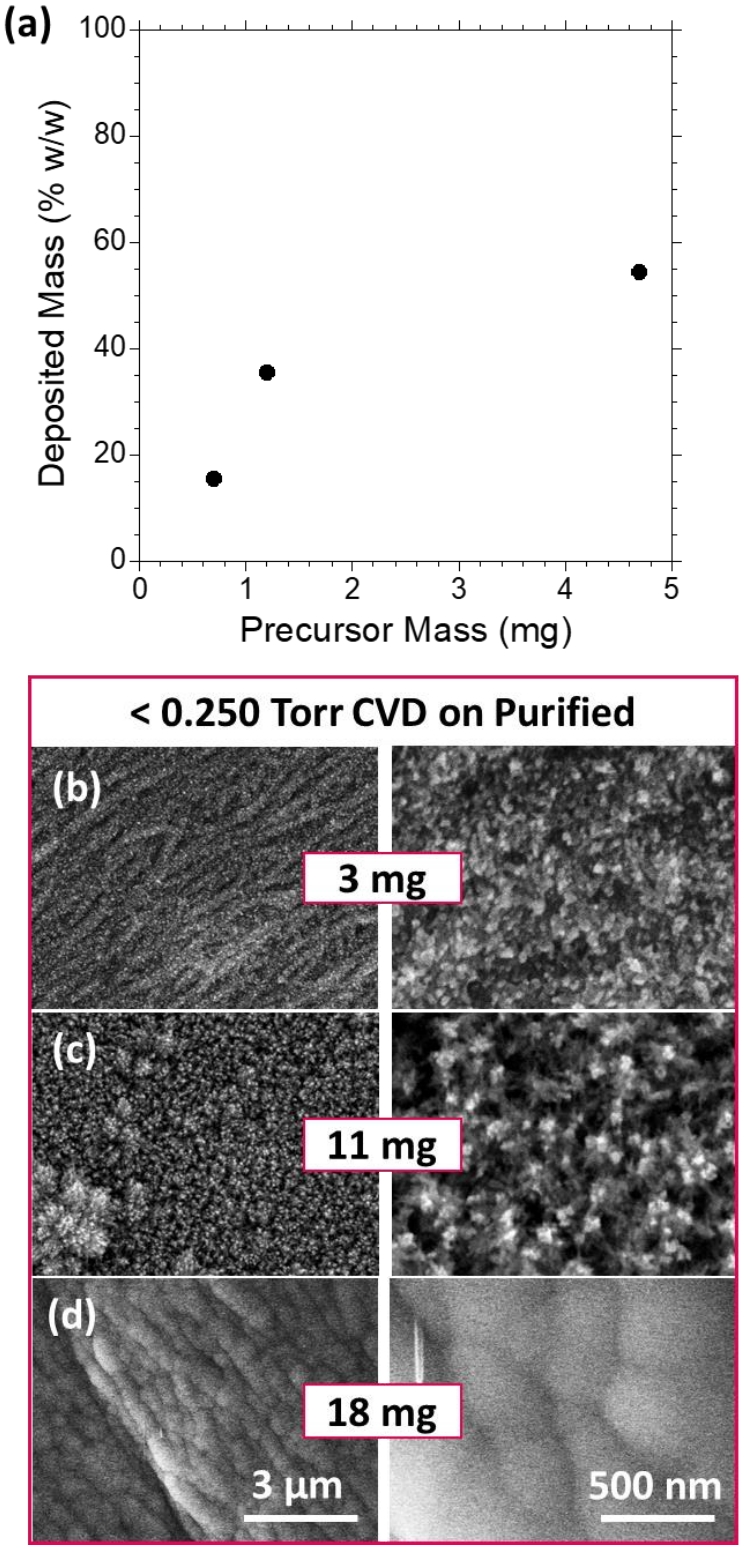

Figure 32 (a) Plot of the weight loading %w/w versus the starting precursor mass for $W(Cp)_2H_2$ depositions performed at < 0.250 Torr, with a 150 °C mantle temperature, and 250 mA applied current for 1 hour. SEM images showing the morphology of the corresponding depositions with (b) 3 mg, (c) 11 mg, and (d) 18 mg $W(Cp)_2H_2$ precursor.

Raman spectroscopy was performed to assess the state of the W deposited onto the CNTs (see **Figure 33**). Standard peaks representing sp^2 and sp^3 bonded carbon, noted as the graphitic (or G) and defect (or D) peaks, respectively, are observed. However, in addition to these peaks, five WO_3 peaks are also observed at 129, 265, 322, 695, and 804 cm^{-1}. The peaks identified for WO_3 closely resemble those reported in literature for h-WO_3 at 161, 251, 321, 691, and 817 cm^{-1}[119].

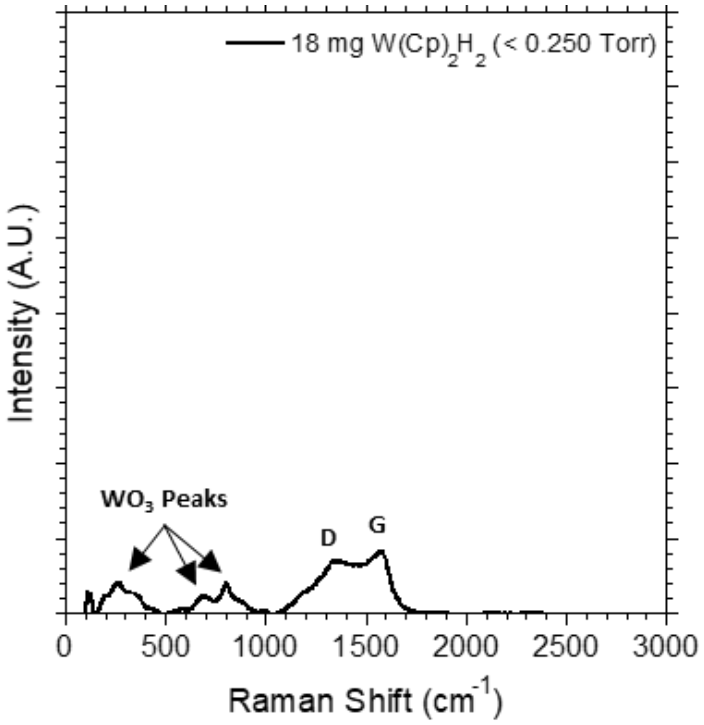

Figure 33 Raman spectroscopy measurements of an 18 mg $W(Cp)_2H_2$ deposition onto purified Miralon CNT roving performed at < 0.250 Torr, with a 150 °C mantle temperature, and 250 mA applied current for 1 hour.

It has been reported that WO_3 can be reduced to pure W in a hydrogen environment in less than an hour annealing time at temperatures between 500-900 °C [120]. Herein, annealing in a 95% Ar/ 5% H_2 environment was performed in a Lindberg/Blue M(HTF55322A) tube furnace at multiple temperatures from 500 to 900 °C for 1 hour on a quartz boat to attempt to reduce the deposited W after CVD deposition.

Raman measurements on the annealed samples show that the peaks associated with WO_3 remain after annealing to 500 and 600 °C, however, successful reduction is achieved at 900 °C, whereby all peaks related to oxides are vacant, and a pristine CNT curve is observed from beneath the surface (see **Figure 34**). Moreover, a significant recovery of the D/G ratio is observed, indicating that the high temperature annealing didn't negatively impact the CNT structure.

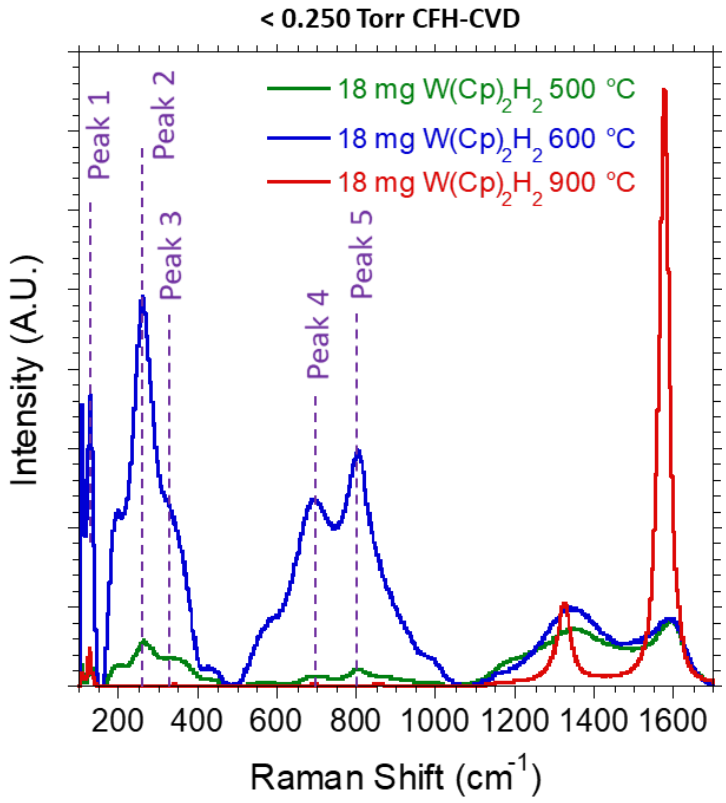

Figure 34 Raman spectroscopy measurements of an 18 mg $W(Cp)_2H_2$ deposition onto purified Miralon CNT roving performed at < 0.250 Torr, with a 150 °C mantle temperature, and 250 mA applied current for 1 hour after annealing to 500, 600, and 900 °C in a 95% Ar/ 5% H_2 environment.

Phase	Peak 1	Peak 2	Peak 3	Peak 4	Peak 5
As-deposited	129	265	322	695	804
Anneal – 500 °C	130	263	332	697	805
Anneal – 600 °C	129	260	324	691	803
*h-WO_3	161	251	321	691	817
*m-WO_3	134	271	330	712	806

Table 3 Raman shift peak locations (reported in cm^{-1}) associated with WO_3. h-WO_3 and m-WO_3 values referenced from literature [119].

Additionally, secondary electron images show the impact of annealing on the surface morphology of the W (see **Figure 35**). No clear trend is established between anealing and grain structure, however, it is demonstrated that the W coating is stable on the CNT surface at temperatures up to 900 °C, maintaining a uniform and continuous coating. Thus, W is demonstrated here to have high temperature stability on the surface of CNT networks.

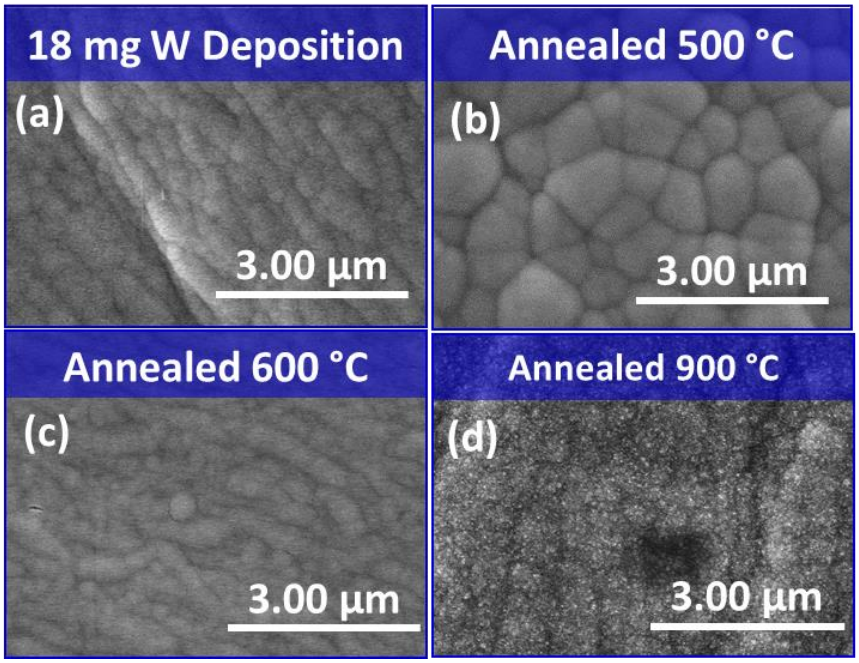

Figure 35 Surface SEM measurements of an 18 mg $W(Cp)_2H_2$ deposition onto purified Miralon CNT roving performed at < 0.250 Torr, with a 150 °C mantle temperature, and 250 mA applied current for 1 hour as-deposited and after annealing to 500, 600, and 900 °C in a 95% Ar/ 5% H_2 environment.

5.3.2 >760 Torr CVD

Annealing in a reducing atmosphere successfully converted the CVD deposited WO_3 film to pure W. Joule-heating CVD at > 760 Torr pressure is explored as an alternative route to achieve W-rich films by encouraging a pure W deposition onto the CNTs during growth. In this study, the modified three-neck flask set-up was used to accommodate pressures greater than 760 Torr, with a continuous flow of 95% Ar / 5% H_2 (mol/mol) gas as shown in **Figure 26**. CVD experiments presented here are conducted with an applied current of 300 mA for 1 hour, using a mantle temperature of 150 °C to sublimate a $W(Cp)_2H_2$ precursor.

The influence of precursor mass on the resultant deposition mass loading and morphology are presented in **Figure 36**a, using 5, 10, and 21 mg of precursor. As observed in the case for CHT-Ti-Cp deposition at > 760 Torr, the weight loading after deposition increases correspondingly with increasing precursor mass. Furthermore, it is again observed here that for a given precursor mass, the resultant weight loading after deposition at > 760 Torr pressure was lower when compared to < 0.250 Torr depositions, which is attributed to the lower mass fraction of vapor phase precursor as described earlier as well as potential convective cooling effects.

Secondary electron images showcase the morphology obtained at the various weight loadings. As seen in **Figure 36**b, utilization of 5 mg of CHT-Ti-Cp precursor led to a continuous and uniform coating that adheres closely to the to the CNT network morphology. Notably, the surface texture is much more smooth in comparison to the spike-shaped features obtained via < 0.250 Torr depositions of $W(Cp)_2H_2$. The morphology for the 10 mg and 21 mg depositions performed at >760 Torr deposition

show greater amount of filling due to the higher weight loading. Importantly, depositions at all weight loadings showcase a smoother surface texture without the presence of spike-shaped features that were observed in the < 0.250 Torr depositions, which may be resultant of oxide formation.

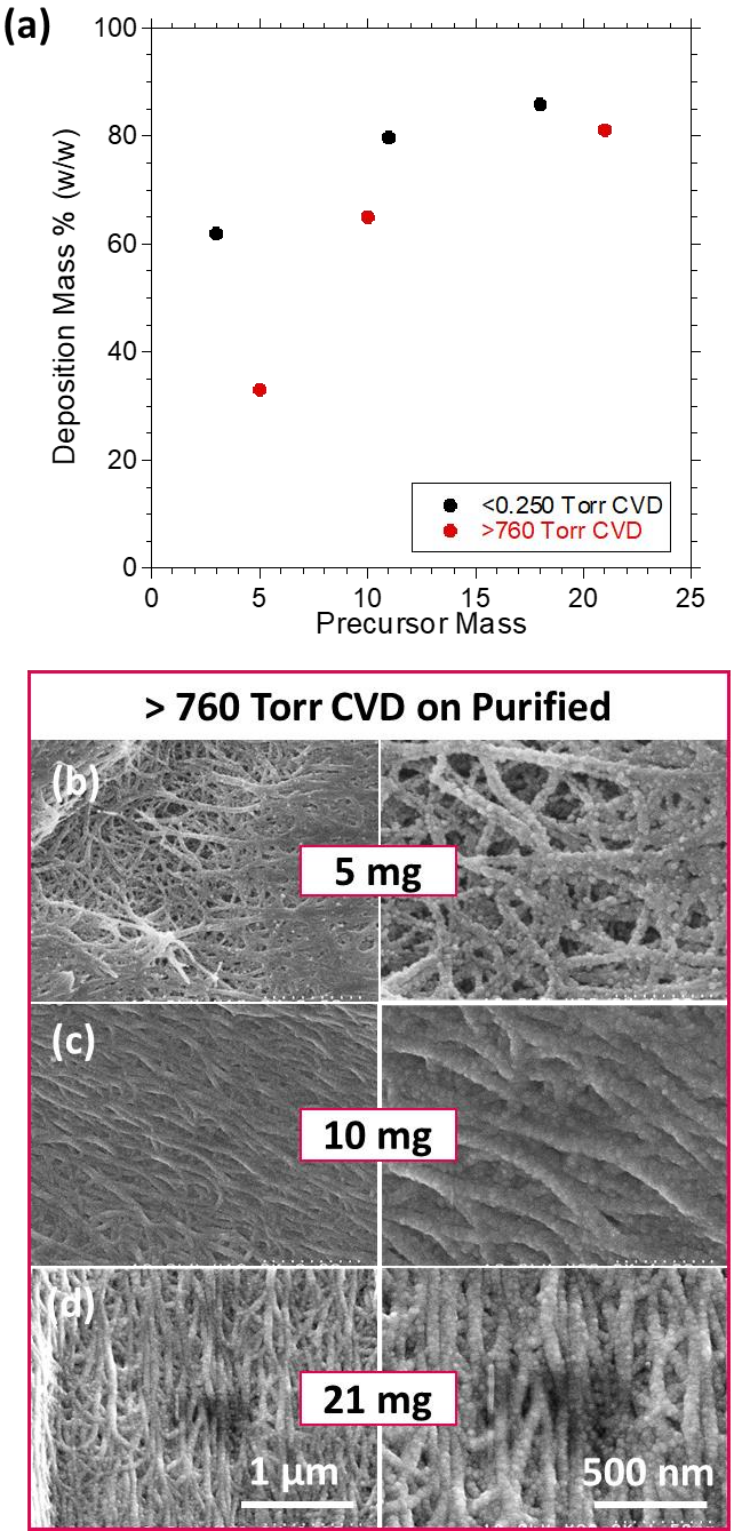

Figure 36 (a) Plot of the weight loading %w/w versus the starting precursor mass for $W(Cp)_2H_2$ depositions performed at > 760 Torr, with a 150 °C mantle temperature, and 300 mA applied current for 1 hour. SEM images showing the morphology of the corresponding depositions with (b) 5 mg, (c) 10 mg, and (d) 21 mg $W(Cp)_2H_2$ precursor.

To verify the deposition of W onto the CNTs, surface-view EDS mapping was performed on a W-CNT sample with a weight loading of 65% w/w, shown in Figure 37. Uniform coverage of W is shown across the surface of the CNTs, with a strong W signal confirming the presence of W. The confirmation of W deposition validates $W(Cp)_2H_2$ as a viable precursor for CVD depositions of W onto CNT networks.

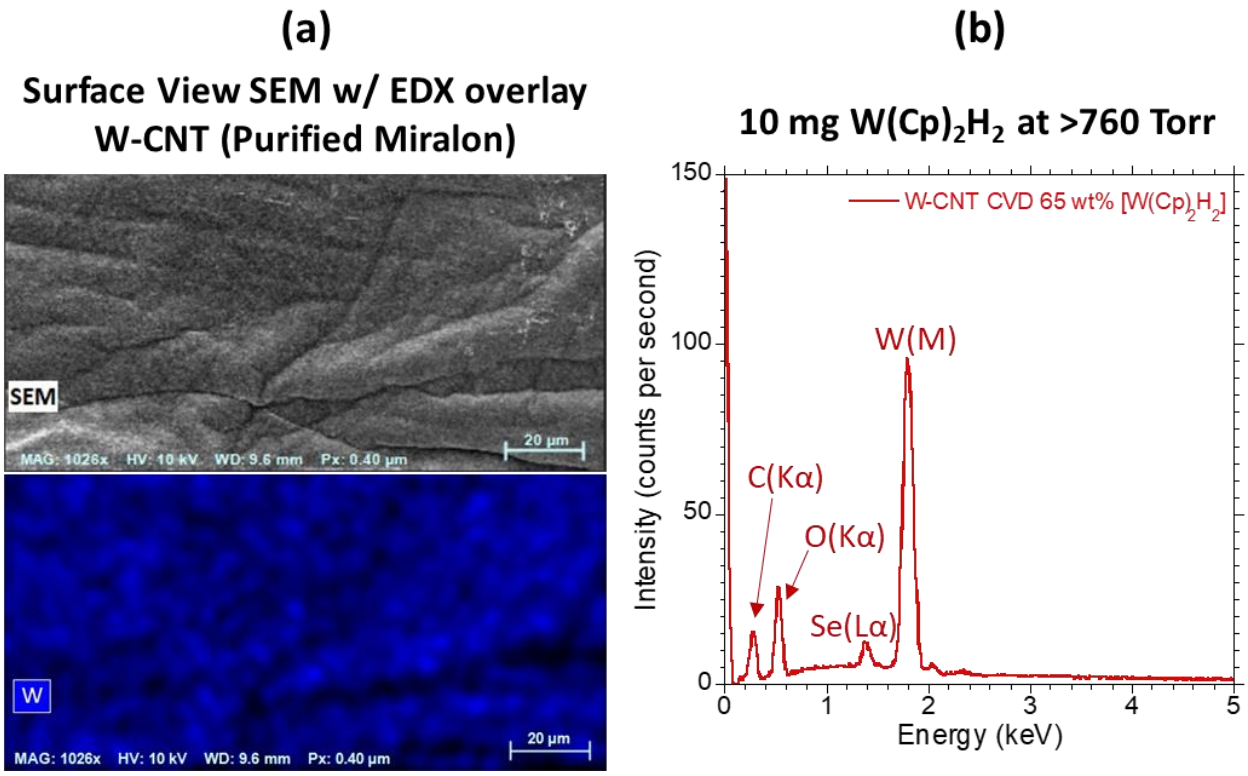

Figure 37 (a) Surface-view SEM of a 10 mg $W(Cp)_2H_2$ deposition on purified Miralon CNTs performed at > 760 Torr, with a 150 °C mantle temperature, and 300 mA applied current for 1 hour. EDX map overlay of W signal in bottom image. (b) Corresponding EDX spectrum.

Raman spectroscopy was performed to understand the phase of W deposited onto the CNTs, shown in **Figure 38**. Standard G, D, and G' peaks are observed for the W-CNT composite, which correspond to the vibrational modes observed in CNTs. No peaks are observed that would correspond to WO_3, however, which is consistent with that observed for >760 Torr CVD depositions performed with CHT-Ti-Cp, whereby oxide formation was minimized. Moreover, a small amount of signal is registered at 690 and

860 cm^{-1}, which has been identified as the vibrational modes for WC [121]. There are two potential sources of WC formation: (1) during deposition, it is possible that W bonds at the outer walls of the CNT surface to form a carbide; (2) the precursor itself contains two five-membered carbon rings, which could dissociate to WC during the fragmentation of the precursor. Either way, WC is known to have a thermal conductivity of 110 W/mK as well as a low resistivity (~0.2 μΩ·m) [122], which could be beneficial for metal:CNT interconnection.

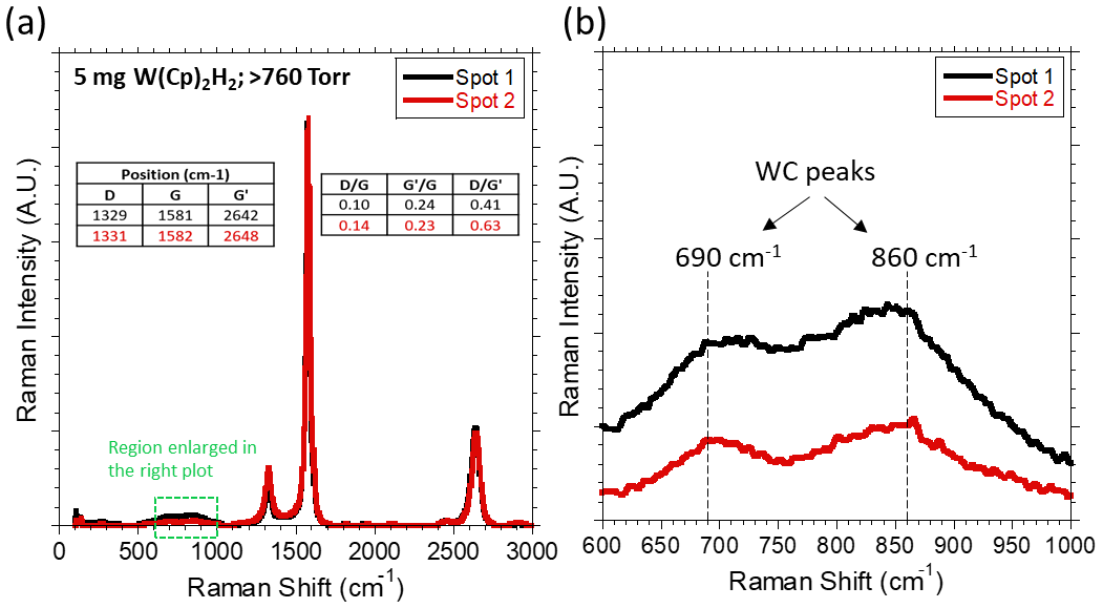

Figure 38 (a) Raman spectroscopy measurements of a 5 mg $W(Cp)_2H_2$ deposited purified Miralon CNT roving at > 760 Torr, with a 150 °C mantle temperature, and 300 mA applied current for 1 hour, with (b) an enlarged plot to show the WC peaks.

Overall, the work here demonstrates the ability to reliably deposit either WO_3 or pure W by controlling the reactor environment. W-CNT composites provide an effective template to probe the oxidation state via Raman due to the large number (5) of detectable oxide peaks, and their relatively high intensity. WO_3 films are shown to be reducible to metallic W by annealing at 900 °C for 1 hour in a 95% Ar/ 5% H_2 environment, while CVD at > 760 Torr is shown to deposit oxide-free W, providing two paths toward W-rich coatings

on the CNT surface. Additionally, the lack of tungsten oxide formation during CVD deposition at > 760 Torr pressure with the $W(Cp)_2H_2$ precursor corroborates the observation of oxide-free Ti deposition shown earlier using the CHT-Ti-Cp precursor, further cementing the ability to deposit Ti-rich or W-rich films.

5.4 Outcomes

The work presented in this chapter has provided an understanding of the influence that reactor environment and pressure have on the deposition properties. Success of oxide-free deposition was achieved using a pressure > 760 Torr in an inert/reducing environment, attributed to the absence of any leaks. However, modifying the pressure also influences other aspects of the deposition dynamics. Namely, at pressures > 760 Torr, lower weight loadings are deposited for a given precursor mass, and thus, finer control over low weight loadings is possible. Additionally, depositions at > 760 Torr offer a route towards CVD onto CNT samples that are sensitive to vacuum environments. At the same time, for applications where higher weight loadings are desirable, deposition at < 0.250 Torr benefits from achieving higher weight loadings while using less precursor. Moreover, a vacuum environment enables longer mean-free-paths for vapor-phase precursors, which may affect diffusion dynamics during deposition. For follow-on studies, an alternative set-up could be implemented in which the reactor flask is situated within an environmental enclosure. In this manner, the flask could be held under vacuum, while the surrounding environment is purged with argon, such that any potential leaks into the flask would be inert. Such a set-up would allow for the study of the pressure effects on the reaction dynamics more closely.

6 Dissertation Conclusions and Impact

The dissertation focused on the nature of adhesion metal interactions with carbon nanotubes. In particular, Ti, Ni, and W were explored as candidate metals due to their wettability, ability to form carbides, and their low contact resistance to CNTs. Multiple deposition techniques were evaluated to create both 2-D thin film structures as well as the use of a novel CVD approach for 3-D deposition. Sample processing methods such as annealing and temperature-cycling were explored to understand the stability of the metals at elevated temperature. The sample test structures were interrogated by SEM, Raman spectroscopy, etc. to explore the morphology and structure that was produced. Electrical measurements and mass characterization provided detailed relationships between experimental conditions and the resulting physical properties. Each of these experiments were directed at understanding the fundamental interaction and susceptibility to electroplated coatings for enhanced hybrid conductors. Ultimately, the experimental work was complemented by a physics-based model to extract parameters that can aid in understanding the conduction mechanism for novel hybrids. The outcomes of each chapter section are provided below as well as summary for the dissertation impacts along with pathways for future work.

Chapter 3 utilizes thermal evaporation to directly evaluate the interfacial characteristics of a 2-D Ti film on a CNT ribbon conductor. Specifically, a 10 nm layer of Ti was shown via secondary electron imaging to deposit continuously and uniformly along the CNT network, indicative of a high binding energy to the CNTs as-deposited. The 10 nm Ti layer was demonstrated to maintain a tightly adhered coating up to 400 °C for 1 hour in 95% Ar / 5% H_2, warranting its use as an adhesion metal for elevated

temperature applications. A 100 nm Cu layer was deposited onto the as-received CNT conductor and annealed to 400 °C, resulting in gap formation throughout the film as the Cu began to delaminate from the surface due to poor interaction. Additionally, as a result of film delamination, the annealed Cu-Ti-CNT hybrid increased in resistance by 40%. Utilizing a 10 nm Ti layer in a Cu-Ti-CNT hybrid succesfully suppressed delamination of the Cu overcoat, and achieved a 12% reduction in the resistance per length, demonstrating the advantages of Ti as an adhesion metal for elevated temperature applications.

Chapter 4 demonstrates the ability to deposit Ti throughout the entire volume of a porous 3-D CNT conductor via Joule-heating driven CVD using a CHT-Ti-Cp precursor. The diffusion of Ti throughout the ~30 μm thickness was verified through cross-sectional EDS mapping, showing for the first time the fabrication of integrated bulk Ti-CNT conductors via this technique. Moreover, control over coating morphology and weight loading is demonstrated by varying precursor mass, achieving coatings tightly bound to the CNT network geometry as well as fully connected thin films on the bulk conductor surface. Additionally, electroplating was employed to fabricate Cu-Ti-CNT hybrids, achieving conductivities as high as 43.1 MS/m after densification and annealing, which is the highest value reported in literature for bulk metal-CNT conductors at 98% or lower metal mass loading. Favorable interaction between the metals and the CNTs resulted in a TCR of 3.49×10^{-3} K^{-1}, combined with a specific conductivity of 6257 Sm^2/kg, which results in a conductor that surpasses the specific conductivity of pure Cu at or above a temperature of 250 °C. This work demonstrates the fabrication of advanced metal-CNT

hybrids that can provide direct energy savings during operation at elevated temperatures for applications such as high efficiency motors.

Chapter 5 establishes CVD reactor environment controls that enable either mixed Ti-oxide or oxide-free depositions, performing depositions at < 0.250 Torr or > 760 Torr in a 95% Ar/ 5% H_2 envinronment. Depositions performed at > 760 Torr are shown to have lower resultant weight loadings for a given starting precursor mass when compared to depositions performed at < 0.250 Torr, allowing for higher precision of control when targeting low masses. Additionally, Raman spectroscopy measurements indicate a lack of oxide formation during depositions at > 760 Torr. The control over oxide formation was verified by depositing W onto CNTs at < 0.250 Torr and > 760 Torr, corroborating the same trends observed for Ti depositions. The W-CNT acts a useful template for probing oxide formation due to WO_3 having 5 easily detectable peaks measurable by Raman. Moreover, in depositions performed at > 760 Torr pressure, the presence of WC was observed, indicating an oxygen-free reaction environment. The results here demonstrate a path toward W-rich and Ti-rich throughout a 3-D porous CNT conductor.

Additionally, in Chapter 5, the impact of oxide formation as well as weight loading on the electrical properties of the Ti-CNT conductors is evaluated via modeling of the temperature-dependent conductivity. Curve fitting revealed that the tunneling barrier between CNT bundles within the network decreased with increased weight loading of Ti deposited at < 0.250 Torr pressure. Furthermore, Ti deposited at > 760 Torr was determined to have an even lower tunneling barrier than depositions performed at < 0.250 Torr, even with higher weight loadings, attributed to the reduced amount of oxides present within the metal coating. The modeling performed herein directly supports the

theory that the deposited metals provide enhanced electrical interconnection between the CNT bundles.

Thus, overall, this work has established the ability to deliver Ti throughout a 3-D CNT network with control over the morphology, oxide formation, and electrical interconnection for the fabrication of advanced Cu-Ti-CNT hybrids with high conductivities and low TCRs. As a result, this dissertation has demonstrated the ability of Ti to act as a temperature-stable adhesion metal for electrical interconnection in Cu-Ti-CNT hybrids, which can provide direct energy savings in elevated temperature applications. Additionally, Joule-heating driven CVD offers conductor fabrication scalability, enabling opportunities for commercialization. Future developments to the scalability of CVD will require modifications to the chamber geometry such that larger samples and alternative Joule-heating can be utilized. Additional work that can systematically control the pressure level while retaining inert atmosphere can probe the mean-free-path dynamics during deposition. Development of electroplating-based processing on a series of higher adhesion metal deposited samples can potentially enable the commercialization of these advanced conductors for use in applications such as high efficiency motors. Exploring modifications to the electroplating approach, including AC-based plating and the use of electrolytic additives, may provide enhancements to the deposited coatings and their interaction with the carbon nanotubes. Adapting these techniques and insights onto other CNT types (i.e. SWCNT, DWCNT, etc.) and geometric articles (i.e densified sheets, wires, etc.) may enable their functionality in applications requiring cylindrical wire formats for electrical applications, or sheet formats for electrode based applications. Overall, the utility of both adhesions metals for hybrid

CNT conductors and the benefits of using joule-heating CVD to realize the depositions show tremendous promise in this emerging field of metal-CNT conductors.

7 Appendix A: Additional Experiments

Data sets included here are based on screening experiments to better understand CVD parameters. The experiments performed here were sufficiently rigorous to be valid, but don't fit into a complete story, and are intended to explore alternative experimental pathways.

7.1 Serial Deposition towards Ti Passivation

A potential source of oxidation for Ti coatings on CNTs can come from environmental exposure. Encapsulation of the Ti layer can prevent the formation of native oxides by eliminating exposure to the environment. Serial CVD deposition is suggested to coat a Ti layer with a Cu overcoat prior to exposure to the ambient environment. In this way, a CVD deposition of 7.5 mg CHT-Ti-Cp was performed at < 0.250 Torr with a mantle temperature of 200 °C and applied current of 350 mA for one hour. Immediately after the Ti deposition was performed, the flask was transferred into a glovebox, where 13 mg of $Cu(acac)_2$ precursor was loaded into the flask. The flask was then transferred back to the Schlenk line and a subsequent CVD deposition was performed at the same conditions. **Figure 39** shows the surface morphology of the Ti-CNT and Cu-Ti-CNT depositions. A spike-shaped morphology is observed the Ti, which is shown to be stable after an anneal to 300 °C in 95% Ar / 5% H_2. The Cu deposition appears to have some degree of coating on the spike-shaped features, with additional spherical particles throughout. After annealing, the spherical Cu particles grow in size, however, the coating underneath the spheres remains intact as well, suggesting that the Ti layer may be helping with the adhesion of the Cu. More studies are needed to encourage a continuous Cu coating along the surface, potentially by focusing on improving the Ti adhesion layer through oxide-free deposition controls.

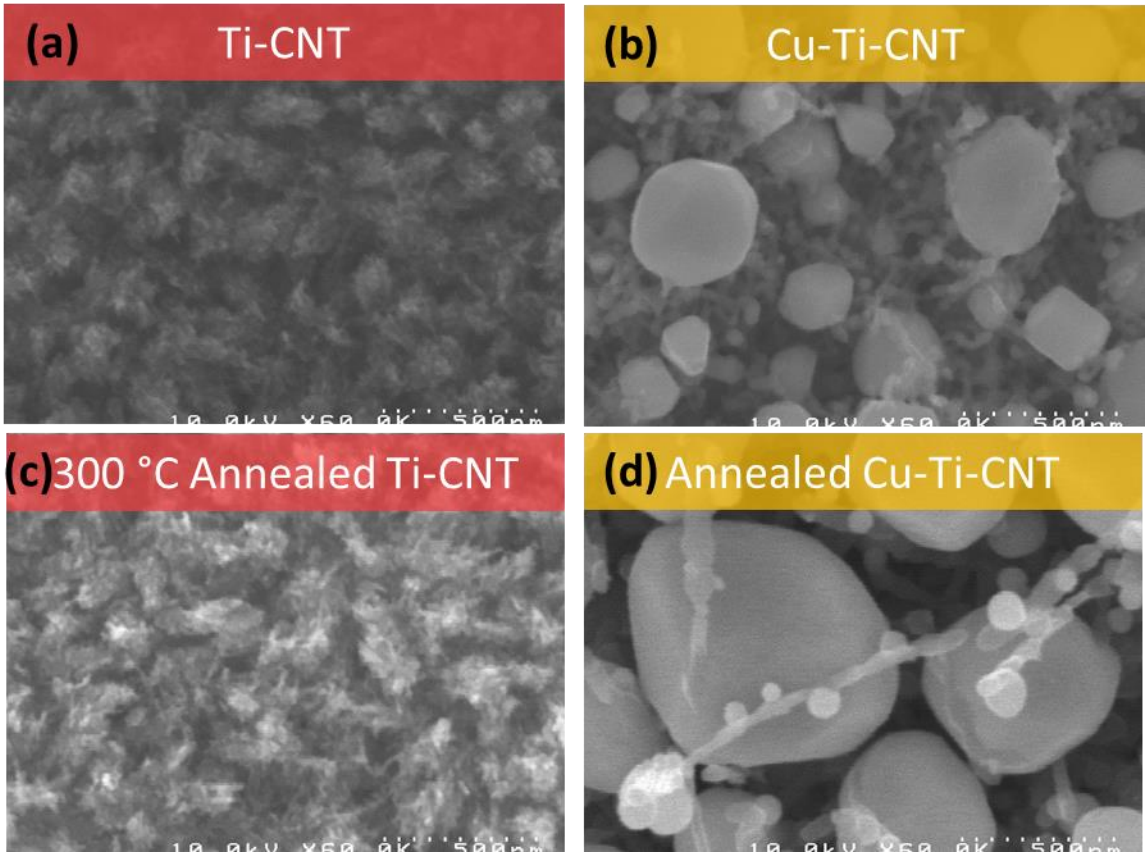

Figure 39 Surface SEMs of (a) as-deposited 7.5 mg CHT-Ti-Cp and (b) serially deposited 13 mg $Cu(acac)_2$, as well as (c,d) after a 300 °C anneal in 95% Ar / 5% H_2 for 1 hour, respectively . Both depositions were performed at < 0.250 Torr with a mantle temperature of 200 °C and applied current of 350 mA for one hour.

7.2 CVD on DexMat

In this study, DexMat is explored as an alternative CNT material for use in CVD depositions. As-received DexMat 1 cm film was laser cut to a width of 2 mm and length of 12.5 cm, to achieve comparable dimensions to that of Miralon CNT roving. A temperature calibration was performed by electrically biasing the 2 mm laser-cut DexMat film and measuring the resultant temperature profile with an IR camera (shown in **Figure 40**).

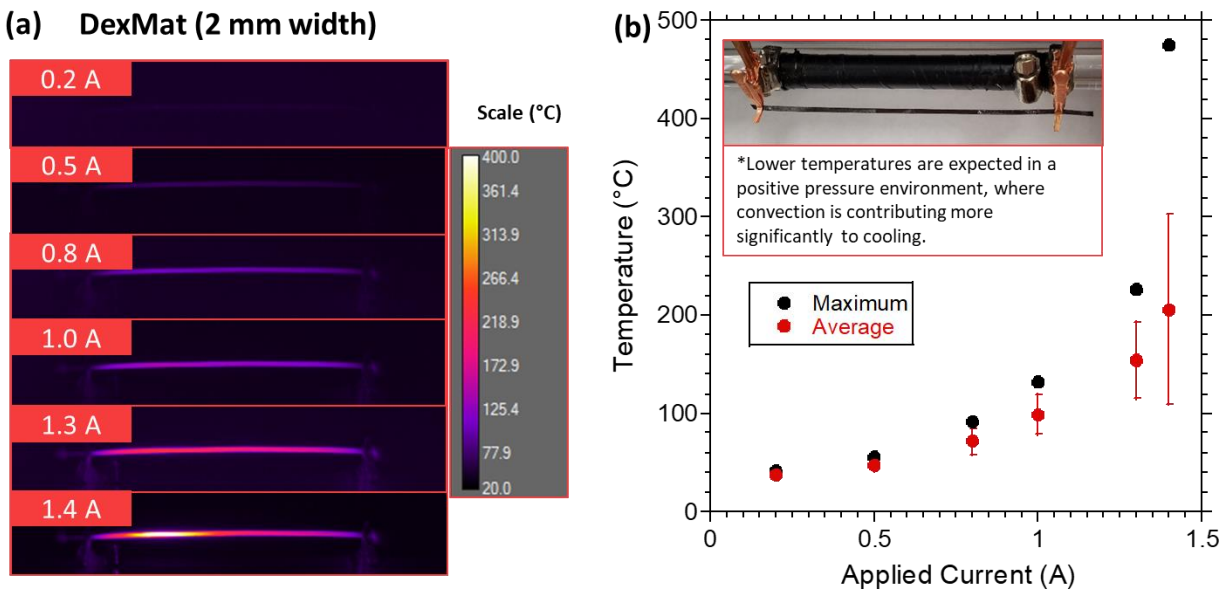

Figure 40 (a) IR images of the 2 mm wide laser cut DexMat film biased at currents ranging from 0.2 to 1.4 A, as well as (b) the corresponding average and maximum temperature of the conductor at each applied current.

Joule-heating driven CVD was performed on the 2 mm laser-cut DexMat film using 21.3 mg CHT-Ti-Cp precursor with a constant flow of 95% Ar/ 5% H_2 (>760 Torr), a mantle temperature of 200 °C, and electrical bias of 1.3 A for 1 hour, resulting a deposition of 36% w/w Ti. **Figure 41** shows the surface morphology of the Ti, showcasing the successful deposition of a fully connected film on the surface.

It is worth noting here that, despite having similar dimensions to the Miralon roving, and depositing with matched conditions, CHT-Ti-Cp CVD performed on DexMat achieved a weight loading of only 36% compared to the 66% obtained on Miralon. Several factors influence the amount of deposition that occurs during a run. It has been shown in this dissertation that the amount of starting precursor mass directly affects the resultant weight loading after CVD. Furthermore, decreasing reactor pressure results in higher weight loading depositions as well, attributed to the fact that powdered precursor more readily sublimes at lower pressures. Similarly, previous studies have shown that

increasing mantle temperature also increases the deposited mass [83]. Lastly, the amount of applied current has been shown to impact the deposition properties due to the temperature distribution resulting from Joule-heating [83]. In such a manner, alternate CNT templates may exhibit different temperature profiles due to CNT network properties (such as alignment and density), which can alter the resultant deposition properties as observed here.

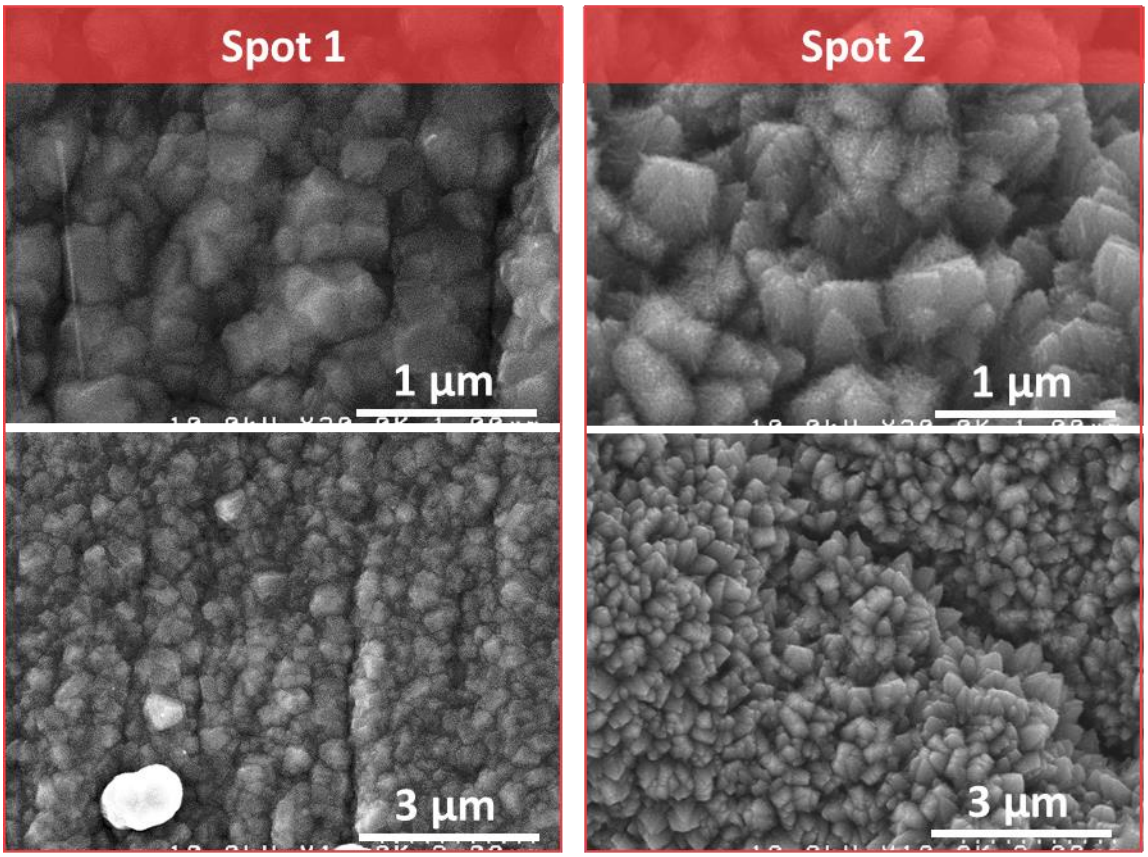

Figure 41 Surface SEM images of a 21.3 mg CHT-Ti-Cp deposition onto 2 mm laser-cut DexMat ribbon at > 760 Torr, with a 200 °C mantle temperature, and 1.3 A applied current for 1 hour.

In addition to Ti deposition onto DexMat, W deposition was performed for comparison. Joule-heating driven CVD was performed on the 2 mm laser-cut DexMat film using 21.3 mg $W(Cp)_2H_2$ precursor with a constant flow of 95% Ar/ 5% H_2 (>760 Torr), a mantle temperature of 200 °C, and electrical bias of 1.3 A for 1 hour. **Figure 42** shows the

surface morphology of the W, whereby a very light coating is observed, following along the network morphology.

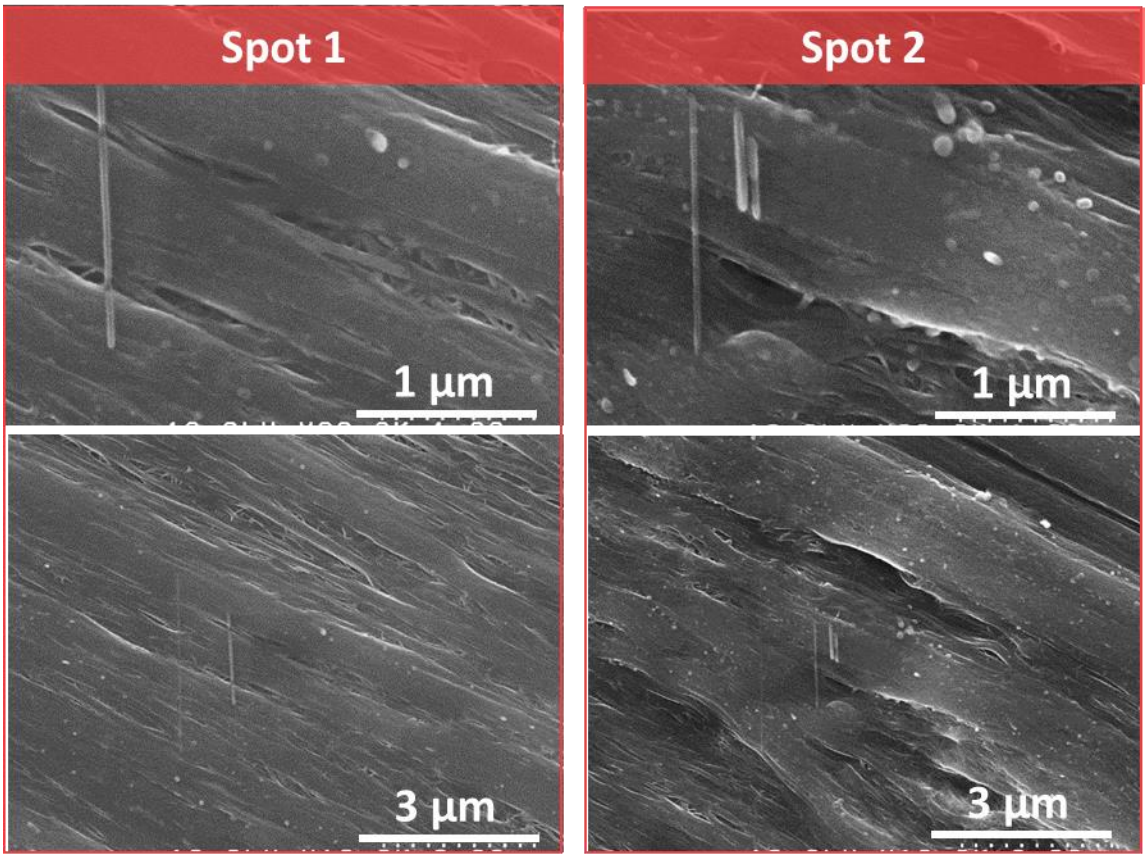

Figure 42 Surface SEM images of a 21.3 mg $W(Cp)_2H_2$ deposition onto 2 mm laser-cut DexMat ribbon at > 760 Torr, with a 150 °C mantle temperature, and 1.3 A applied current for 1 hour.

Surface EDS mapping confirms the presence of W, with a uniform distribution across the surface (**Figure 43**). Additionally, Fe and S are found in the sample, which likely result from the catalyst used to synthesize the CNTs, and the acids used to process the CNT product (such as chlorosulphonic acid, which contains S).

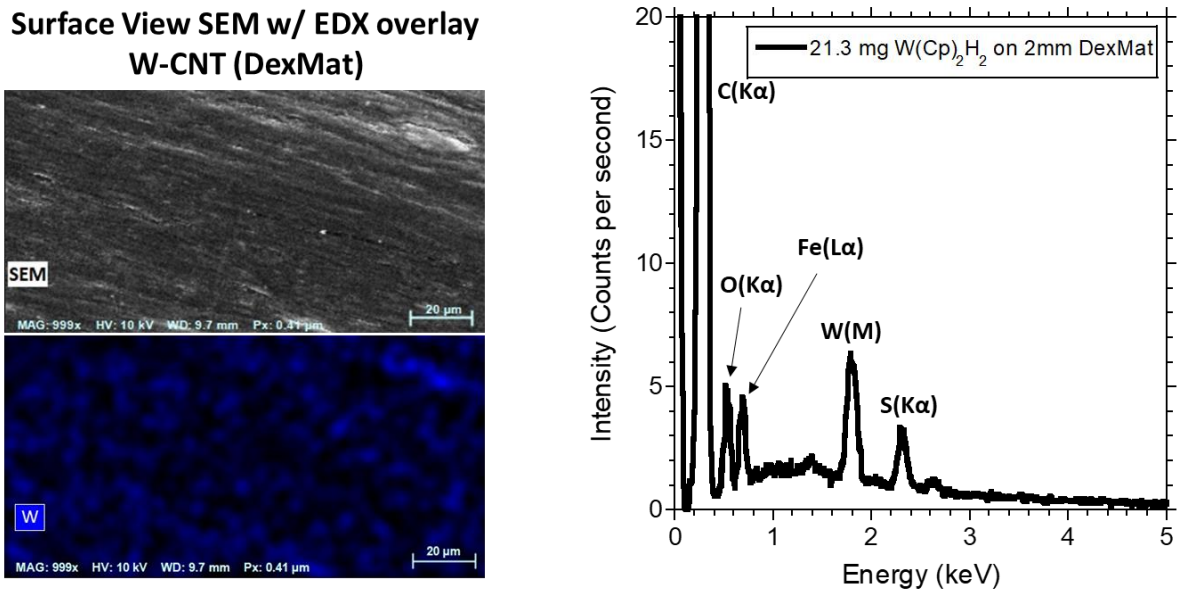

Figure 43 (a) Surface-view SEM of a 21.3 mg $W(Cp)_2H_2$ deposition onto 2 mm laser-cut DexMat ribbon at > 760 Torr, with a 150 °C mantle temperature, and 1.3 A applied current for 1 hour. EDX map overlay of W signal in bottom image. (b) Corresponding EDX spectrum.

Raman spectroscopy indicates the lack of an oxide present; however, a weak signal is measured where peaks for WC are expected, consistent with that observed for W depositions on the purified Miralon roving (shown in **Figure 44**).

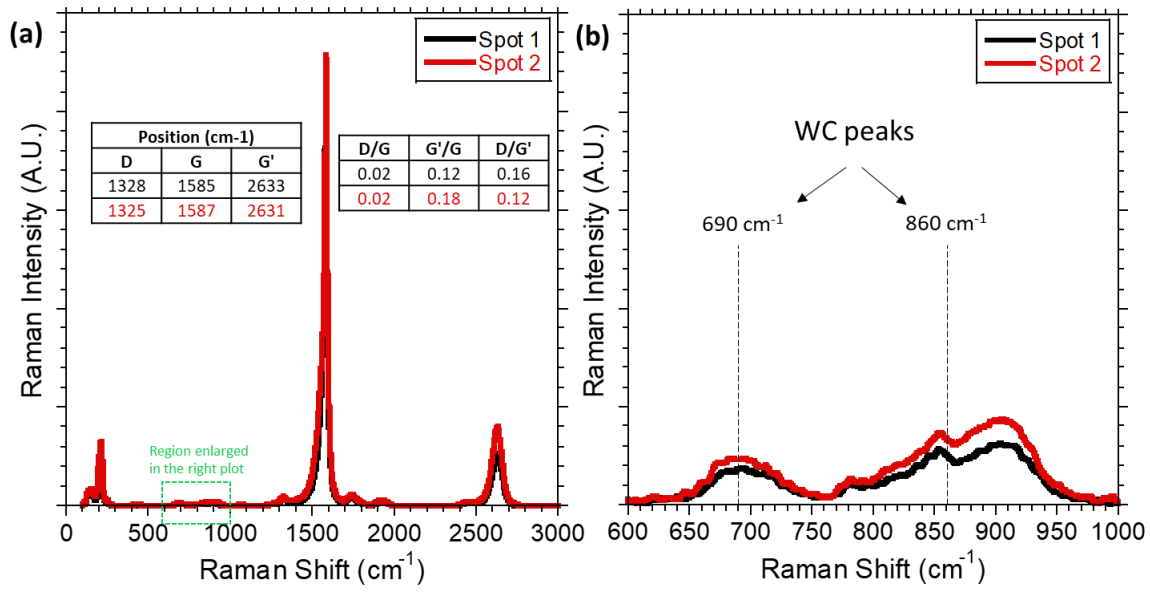

Figure 44 (a) Raman spectroscopy measurements of a 21.3 mg $W(Cp)_2H_2$ deposition onto 2 mm laser-cut DexMat ribbon at > 760 Torr, with a 150 °C mantle temperature, and 1.3 A applied current for 1 hour, with (b) an enlarged plot to show the WC peaks.

The M/L of the W-CNT (DexMat) did not change after W deposition. It is hypothesized that some amount of mass is lost in the beginning of the Joule-heating CVD process due to desorption of residual dopants present from the DexMat fabrication process. To determine the amount of mass deposited, thermogravimetric analysis was performed, whereby the mass of as-received DexMat and W-deposited DexMat were measured in-situ while ramping the temperature up to 1000 °C at 10 °C/min in air. The as-received DexMat shows a steady decline in normalized weight % until around ~600 °C. This decrease at lower temperatures may be resultant of residual dopants and/or acids used during the fabrication of DexMat. Furthermore, the W-CNT sample shows a more stable weight % for the first 200 °C, which additionally supports the theory that the Joule-heating driven CVD process desorbed species prior to the deposition of W. After reaching 1000 °C, the only elements that will remain in the sample are the metals present – Fe catalyst (shown to be present in EDX scans shown in **Figure 43**), and the deposited W. A comparison of the residual mass left after reaching 1000 °C for the as-received and W-CNT was used to calculate a 6.1% mass loading of W on the sample.

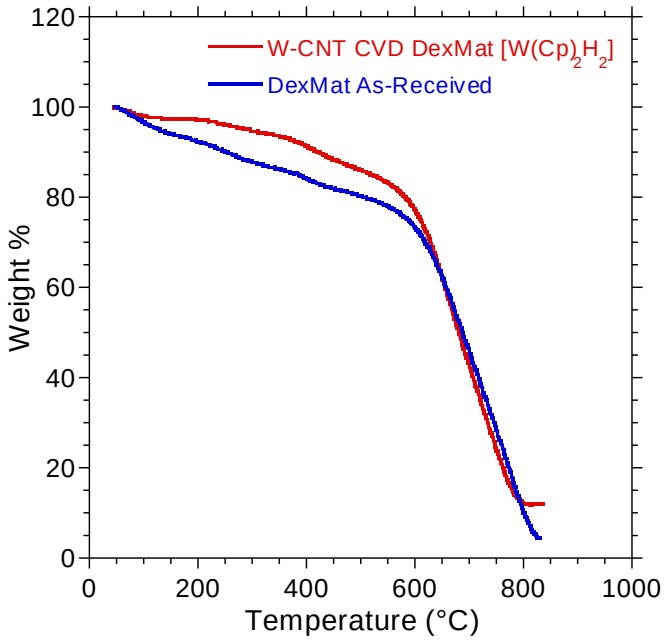

Figure 45 Thermogravimetric analysis measurements of as-received DexMat and a 21.3 mg $W(Cp)_2H_2$ deposition onto 2 mm laser-cut DexMat ribbon at > 760 Torr, with a 150 °C mantle temperature, and 1.3 A applied current for 1 hour.

7.3 IR Measurements of Various CNT Templates

Thermal imaging with an IR camera was performed on a variety of CNT templates under electrical bias to generate an understanding of the temperature dynamics for use in CVD or other applications. The CNT templates evaluated here consist of the following:

(1) Purified Miralon CNT roving subjected to a thermal oxidation up to 560 °C at 10 °C/min ramp, followed by an HCl rinse for 30 minutes, and an additional thermal oxidation with the same conditions

(2) An experimental 40 tex Miralon roving

(3) The 40 tex Miralon roving with ultrasonically welded Cu pads for improved current distribution over the wide injection area

(4) As-received DexMat 1 cm film

(5) As-received DexMat 1 cm film with ultrasonically welded Cu pads for current distribution

(6) Laser-synthesized SWCNT ribbon cut from a purified paper.

The average temperature measured for a given applied current for each sample is shown in **Figure 46**. In general, it is shown that the wider samples generate less heat at a given current, which results from the lower resistance. Additionally, it is found that for the widest samples (DexMat 1 cm film and 40 tex roving), hot spots accrue at the electrical contact points. Ultrasonically welding Cu pads onto these samples results in a cooler contact region, and improves the uniformity of the temperature profile overall. Thus, it is shown here that it is crucial to use Cu pads on wider samples for proper current distribution and improved heating uniformity.

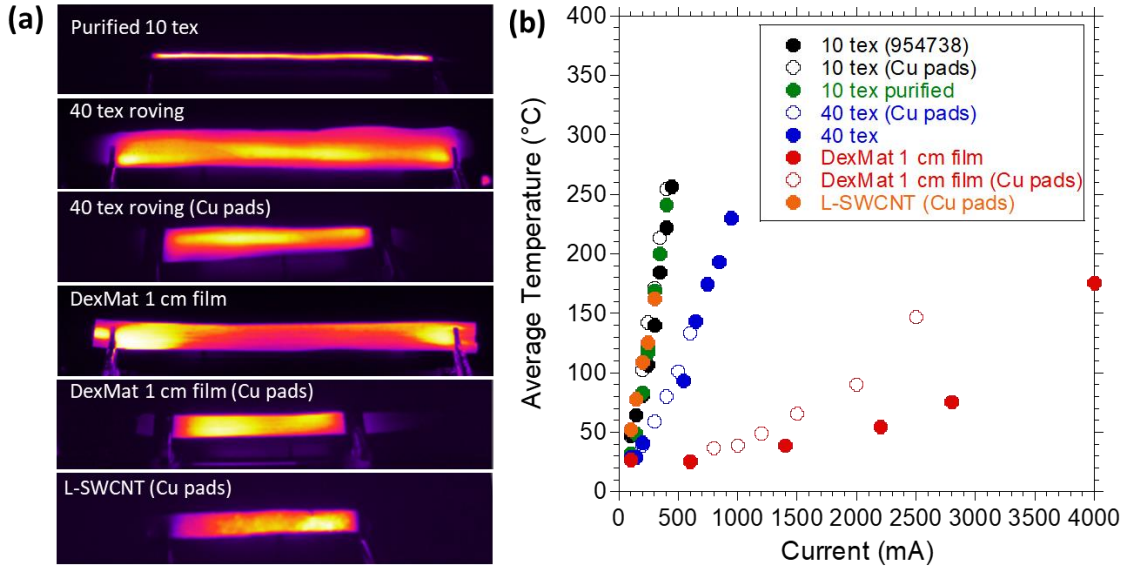

Figure 46 (a) IR images of various CNT templates biased at currents at a range of currents up to 4 A, as well as (b) the corresponding average temperature of the conductors at each applied current.

7.4 Alternative Ti Precursors

7.4.1 Dimethylbis(t-butylcyclopentadienyl) Titanium (IV) [tCp_2-Ti-Me_2]

Dimethylbis(t-butylcyclopentadienyl) Titanium (IV) [tCp_2-Ti-Me_2] was selected as an alternative precursor to evaluate the performance of Ti on the CNT roving seeded via

CFH-CVD. The CVD process was conducted under static 0.300 Torr vacuum, with three roving in parallel biased at 350 mA/roving for 1 hour. The mantle temperature was held at 200 °C. A precursor mass of 6.5 mg lead to a weight loading of 25.1% w/w. As observed in Figure 47, 6.5 mg of tCp_2-Ti-Me_2 precursor was sufficient to coat the CNTs with a thin film while maintaining some of the network morphology. Finishing of the 6.5 mg tCp_2-Ti-Me_2 seeded conductor was performed by electroplating in a sandwich cell configuration in Transene Cu acid solution at a current of 10 mA, followed by densification and annealing at 300 °C for 3 hours in a reducing environment. The finished 6.5 mg tCp_2-Ti-Me_2 seeded conductor (97.4% Cu / 0.7% Ti / 1.9% CNT) exhibited a specific conductivity of 3874 $S \cdot m^2/kg$, and conductivity of 36 MS/m, based on cross-sectional SEM (see Figure 47b). Thus, tCp_2-Ti-Me_2 is shown here to be a viable precursor for fabrication of high conductivity Cu-Ti-CNT hybrids.

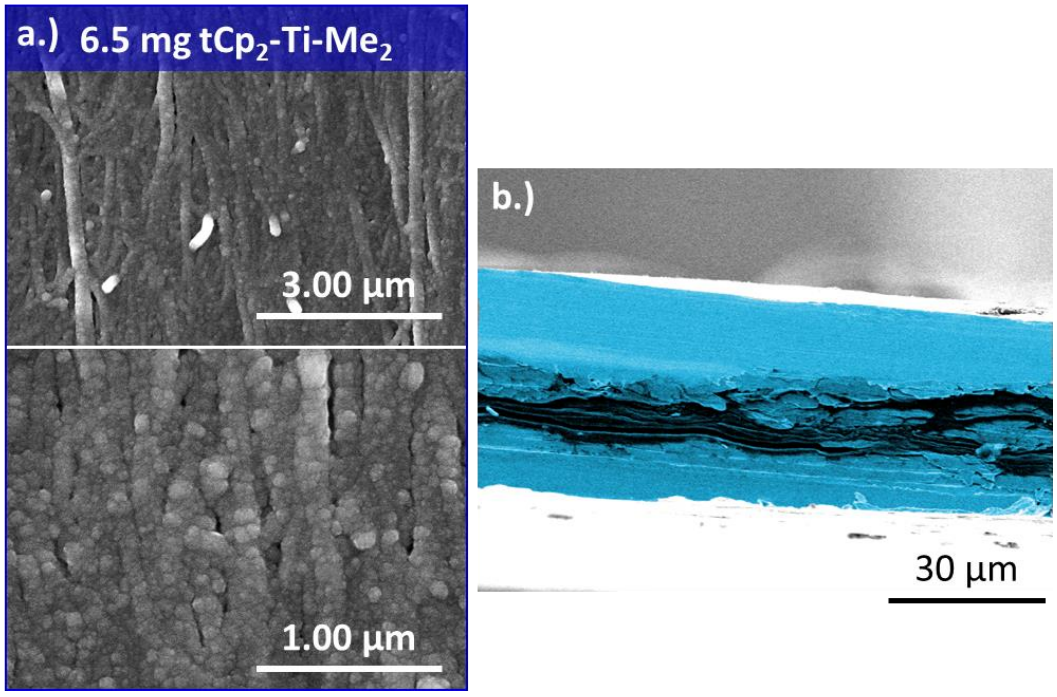

Figure 47: a.) Surface SEM images of the 6.5 mg tCp_2-Ti-Me_2 seeded CNT roving. b.) False-colored cross-sectional SEM of 6.5 mg tCp_2-Ti-Me_2 seeded CNT conductor electroplated at 10 mA current and finished.

7.4.2 Titanium Tetraisopropoxide (TTIP)

Cyclopentadienyl (Cycloheptatrienyl) Titanium (II) [CHT-Ti-Cp] and Titanium Tetraisopropoxide (TTIP) precursors were selected to evaluate the deposition of Ti compounds onto the CNT roving via CFH-CVD. The CVD process was conducted under static 0.300 Torr vacuum, with three roving in parallel biased at 350 mA/roving for 1 hour. The mantle temperature was held at 200 °C for the CHT-Ti-Cp powder precursor, however, the mantle was kept at 23 °C for the liquid TTIP precursor, as the vacuum alone provides necessary conditions to evaporate the TTIP precursor. Deposition of 25 mg of the TTIP and CHT-Ti-Cp precursor onto the CNT roving can be seen in Figure 48, whereby the TTIP led to an 87.98% weight loading by mass, and the CHT-Ti-Cp led to a 67.15% weight loading. TTIP deposition is shown to form nano-needles, whereas the CHT-Ti-Cp precursor deposits more bulbous structures. The R/L remained relatively unchanged in the case of the CHT-Ti-Cp seeded conductor (354 ± 30 Ω/m), while the TTIP precursor, which is known to form titanium oxides, deposited an insulating layer on the surface of the roving.

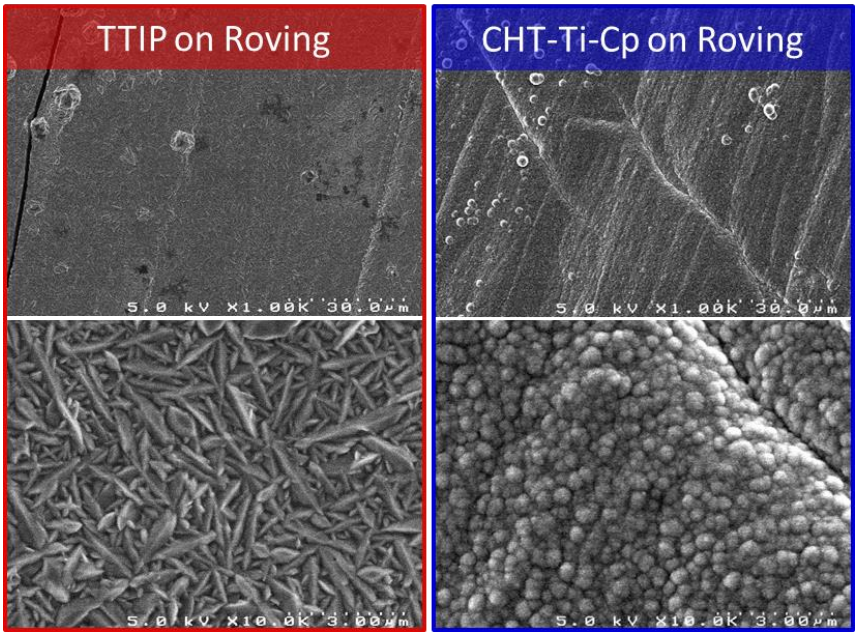

Figure 48 Surface morphology of the TTIP and CHT-Ti-Cp depositions on CNT roving as taken by SEM.

To understand the phase of the titanium deposited onto the CNTs by the TTIP precursor, Raman spectroscopy was performed. As see in Figure 49a, the TTIP seeded conductor exhibits well-defined anatase TiO_2 peaks, as compared to literature values.

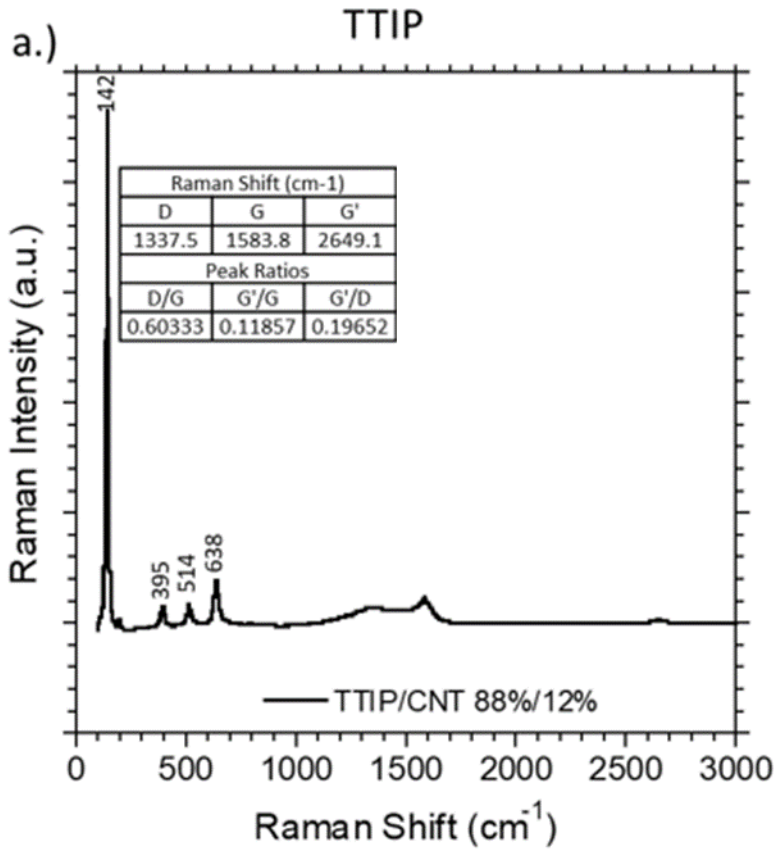

Figure 49 Raman analysis of the (a.) TTIP and (b.) CHT-Ti-Cp depositions on CNT roving.

8 Works Cited

1. Reich S, Thomsen C, Ordejón P (2002) Electronic band structure of isolated and bundled carbon nanotubes. Phys Rev B - Condens Matter Mater Phys 65:1554111–15541111. https://doi.org/10.1103/PhysRevB.65.155411

2. Landi BJ, Raffaelle RP (2007) Effects of carrier gas dynamics on single wall carbon nanotube chiral distributions during laser vaporization synthesis. J Nanosci Nanotechnol 7:883–890. https://doi.org/10.1166/jnn.2007.207

3. Jorio A, Saito R, Hertel T, et al (2018) C arbon Nanotube Photophysics

4. Cheng HM, Li F, Sun X, et al (1998) Bulk morphology and diameter distribution of single-walled carbon nanotubes synthesized by catalytic decomposition of hydrocarbons. Chem Phys Lett 289:602–610. https://doi.org/10.1016/S0009-2614(98)00479-5

5. Wu AS, Chou TW, Gillespie JW, et al (2012) Electromechanical response and failure behaviour of aerogel-spun carbon nanotube fibres under tensile loading. J Mater Chem 22:6792–6798. https://doi.org/10.1039/c2jm15869h

6. Jarosz P, Schauerman C, Alvarenga J, et al (2011) Carbon nanotube wires and cables: Near-term applications and future perspectives. Nanoscale 3:4542–4553. https://doi.org/10.1039/c1nr10814j

7. Cress CD, Ganter MJ, Schauerman CM, et al (2017) Carbon nanotube wires with continuous current rating exceeding 20 Amperes. J Appl Phys 122:. https://doi.org/10.1063/1.4990981

8. Thomsen C, Maultzsch J (2004) Carbon Nanotubes: Basic Concepts and Physical Properties. Wiley

9. Tans SJ, Devoret MH, Dai H, et al (1997) Individual single-wall carbon nanotubes as quantum wires. Nature 386:474–477

10. White CT, Todorov TN (1998) Carbon nanotubes as long ballistic conductors. Nature 393:240–241. https://doi.org/10.1038/30420

11. Zhang Z, Peng J, Zhang H (2001) Low-temperature resistance of individual single-walled carbon nanotubes: A theoretical estimation. Appl Phys Lett 79:3515–3517. https://doi.org/10.1063/1.1420493

12. Ouyang M, Huang JL, Cheung CL, Lieber CM (2001) Energy gaps in "Metallic" single-walled carbon nanotubes. Science (80-) 292:702–705. https://doi.org/10.1126/science.1058853

13. Sun CH, Lu GQ, Cheng HM (2006) Simple approach to estimating the van der Waals interaction between carbon nanotubes. Phys Rev B - Condens Matter Mater Phys 73:1–5. https://doi.org/10.1103/PhysRevB.73.195414

14. Sun CH, Yin LC, Li F, et al (2005) Van der Waals interactions between two parallel infinitely long single-walled nanotubes. Chem Phys Lett 403:343–346. https://doi.org/10.1016/j.cplett.2005.01.030

15. Delaney P, Choi HJ, Ihm J, et al (1999) Broken symmetry and pseudogaps in ropes of carbon nanotubes. Phys Rev B - Condens Matter Mater Phys 60:7899–7904. https://doi.org/10.1103/PhysRevB.60.7899

16. Kaiser AB, Skákalová V, Roth S (2008) Modelling conduction in carbon nanotube networks with different thickness, chemical treatment and irradiation. Phys E Low-Dimensional Syst Nanostructures 40:2311–2318. https://doi.org/10.1016/j.physe.2007.10.038

17. Li S, Yu Z, Rutherglen C, Burke PJ (2004) Electrical properties of 0.4 cm long single-walled carbon nanotubes. Nano Lett 4:2003–2007. https://doi.org/10.1021/nl048687z

18. Mann D, Javey A, Kong J, et al Ballistic Transport in Metallic Nanotubes with Reliable Pd Ohmic Contacts_Mann Javey and Dai et al_NANO LETTERS_2003.pdf. 1–15

19. Purewal MS, Hong BH, Ravi A, et al (2007) Scaling of resistance and electron mean free path of single-walled carbon nanotubes. Phys Rev Lett 98:2–5. https://doi.org/10.1103/PhysRevLett.98.186808

20. Bachtold A, Fuhrer MS, Plyasunov S, et al (2000) Scanned probe microscopy of electronic transport in carbon nanotubes. Phys Rev Lett 84:6082–6085. https://doi.org/10.1103/PhysRevLett.84.6082

21. Dürkop T, Getty SA, Cobas E, Fuhrer MS (2004) Extraordinary Mobility in Semiconducting Carbon Nanotubes. Nano Lett 4:35–39. https://doi.org/10.1021/nl034841q

22. Stadermann M, Papadakis SJ, Falvo MR, et al (2004) Nanoscale study of conduction through carbon nanotube networks. Phys Rev B - Condens Matter Mater Phys 69:8–11. https://doi.org/10.1103/PhysRevB.69.201402

23. Kalinin S V., Jesse S, Shin J, et al (2004) Scanning probe microscopy imaging of frequency dependent electrical transport through carbon nanotube networks in polymers. Nanotechnology 15:907–912. https://doi.org/10.1088/0957-4484/15/8/006

24. Kodama Y, Sato R, Inami N, et al (2007) Field-effect modulation of contact resistance between carbon nanotubes. Appl Phys Lett 91:. https://doi.org/10.1063/1.2790805

25. Nirmalraj PN, Lyons PE, De S, et al (2009) Electrical connectivity in single-walled carbon nanotube networks. Nano Lett 9:3890–3895. https://doi.org/10.1021/nl9020914

26. Skákalová V, Kaiser AB, Woo YS, Roth S (2006) Electronic transport in carbon nanotubes: From individual nanotubes to thin and thick networks. Conf Proc - 6th Int Conf Adv Semicond Devices Microsystems, ASDAM'06 11–13. https://doi.org/10.1109/ASDAM.2006.331142

27. Leggiero AP, Trettner KJ, Ursino HL, et al (2019) High Conductivity Copper − Carbon Nanotube Hybrids via Site- Speci fi c Chemical Vapor Deposition. ACS Appl Nano Mater 2:118–126. https://doi.org/10.1021/acsanm.8b01740

28. Downes RD, Hao A, Park JG, et al (2015) Geometrically constrained self-assembly and crystal packing of flattened and aligned carbon nanotubes. Carbon N Y 93:953–966. https://doi.org/10.1016/j.carbon.2015.06.012

29. Alvarenga J, Jarosz PR, Schauerman CM, et al (2010) High conductivity carbon nanotube wires from radial densification and ionic doping. Appl Phys Lett 97:.

https://doi.org/10.1063/1.3506703

30. Zhao Y, Wei J, Vajtai R, et al (2011) Iodine doped carbon nanotube cables exceeding specific electrical conductivity of metals. Sci Rep 1:1–5. https://doi.org/10.1038/srep00083

31. Janas D, Milowska KZ, Bristowe PD, Koziol KKK (2017) Improving the electrical properties of carbon nanotubes with interhalogen compounds. Nanoscale 9:3212–3221. https://doi.org/10.1039/c7nr00224f

32. Puchades I, Lawlor CC, Schauerman CM, et al (2014) Mechanism of chemical doping in electronic-type-separated single wall carbon nanotubes towards high electrical conductivity. J Mater Chem C 2:4904–4908. https://doi.org/10.1039/c4tc00699b

33. Li S, Zhang X, Zhao J, et al (2012) Enhancement of carbon nanotube fibres using different solvents and polymers. Compos Sci Technol 72:1402–1407. https://doi.org/10.1016/j.compscitech.2012.05.013

34. Liu P, Hu DCM, Tran TQ, et al (2016) Electrical property enhancement of carbon nanotube fibers from post treatments. Colloids Surfaces A Physicochem Eng Asp 509:384–389. https://doi.org/10.1016/j.colsurfa.2016.09.036

35. Di J, Fang S, Moura FA, et al (2016) Strong, Twist-Stable Carbon Nanotube Yarns and Muscles by Tension Annealing at Extreme Temperatures. Adv. Mater. 6598–6605

36. Subramaniam C, Sekiguchi A, Yamada T, et al (2016) Nano-scale, planar and

multi-tiered current pathways from a carbon nanotube–copper composite with high conductivity, ampacity and stability. Nanoscale 8:3888–3894. https://doi.org/10.1039/C5NR03762J

37. Subramaniam C, Yamada T, Kobashi K, et al (2013) One hundred fold increase in current carrying capacity in a carbon nanotube-copper composite. Nat Commun 4:1–7. https://doi.org/10.1038/ncomms3202

38. Tokutomi J, Uemura T, Sugiyama S, et al (2015) Hot extrusion to manufacture the metal matrix composite of carbon nanotube and aluminum with excellent electrical conductivities and mechanical properties. CIRP Ann - Manuf Technol 64:257–260. https://doi.org/10.1016/j.cirp.2015.04.083

39. Hjortstam O, Isberg P, Söderholm S, Dai H (2004) Can we achieve ultra-low resistivity in carbon nanotube-based metal composites? Appl Phys A Mater Sci Process 78:1175–1179. https://doi.org/10.1007/s00339-003-2424-x

40. Ta BQ, Ngo A V., Nilsen O, et al (2013) Deposition of Palladium on Suspended and Locally Grown Carbon N anotubes using Thermal Evaporation. 2013 13th IEEE Conf Nanotechnol 1176–1179

41. Gingery D, Bühlmann P (2008) Formation of gold nanoparticles on multiwalled carbon nanotubes by thermal evaporation. Carbon N Y 46:1966–1972. https://doi.org/10.1016/j.carbon.2008.08.007

42. Cox ND, Rape A, Pham M, et al (2016) Free-standing silver/carbon nanotube metal matrix composite thin films. J Mater Sci 51:10935–10942. https://doi.org/10.1007/s10853-016-0305-x

43. Scarselli M, Camilli L, Castrucci P, et al (2012) In situ formation of noble metal nanoparticles on multiwalled carbon nanotubes and its implication in metal-nanotube interactions. Carbon N Y 50:875–884. https://doi.org/10.1016/j.carbon.2011.09.048

44. Han B, Guo E, Xue X, et al (2017) Fabrication and densification of high performance carbon nanotube/copper composite fibers. Carbon N Y 123:593–604. https://doi.org/10.1016/j.carbon.2017.08.004

45. Milowska KZ, Ghorbani-Asl M, Burda M, et al (2017) Breaking the electrical barrier between copper and carbon nanotubes. Nanoscale 9:8458–8469. https://doi.org/10.1039/C7NR02142A

46. Janas D, Koziol KKK (2016) The influence of metal nanoparticles on electrical properties of carbon nanotubes. Appl Surf Sci 376:74–78. https://doi.org/10.1016/j.apsusc.2016.02.233

47. Muratore C, Reed AN, Bultman JE, et al (2013) Nanoparticle decoration of carbon nanotubes by sputtering. Carbon N Y 57:274–281. https://doi.org/10.1016/j.carbon.2013.01.074

48. Han B, Guo E, Xue X, et al (2018) Fabricating and strengthening the carbon nanotube/copper composite fibers with high strength and high electrical conductivity. Appl Surf Sci 441:984–992. https://doi.org/10.1016/j.apsusc.2018.02.078

49. Janas D, Koziol KKK (2016) The influence of metal nanoparticles on electrical properties of carbon nanotubes. Appl Surf Sci 376:74–78.

https://doi.org/10.1016/j.apsusc.2016.02.233

50. Tran TQ, Lee JKY, Chinnappan A, et al (2020) Strong, lightweight, and highly conductive CNT/Au/Cu wires from sputtering and electroplating methods. J Mater Sci Technol 40:99–106. https://doi.org/10.1016/j.jmst.2019.08.033

51. Rochefort A, Salahub DR, Avouris P (1998) The effect of structural distortions on the electronic structure of carbon nanotubes. Chem Phys Lett 297:45–50. https://doi.org/10.1016/S0009-2614(98)01105-1

52. Charatan RM, Gross ME, Eaglesham DJ (1994) Plasma enhanced chemical vapor deposition of titanium nitride thin films using cyclopentadienyl cycloheptatrienyl titanium. J Appl Phys 76:4377–4382. https://doi.org/10.1063/1.357327

53. Gregorczyk KE, Kozen AC, Chen X, et al (2015) Fabrication of 3D core-shell multiwalled carbon nanotube@RuO2 lithium-ion battery electrodes through a RuO2 atomic layer deposition process. ACS Nano 9:464–473. https://doi.org/10.1021/nn505644q

54. Jin SH, Jun GH, Hong SH, Jeon S (2012) Conformal coating of titanium suboxide on carbon nanotube networks by atomic layer deposition for inverted organic photovoltaic cells. Carbon N Y 50:4483–4488. https://doi.org/10.1016/j.carbon.2012.05.027

55. Do JW, Estrada D, Xie X, et al (2013) Nanosoldering carbon nanotube junctions by local chemical vapor deposition for improved device performance. Nano Lett 13:5844–5850. https://doi.org/10.1021/nl4026083

56. Hannula PM, Peltonen A, Aromaa J, et al (2016) Carbon nanotube-copper composites by electrodeposition on carbon nanotube fibers. Carbon N Y 107:281–287. https://doi.org/10.1016/j.carbon.2016.06.008

57. Hannula PM, Aromaa J, Wilson BP, et al (2017) Observations of copper deposition on functionalized carbon nanotube films. Electrochim Acta 232:495–504. https://doi.org/10.1016/j.electacta.2017.03.006

58. Subramaniam C, Sekiguchi A, Yamada T, et al (2016) Nano-scale, planar and multi-tiered current pathways from a carbon nanotube–copper composite with high conductivity, ampacity and stability. Nanoscale 8:3888–3894. https://doi.org/10.1039/C5NR03762J

59. Hussain S, Pal AK (2008) Incorporation of nanocrystalline silver on carbon nanotubes by electrodeposition technique. Mater Lett 62:1874–1877. https://doi.org/10.1016/j.matlet.2007.10.021

60. Sundaram R, Yamada T, Hata K, Sekiguchi A (2017) Electrical performance of lightweight CNT-Cu composite wires impacted by surface and internal Cu spatial distribution. Sci Rep 1–11. https://doi.org/10.1038/s41598-017-09279-x

61. Von Glasow A, Fischer AH, Steinlesberger G (2003) Using the temperature coefficient of the resistance (TCR) as early reliability indicator for stressvoiding risks in Cu interconnects. IEEE Int Reliab Phys Symp Proc 2003–Janua:126–131. https://doi.org/10.1109/RELPHY.2003.1197732

62. Zou J, Liu D, Zhao J, et al (2018) Ni Nanobuffer Layer Provides Light-Weight CNT/Cu Fibers with Superior Robustness, Conductivity, and Ampacity. ACS Appl

Mater Interfaces 10:8197–8204. https://doi.org/10.1021/acsami.7b19012

63. Zhang Y, Franklin NW, Chen RJ, Dai H (2000) Metal coating on suspended carbon nanotubes and its implication to metal-tube interaction. Chem Phys Lett 331:35–41. https://doi.org/10.1016/S0009-2614(00)01162-3

64. Zhang Y, Dai H (2000) Formation of metal nanowires on suspended single-walled carbon nanotubes. Appl Phys Lett 77:3015–3017. https://doi.org/10.1063/1.1324731

65. Chopra KL (1969) Thin Film Phenomena. McGraw-Hill, New York

66. Sung CM, Tai MF (1997) Reactivities of Transition Metals with Carbon: Implications to the Mechanism of Diamond Synthesis Under High Pressure. Int J Refract Met Hard Mater 15:237–256. https://doi.org/10.1016/S0263-4368(97)00003-6

67. Lim SC, Jang JH, Bae DJ, et al (2009) Contact resistance between metal and carbon nanotube interconnects: Effect of work function and wettability. Appl Phys Lett 95:93–96. https://doi.org/10.1063/1.3255016

68. Yamada T, Saito T, Suzuki M, et al (2010) Tunneling between carbon nanofiber and gold electrodes. J Appl Phys 107:. https://doi.org/10.1063/1.3295901

69. Wilhite P, Vyas AA, Tan J, et al (2014) Metal-nanocarbon contacts. Semicond Sci Technol 29:. https://doi.org/10.1088/0268-1242/29/5/054006

70. Blackburn JL, Barnes TM, Beard MC, et al (2008) Transparent conductive single-walled carbon nanotube networks with precisely tunable ratios of semiconducting

and metallic nanotubes. ACS Nano 2:1266–1274. https://doi.org/10.1021/nn800200d

71. Zhao J, Buldum A, Han J, Lu JP (2002) Gas molecule adsorption in carbon nanotubes and nanotube bundles. Nanotechnology 13:195–200. https://doi.org/10.1088/0957-4484/13/2/312

72. Leenaerts O, Partoens B, Peeters FM (2008) Adsorption of H2 O, N H3, CO, N O2, and NO on graphene: A first-principles study. Phys Rev B - Condens Matter Mater Phys 77:1–6. https://doi.org/10.1103/PhysRevB.77.125416

73. Zahab A, Spina L, Poncharal P, Marlière C (2000) Water-vapor effect on the electrical conductivity of a single-walled carbon nanotube mat. Phys Rev B - Condens Matter Mater Phys 62:10000–10003. https://doi.org/10.1103/PhysRevB.62.10000

74. Sumanasekera GU, Adu CKW, Fang S, Eklund PC (2000) Effects of gas adsorption and collisions on electrical transport in single-walled carbon nanotubes. Phys Rev Lett 85:1096–1099. https://doi.org/10.1103/PhysRevLett.85.1096

75. Ifuku R, Nagashio K, Nishimura T, Toriumi A (2013) The density of states of graphene underneath a metal electrode and its correlation with the contact resistivity. Appl Phys Lett 103:. https://doi.org/10.1063/1.4815990

76. Liebau M, Unger E, Duesberg GS, et al (2003) Contact improvement of carbon nanotubes via electroless nickel deposition. Appl Phys A Mater Sci Process 77:731–734. https://doi.org/10.1007/s00339-003-2207-4

77. Lee S, Kahng SJ, Kuk Y (2010) Nano-level wettings of platinum and palladium on single-walled carbon nanotubes. Chem Phys Lett 500:82–85. https://doi.org/10.1016/j.cplett.2010.09.082

78. Dai H (2000) Controlling nanotube growth. Phys World 13:43–47. https://doi.org/10.1088/2058-7058/13/6/28

79. Lim SC, Jang JH, Bae DJ, et al (2010) Contact resistance between metal and carbon nanotube interconnects: Effect of work function and wettability. Appl Phys Lett 95:264103. https://doi.org/10.1063/1.3255016

80. Lian R, Yu H, He L, et al (2016) Sublimation of Ag nanocrystals and their wetting behaviors with graphene and carbon nanotubes. Carbon N Y 101:368–376. https://doi.org/10.1016/j.carbon.2016.01.105

81. Sung C, Taib M (1997) Reactivities of Transition Metals with Carbon : Implications to the Mechanism of Diamond Synthesis Under High Pressure. 15:237–256

82. Chu K, Jia C chang, Jiang L kun, Li W sheng (2013) Improvement of interface and mechanical properties in carbon nanotube reinforced Cu-Cr matrix composites. Mater Des 45:407–411. https://doi.org/10.1016/j.matdes.2012.09.027

83. Leggiero AP, Driess SD, Loughran ED, et al (2020) Platinum nanometal interconnection of copper–carbon nanotube hybrid electrical conductors. Carbon N Y 168:290–301. https://doi.org/10.1016/j.carbon.2020.07.009

84. Standing R, Nicholas M (1978) The wetting of alumina and vitreous carbon by

copper-tin-titanium alloys. J Mater Sci 13:1509–1514. https://doi.org/10.1007/BF00553207

85. Nie JH, Jia CC, Jia X, et al (2012) Fabrication and thermal conductivity of copper matrix composites reinforced by tungsten-coated carbon nanotubes. Int J Miner Metall Mater 19:446–452. https://doi.org/10.1007/s12613-012-0577-3

86. Dileo RA, Castiglia A, Ganter MJ, et al (2010) Enhanced Capacity and Rate Capability of Carbon Nanotube Based Anodes with Batteries. ACS Nano 4:6121–6131

87. Menon M, Andriotis AN, Froudakis GE (2000) Curvature dependence of the metal catalyst atom interaction with carbon nanotubes walls. Chem Phys Lett 320:425–434. https://doi.org/10.1016/S0009-2614(00)00224-4

88. Bakonyi I, Tóth-Kadar E, Tóth J, et al (1999) Magnetic and electrical transport properties of electrodeposited Ni-Cu alloys and Ni 81 Cu 19 /Cu multilayers. J Phys Condens Matter 11:963–973. https://doi.org/10.1088/0953-8984/11/4/004

89. Hur S-G, Kim D-J, Kang B-D, Yoon S-G (2004) Effect of the deposition temperature on temperature coefficient of resistance in CuNi thin film resistors. J Vac Sci Technol B Microelectron Nanom Struct 22:2698. https://doi.org/10.1116/1.1815313

90. Yang CK, Zhao J, Lu JP (2002) Binding energies and electronic structures of adsorbed titanium chains on carbon nanotubes. Phys Rev B - Condens Matter Mater Phys 66:414031–414034. https://doi.org/10.1103/PhysRevB.66.041403

91. Matsuda Y, Deng WQ, Goddard WA (2007) Contact resistance properties between nanotubes and various metals from quantum mechanics. J Phys Chem C 111:11113–11116. https://doi.org/10.1021/jp072794a

92. Uh HS, Park S, Kim B (2010) Enhanced field emission properties from titanium-coated carbon nanotubes. Diam Relat Mater 19:586–589. https://doi.org/10.1016/j.diamond.2009.11.021

93. Srividya S, Gautam S, Jha P, et al (2010) Titanium buffer layer for improved field emission of CNT based cold cathode. Appl Surf Sci 256:3563–3566. https://doi.org/10.1016/j.apsusc.2009.12.155

94. Bonard JM, Klinke C, Dean KA, Coll BF (2003) Degradation and failure of carbon nanotube field emitters. Phys Rev B - Condens Matter Mater Phys 67:10. https://doi.org/10.1103/PhysRevB.67.115406

95. Chu K, Jia CC, Li WS, Wang P (2013) Mechanical and electrical properties of carbon-nanotube-reinforced Cu-Ti alloy matrix composites. Phys Status Solidi Appl Mater Sci 210:594–599. https://doi.org/10.1002/pssa.201228549

96. Lisowska A, Biallozor S (1982) Investigations on electroreduction of TiCl4 in dimethylsulfoxide. Electrochim Acta 27:105–110. https://doi.org/10.1016/0013-4686(82)80067-4

97. Biallozor S, Lisowska A (1980) Study on electroreduction of titanium tetrachloride in acetonitrile solutions. Electrochim Acta 25:1209–1214. https://doi.org/10.1016/0013-4686(80)87121-0

98. Endres F, Zein El Abedin S, Saad AY, et al (2008) On the electrodeposition of titanium in ionic liquids. Phys Chem Chem Phys 10:2189–2199. https://doi.org/10.1039/b800353j

99. McIntyre DJ, Hirschman RK, Puchades I, Landi BJ (2020) Enhanced copper–carbon nanotube hybrid conductors with titanium adhesion layer. J Mater Sci 55:6610–6622. https://doi.org/10.1007/s10853-020-04457-1

100. (2019) Nanocomp Technologies, INC. A Hunstman Company. http://www.miralon.com/

101. Simoes S, Calinas R, Vieira MT, et al (2010) In situ TEM study of grain growth in nanocrystalline copper thin films. Nanotechnology 21:. https://doi.org/10.1088/0957-4484/21/14/145701

102. Shibuta Y, Suzuki T (2010) Melting and solidification point of fcc-metal nanoparticles with respect to particle size: A molecular dynamics study. Chem Phys Lett 498:323–327. https://doi.org/10.1016/j.cplett.2010.08.082

103. Carey JD, Ong LL, Silva SRP (2003) Formation of low-temperature self-organized nanoscale nickel metal islands. Nanotechnology 14:1223–1227. https://doi.org/10.1088/0957-4484/14/11/011

104. Kaiser AB (2001) Electronic transport properties of conducting polymers and carbon nanotubes. Rep Prog Phys 64:1–49

105. Barnes TM, Blackburn JL, Lagemaat J Van De, et al (2008) Reversibility, Dopant Desorption, and Tunneling in the Temperature- Dependent Conductivity of Type-

Separated, Conductive Carbon Nanotube Networks. ACS Nano 2:1968–1976. https://doi.org/https://doi.org/10.1021/nn800194u

106. Colasanti S, Robbiano V, Loghin FC, et al (2016) Experimental and Computational Study on the Temperature Behavior of CNT Networks. IEEE Trans Nanotechnol 15:171–178. https://doi.org/10.1109/TNANO.2015.2510965

107. Roch A, Greifzu M, Talens ER, et al (2015) Ambient effects on the electrical conductivity of carbon nanotubes. Carbon N Y 95:347–353. https://doi.org/10.1016/j.carbon.2015.08.045

108. Kasap SO (2006) Principles of Electronic Materials and Devices, 3rd ed. McGraw-Hill

109. Durgun E, Dag S, Bagci VMK, et al (2003) Systematic study of adsorption of single atoms on a carbon nanotube. Phys Rev B - Condens Matter Mater Phys 67:1–4. https://doi.org/10.1103/PhysRevB.67.201401

110. Zhao J, Qiu Q, Wang B, et al (2001) Geometric and electronic properties of titanium clusters studied by ultrasoft pseudopotential. Solid State Commun 118:157–161. https://doi.org/10.1016/S0038-1098(01)00044-8

111. Yi C, Bagchi S, Dmuchowski CM, et al (2018) Direct nanomechanical characterization of carbon nanotube - titanium interfaces. Carbon N Y 132:548–555. https://doi.org/10.1016/j.carbon.2018.02.069

112. AHMAD HM, GREIG D (1974) the Electrical Resistivity and Thermopower of Nickel-Copper Alloys. Le J Phys Colloq 35:C4-223-C4-226.

https://doi.org/10.1051/jphyscol:1974440

113. Liang LH, Liu D, Jiang Q (2003) Size-dependent continuous binary solution phase diagram. Nanotechnology 14:438–442. https://doi.org/10.1088/0957-4484/14/4/306

114. McIntyre DJ, Leggiero AP, Hailstone RK, et al (2020) Integrated Titanium-Carbon Nanotube Conductors via Joule-Heating Driven Chemical Vapor Deposition. ECS Trans 97:321–327. https://doi.org/10.1149/09707.0321ecst

115. Kanbara T, Takenobu T, Takahashi T, et al (2010) Contact resistance modulation in carbon nanotube devices investigated by four-probe experiments Contact resistance modulation in carbon nanotube devices investigated by four-probe experiments. 053118:86–89. https://doi.org/10.1063/1.2171481

116. Maeda S, Wilhite P, Kanzaki N, et al (2011) Change in carbon nanofiber resistance from ambient to vacuum. AIP Adv 022102:. https://doi.org/10.1063/1.3582812

117. Landi BJ, Ruf HJ, Evans CM, et al (2005) Purity Assessment of Single-Wall Carbon Nanotubes , Using Optical Absorption Spectroscopy. 9952–9965

118. Leggiero AP (2020) High Conductivity Metal–Carbon Nanotube Hybrid Conductors Via Chemical Vapor Deposition and Electroplating. Rochester Institute of Technology, Microsystems Engineering, Dissertation

119. Djaoued Y, Balaji S, Brüning R (2012) Electrochromic devices based on porous tungsten oxide thin films. J Nanomater 2012:. https://doi.org/10.1155/2012/674168

120. Wilken T, Morcom W, Wert C, Woodhouse J (1976) Reduction of Tungsten Oxide

to Tungsten Metal. Metall Trans B 7:589–597

121. Porrati F, Sachser R, Strauss M, et al (2010) Artificial granularity in two-dimensional arrays of nanodots fabricated by focused-electron-beam-induced deposition. Nanotechnology 21:. https://doi.org/10.1088/0957-4484/21/37/375302

122. Woolley JC (1957) Introduction to solid state physics